Multi-Dimensional Unsteady Characteristics

Multi-Dimensional Unsteady Characteristics of the Standing Oblique Detonation

Akiko Matsuo

①

Multi-Dimensional Unsteady Characteristics of the Standing Oblique Detonation

Akiko Matsuo

MULTI-DIMENSIONAL UNSTEADY CHARACTERISTICS OF THE STANDING OBLIQUE DETONATION

ABSTRACT

The characteristics of the standing oblique detonation (SOD) around a two-dimensional blunted wedge and an axisymmetric blunt body are studied by the numerical simulations to clarify the underlying physics, based on the relations among thermodynamic, chemical kinetics and fluid mechanical considerations.

In the study of SOD supported by the two-dimensional wedge, the existence of the critical values for the establishment of SOD in a hypersonic premixed gas is confirmed by changing the wedge tip radius and the wedge angles. Whether a coupled oblique detonation is obtained or not significantly depends on the scale of the wedge tip radius and the angle of the wedge. The numerical results suggest that there exist three different modes in SOD; (i) steady oblique coupled detonations, (ii) steady oblique decoupled detonations, (iii) run-away detonations which are unable to stand in front of a wedge. The mode change can be explained by the limiting angle of the oblique shock wave.

In the study of SOD supported by the axisymmetric blunt body, the ballistic range experiments for the combustible gas at hypervelocities are numerically simulated. The simulations are mainly focused on the periodic unsteadiness observed on the reaction boundary in the shock layer of a spherical projectile body. A series of our simulations have clarified the detailed mechanism for the periodic unsteadiness. First, the basic characteristics of the periodic unsteadiness in the shock-induced combustion have been qualitatively studied, using a simplified chemical reaction model. The dependency of the mechanism on the projectile velocity is also investigated. Next, an enhanced chemical model to explain the mechanism for the periodic unsteadiness is proposed, which proved to be appropriate to explain the unsteadiness in various projectile velocities. Next, key parameters for the periodic unsteadiness have been quantitatively studied by the parametric study, using a H_2/Air gas mixture: They are the induction time, the heat release and the rate of heat release. The induction time is a key parameter to determine the frequency of unsteadiness. The rate of heat release is important for the unsteadiness itself. The amount of heat release is important because the total energy creating the compression waves depends on it. The simulations reveal the underlaying physics of the flowfields.

ACKNOWLEDGMENTS

I would like to thank my family and many people who enabled to complete this dissertation. I would like to thank my advisor, Professor Toshi Fujiwara, for his technical support throughout my studies, and people in the propulsion laboratory in Nagoya University. Thanks also to Prof. Kozo Fujii and the members in Fujii laboratory in the ISAS for supporting me and helping my research.

I express appreciation to the Japan Society for the Promotion of Science which has given me a fellowship for Japanese Junior Scientists to further my research.

TABLE OF CONTENTS

LIST OF TABLES

LIST OF FIGURES

Figure

LIST OF PUBLICATIONS

JOURNAL ARTICLE

1. *"Numerical Investigation of Oscillatory Instability Mechanism in Shock-Induced Combustion around an Axisymmetric Blunt Body"*
   Akiko Matsuo and Toshi Fujiwara
   To appear in AIAA Journal, July, 1993

2. *"Numerical Prediction of Mechanism of Oscillatory Instabilities in Shock-Induced Combustion"*
   Akiko Matsuo and Toshi Fujiwara
   To appear in Progress in Astronautics and Aeronautics, 1993

3. *"Numerical Investigation of Standing Oblique Detonation Supported by Two-Dimensional Blunted Wedge"*
   Akiko Matsuo and Toshi Fujiwara
   Transactions of the Japan Society for Aeronautical and Space Sciences, May, Vol. 36, No. 111, 1993, pp. 47-56

PROCEEDINGS OF INTERNATIONAL CONFERENCES

1. *"A Two-Dimensional Detonation Supported by a Blunt Body or a Wedge"*
   Toshi Fujiwara, Akiko Matsuo and H. Nomoto
   AIAA 26th Aerospace Sciences Meeting, Reno, Nevada, USA, Jan. 1988
   AIAA Paper 88-0098

2. *"Standing Oblique Detonation Held by a Wedge"*
   Akiko Matsuo
   16th International Symposium on Space Technology and Science, Sapporo, Japan, May 1988
   Proceedings of 16th International Symposium on Space Technology and Science, pp. 2589-2594

3. *"Oxyhydrogen Oblique Detonation Supported by Two-Dimensional Wedge"*
   Toshi Fujiwara and Akiko Matsuo
   International Symposium on Computational Fluid Dynamics, Nagoya, Japan, Aug. 1989
   Proceedings of the International Symposium on Computational Fluid Dynamics, pp. 623-628
   Numerical Methods in Fluid Dynamics II, pp. 580-586.

4. *"Detailed Numerical Analysis of Standing Oblique Detonation"*
   Akiko Matsuo and Toshi Fujiwara
   17th International Symposium on Space Technology and Science, Tokyo, Japan, May 1990

Proceedings of 17th International Symposium on Space Technology and Science, pp. 735-740

5. *"Numerical Simulation of Shock-Induced Combustion around an Axisymmetric Blunt Body"*
   Akiko Matsuo and Toshi Fujiwara
   AIAA 26th Thermophysics Conference, Waikiki, Hawaii, USA, June 1991
   AIAA Paper 91-1414

6. *"On the Mechanism of Shock-Induced Combustion around an Axisymmetric Blunt Body"*
   Akiko Matsuo, Toshi Fujiwara and Kozo Fujii
   18th International Symposium on Space Technology and Science, Kagoshima, Japan, May 1992
   Proceedings of 18th International Symposium on Space Technology and Science, pp. 691-696

7. *"Flow Features of Shock-Induced Combustion around Projectile Travelling at Hypervelocities"*
   Akiko Matsuo, Toshi Fujiwara and Kozo Fujii
   AIAA 31st Aerospace Sciences Meeting, Reno, Nevada, USA, Jan. 1993
   AIAA Paper 93-0451

CHAPTERS - PUBLICATIONS CORRESPONDENCE

CHAPTER III STANDING OBLIQUE DETONATION SUPPORTED BY TWO-DIMENSIONAL BLUNTED WEDGE

1. *"Numerical Investigation of Standing Oblique Detonation Supported by Two-Dimensional Blunted Wedge"*
   Akiko Matsuo and Toshi Fujiwara
   Transactions of the Japan Society for Aeronautical and Space Sciences, May, 1993

2. *"A Two-Dimensional Detonation Supported by a Blunt Body or a Wedge"*
   Toshi Fujiwara, Akiko Matsuo and H. Nomoto
   AIAA 26th Aerospace Sciences Meeting, Reno, Nevada, USA, Jan. 1988, AIAA Paper 88-0098

3. *"Standing Oblique Detonation Held by a Wedge"*
   Akiko Matsuo
   16th International Symposium on Space Technology and Science, Sapporo, Japan, May 1988
   Proceedings of 16th International Symposium on Space Technology and Science, pp. 2589-2594

4. *"Oxyhydrogen Oblique Detonation Supported by Two-Dimensional Wedge"*
   Toshi Fujiwara and Akiko Matsuo
   International Symposium on Computational Fluid Dynamics, Nagoya, Japan, Aug. 1989
   Proceedings of the International Symposium on Computational Fluid Dynamics, pp. 623-628
   Numerical Methods in Fluid Dynamics II, pp. 580-586.

5. *"Detailed Numerical Analysis of Standing Oblique Detonation"*
   Akiko Matsuo and Toshi Fujiwara
   17th International Symposium on Space Technology and Science, Tokyo, Japan, May 1990
   Proceedings of 17th International Symposium on Space Technology and Science, pp. 735-740

CHAPTER V NUMERICAL STUDIES BASED ON THE SIMPLIFIED TWO-STEP CHEMICAL REACTION MECHANISM

1. *"Numerical Simulation of Shock-Induced Combustion around an Axisymmetric Blunt Body"*
   Akiko Matsuo and Toshi Fujiwara
   AIAA 26th Thermophysics Conference, Waikiki, Hawaii, USA, June 1991
   AIAA Paper 91-1414.

2. *"Numerical Investigation of Oscillatory Instability Mechanism in Shock-Induced Combustion around an Axisymmetric Blunt Body"*
   Akiko Matsuo and Toshi Fujiwara
   To appear in AIAA Journal, July, 1993.

3. *"Numerical Prediction of Mechanism of Oscillatory Instabilities in Shock-Induced Combustion"*
   Akiko Matsuo and Toshi Fujiwara
   To appear in Progress in Astronautics and Aeronautics, 1993.

CHAPTER VI PARAMETRIC STUDIES FOR VARIOUS PROJECTILE VELOCITIES

1. *"On the Mechanism of Shock-Induced Combustion around an Axisymmetric Blunt Body"*
   Akiko Matsuo, Toshi Fujiwara and Kozo Fujii
   18th International Symposium on Space Technology and Science, Kagoshima, Japan, May 1992
   Proceedings of 18th International Symposium on Space Technology and Science, pp. 691-696

CHAPTER VII FLOW FEATURES OF SHOCK-INDUCED COMBUSTION BASED ON H_2-O_2 REACTION MECHANISM

1. *"Flow Features of Shock-Induced Combustion around Projectile Travelling at Hypervelocities"*
   Akiko Matsuo, Toshi Fujiwara and Kozo Fujii
   AIAA 31st Aerospace Sciences Meeting, Reno, Nevada, USA, Jan. 1993,
   AIAA Paper 93-0451

NOMENCLATURE

Roman Symbols

A_k	constant in the Arrhenius expression for each reaction, Table 2.1 and 2.2
c	frozen speed of sound
c_{xi}	mass fraction of species i, ρ_i / ρ
c_p	specific heat at constant pressure for the gas mixture
D	detonation wave speed
e	total energy per unit volume
E_1, E_2	activation energy for the simplified reaction mechanism
E, F	convective flux vectors in Cartesian coordinates
$\hat{E}, \hat{F}$	transformed convective flux vector in generalized coordinates
E_k	constant in the Arrhenius expression for each reaction, Table 2.1 and 2.2
f	frequency
H	enthalpy
H	axisymmetric source term vector
$\hat{H}$	transformed axisymmetric source term vector in generalized coordinates
h_i	enthalpy per unit mass of species i
I	identity matrix
J	transformation Jacobian
k_1, k_2	reaction rate constants for the simplified reaction mechanism
$k_{f,k}, k_{b,k}$	forward and backward reaction rates for each reaction k
$K_{eq,k}$	equilibrium constant for reaction k
$K_{Peq,k}$	pressure equilibrium constant for reaction k
M	any possible species for third-body collision partner
M	Mach number
n_k	constant in the Arrhenius expression for each reaction, Table 2.1 and 2.2
P	pressure

Q	exothermic energy per unit gram for the simplified reaction mechanism
R	gas constant
R_i	gas constant for species i
R_u	universal gas constant, $R_u = 8.3143$ J/(molK) = 1.987 cal/(molK)
R_k	reaction rate for reaction k
s_i^o	entropy of species i
S	chemical source term vector
$\hat{S}$	transformed chemical source term vector in generalized coordinates
T	absolute temperature
t	physical time
U	vector of conserved variables
$\hat{U}$	transformed vector of conserved variables in generalized coordinates
U	Contravarient velocity component along the ξ axis
u,v	x and y components of velocity
V	Contravarient velocity component along the η axis
v	Velocity component along the y axis
W_i	molecular weight of species i
x	Cartesian coordinate
y	Cartesian coordinate

Greek Symbols

ω_i	source term in the continuity equation of species i
α_{ik}	third efficiency factor for reaction k and species i
γ	Specific heat ratio
η	Transformed coordinate normal to the body
ξ	Transformed coordinate along the body
ρ	Fluid density
ρ_i	density of species i

v', v''	stoichiometric coefficients of the reactant and products for each chemical reaction

Subscript

∞	evaluated in the free stream
$\circ$	stagnation values
i	index for species
j	index for grid points along the body
k	index for grid points in the normal direction to the body
k	index for reaction
N	number of species

Superscript

n	evaluated at time $n\Delta t$
$n+1$	evaluated at time $(n+1)\Delta t$

CHAPTER I

INTRODUCTION

In recent years, renewed interest in hypersonic air-breathing vehicles and hypervelocity mass launchers has created needs to study characteristics of hypersonic combustion in combustible gas mixtures. This type of combustion is present in such hypersonic propulsion concepts as the supersonic combustion ramjet (SCRAMJET), the oblique detonation wave engine (ODWE), and the ram accelerator. Obtaining good understanding of this type of combustion is particularly important for such hypersonic propulsions.

One design concept for a supersonic combustion ramjet (SCRAMJET) is depicted in Fig. 1.1. In this design, air is decelerated in an inlet diffuser through a series of oblique shocks to attain the temperature and pressure favorable for combustion. The supersonic air enters the combustor where fuel is injected, mixed and burned. The hot gas exits through the nozzle where it is expanded to provide thrust for the vehicle. One of the biggest challenges related to this concept is how the fuel and air can be quickly mixed without significant energy loss. Rapid mixing is required because the residence time in the combustor is short, and high efficiency is important because losses of just a few percent result in a crucial loss of thrust.

Another design called the oblique detonation wave engine (ODWE) in Fig. 1.2 has recently been proposed as an alternative to the SCRAMJET. It is considered to improve mixing by injecting the fuel at the upstream of the combustor where temperatures are relatively low. The temperature behind the an oblique shock in the combustor is high enough to cause ignition, so that the fuel-air mixture detonates. Furthermore, an additional distance from the injection point to the combustor is provided for mixing the fuel and air. The ODWE design could reduce combustor length and lower engine weight because no mixing is required in the combustor. However, questions have been raised concerning stability (flameholding) and degree of thermodynamic irreversibility (total pressure loss) characteristics of the proposed ODWE. Attempts to stabilize and analyze oblique detonation waves, performed in the late 1950s and early 1960s, were inconclusive, as experimental limitations permitted only low approach Mach numbers and correspondingly limited (sub-stoichiometric) amounts of heat addition to the flow.

The ram accelerator is a hypervelocity mass launcher device in which a shaped projectile can in principle be accelerated efficiently to the velocities in excess of 10 km/s by means of detonation waves or other shock-induced combustion modes. This concept, developed at University of Washington[1], can be scaled for projectile masses ranging from grams to hundreds of kilograms and has the potential for a number of applications, such as hypervelocity impact physics, direct launch to the orbit of acceleration-insensitive payloads, and hypersonic testing. Although several ram accelerator operation modes have been proposed, the analysis is centered on the "oblique detonation" mode shown in Fig. 1.3. The gas dynamic principles of the oblique detonation ram accelerator are similar to those of the ODWE concept; however, the device is operated in a different manner.

In such combustion chambers, combustion would be performed in the mode of interaction between (i) highly-turbulent diffusion flames and (ii) a number of shock wavelets. Exothermic reactions occurring behind a leading shock wave in a hypersonic premixed gas mixture generate the phenomena useful for studying the flow-chemistry interaction features. This mode of combustion, i.e. a steadily-maintained detonation in front of a blunted “holder”, has not been studied widely.

---

[1] See Hertzberg et al. (1988)

The author has been active in exploring the fundamental properties of a standing oblique detonation (SOD) from both numerical and theoretical viewpoints.

It is the purpose of this study to examine the characteristics of the standing oblique detonation (SOD), in order to clarify the relations among thermodynamics, chemical kinetics and fluid mechanics, because the underlying physics of SOD has not been fully investigated. Study of the relation between fluid and chemistry should determine the required parameters under which a stable SOD with acceptable total pressure loss can be sustained.

In this dissertation, the basic physics of supersonic flows with combustion chemistry is studied by numerical simulations. Focus is, at first, placed on the basic characteristics of SOD supported by a two-dimensional blunted wedge. The flow features of SOD are qualitatively studied by changing various parameters; the scale of the wedge tip radius, the wedge angle, and the Mach number and temperature of the incoming flow. A series of simulation reveals the underlying physics of SOD, based on the simplified reaction mechanism and the H_2-O_2 reaction mechanism. Second, one of the famous phenomena of shock-induced combustion, which has a periodic "instability" around a hypersonic flying axisymmetric blunted projectile body, is treated. The flow is worthy of investigation because it contains complex interactions between combustion chemistry and fluid dynamics, and the flowfield should be clarified for further research of SOD.

CHAPTER II

NUMERICAL FORMULATION

The physical model for flowfield analysis is described by the Euler equations, and the species continuity equations or the equations consisting of the simplified two-step chemical reaction mechanism. The simplified chemical reaction mechanism is used to qualitatively understand the phenomena, and the $H_2 - O_2$ reaction mechanism consisting of elementary reactions is used to quantitatively discuss and verify the flowfield in detail. In Chapter II, the numerical scheme, the reaction models and the numerical techniques used in the present study are described.

II. 1 Simplified Two-Step Chemical Reaction Mechanism

In the present calculation, the following set of model reactions[1] is considered, instead of handling a realistic chemical system undergoing a number of elementary reactions. It has been proved that the following model is useful for the simulation of a realistic oxyhydrogen mixture diluted by Argon/Helium:

$$2H_2 + O_2 + 7Ar/He.$$

The induction time and the other chemical parameters were carefully adjusted to the existing shock tube data. Utilized assumptions are as follows:

(I) The gas is perfect with adiabatic index $\gamma = 1.4$, generating a constant exothermicity.

(II) The gas is non-diffusive, i.e. the Euler equations are used.

(III) The chemical reaction consists of the following two stages:

---

[1] See Korobeinikov et al. (1972)

a) The induction stage where no heat is released, while the progress variable α varies monotonically from 1 to 0.

b) The exothermic reaction stage that is faster than the induction reaction. This stage is triggered at the instant $\alpha = 0$ when the other progress variable β starts decreasing from 1 to its equilibrium value $\beta_{eq} > 0$. The amount of heat release is proportional to the change of the progress variable β.

For an Argon/Helium-diluted stoichiometric oxyhydrogen mixture, the source terms ω_α and ω_β are expressed as:

Induction;

$$\omega_\alpha \equiv \frac{d\alpha}{dt} = -\frac{1}{\tau_{ind}} = -k_1 \rho \exp\left(-\frac{E_1}{RT}\right). \tag{2.1}$$

Exothermic reaction;

$$\omega_\beta \equiv \frac{d\beta}{dt} = \begin{cases} = 0, & \alpha > 0 \\ = -k_2 P^2 \left[\beta^2 \exp\left(-\frac{E_2}{RT}\right) - (1-\beta)^2 \exp\left(-\frac{E_2 + Q}{RT}\right)\right], & \alpha \le 0. \end{cases} \tag{2.2}$$

The above model is coupled with the following equations.

$$\frac{D(\rho\alpha)}{Dt} = \rho\omega_\alpha, \quad \frac{D(\rho\beta)}{Dt} = \rho\omega_\beta. \tag{2.3}$$

Here the reaction parameters[1] appearing in Eqs. (2.1) and (2.2) are selected as

---

[1] The parameters of the simplified reaction model are selected from Taki and Fujiwara (1978) and Wang and Fujiwara (1988)

$$\begin{aligned} &k_1 = 3.0 \times 10^{11} cm^3 / g / sec, \\ &k_2 = 1.875 \times 10^{-8} cm^4 / dyn^2 / sec, \\ &E_1 / R = 9800K, \\ &E_2 / R = 2000K, \\ &Q = 4.0 \times 10^{10} erg / g, \end{aligned} \tag{2.4}$$

to fit the shock-tube data of $2H_2 + O_2 + 7Ar / He$ mixture, where the uniform flow pressure and temperature are 0.1 atm and 288.64 K. Here, k_1 and k_2 are the reaction rate constants, and E_1 and E_2 of Eqs. (2.1) and (2.2) are the activation energies. Q is the exothermic energy per unit mass. The exothermic reaction after the induction time is represented by the rapid decrease of β from 1 to an equilibrium value β_{eq}. The C-J Mach number $M_{C\text{-}J}$ and the equilibrium value β_{eq} are given in this gas mixture as follows:

$$M_{C\text{-}J} = 4.8, \quad \beta_{eq} = 0.2315. \tag{2.5}$$

The governing system of equations is written for inviscid flows and axisymmetric geometry, under ideal (constant γ) and adiabatic assumptions. Pressure is described bellow:

$$P = (\gamma - 1)e - \rho\beta Q - 0.5\rho(u^2 + v^2). \tag{2.6}$$

The traveling distance L^* of a fluid particle during the induction time can roughly be estimated, using the velocity u_2 immediately behind the shock wave, as $L^* = u_2 \cdot \tau_{ind}$. Note that L^*, which is the induction length of the plane Chapman-Jouguet detonation, is of very small size, e.g. 3.65 mm at $P_\infty = 0.1$ atm and $T_\infty = 288.64$ K for the gas mixture diluted by Argon.

Our experience indicated that the grid resolution is important to describe the wave interaction and the behavior of the reaction progress. The simplified two-step chemical reaction mechanism does not require excessive computer time and memory, which allows us to use very fine mesh distributions. This is another reason to use the simplified mechanism. In Chapters III, V and VI, the simplified reaction mechanism is used to clarify the mechanism of the periodic unsteadiness qualitatively.

II. 2 H_2-O_2 Reaction Mechanism

The oxyhydrogen combustion mechanisms used in this study are taken from the work of Drummond and Hassaini (1987) and Wilson and MacCormack (1990). The former combustion mechanism consists of 7 reacting species (H_2, O_2, H, O, OH, H_2O and HO_2) and 9 reactions, which are sited in Table 2.1 and used in Chapter III. The latter reaction set was developed for supersonic combustion, basically consisting of 13 reacting species (H_2, O_2, H, O, OH, H_2O, HO_2, H_2O_2, N, NO, NO_2, HNO and N_2) and 33 reactions, and was called the modified Jachimowski's combustion mechanism.[1] However, this study uses only 8 species (H_2, O_2, H, O, OH, H_2O, HO_2 and H_2O_2) and 19 reactions, which are sited in Table 2.2, to describe the combustion mechanism because the nitrogen reactions are not so important at around Mach number 5. Therefore, all the nitrogen reactions are omitted in this study, although the species N, NO and HNO become important at higher Mach numbers. In Chapter VII, the H_2-O_2 reaction mechanism is used to quantitatively discuss and verify the oscillating mechanism of the flowfield, which is proposed in Chapter V.

The molecular constants and thermochemical data used for the nine species in H_2/Air gas model are given in Appendix A, and general formulas to calculate the chemical source term are given in Appendix B, in detail.

---

[1] See Jachimowski (1988)

TABLE 2.1 $H_2 - O_2$ Reaction Mechanism

k	*Reaction*	*A*	*n*	*E*
(1)	$H_2 + O_2 = OH + OH$	1.70×10^{13}	*0.*	*48150*
(2)	$H + O_2 = OH + O$	1.42×10^{13}	*0.*	*16400*
(3)	$OH + H_2 = H_2O + H$	3.16×10^{7}	*1.8*	*3030*
(4)	$O + H_2 = OH + H$	2.07×10^{14}	*0.*	*13750*
(5)	$OH + OH = O + H_2O$	5.50×10^{13}	*0.*	*7000*
(6)	$H + OH + M = H_2O + M$	2.21×10^{23}	*-2.*	*0*
(7)	$H + H + M = H_2 + M$	6.53×10^{18}	*-1.*	*0*
(8)	$H + O_2 + M = HO_2 + M$	3.20×10^{18}	*-1.*	*0*
(9)	$HO_2 + OH = H_2O + O_2$	5.00×10^{13}	*0.*	*1000*

$k_{f_k} = AT^{n_k} exp(-E_k / RT)$; units are in seconds, moles, centimeters^3, calories and Kelvins.

TABLE 2.2 $H_2 - O_2$ Reaction Mechanism

k	*Reaction*	*A*	*n*	*E*
(1)	$H_2 + O_2 = HO_2 + H$	1.00×10^{14}	*0.*	*56000*
(2)	$H + O_2 = OH + O$	2.60×10^{14}	*0.*	*16800*
(3)	$O + H_2 = OH + H$	1.80×10^{10}	*1.*	*8900*
(4)	$OH + H_2 = H + H_2O$	2.20×10^{13}	*0.*	*5150*
(5)	$OH + OH = O + H_2O$	6.30×10^{12}	*-2.*	*1090*
(6)	$H + OH + M = H_2O + M$	2.20×10^{22}	*-1.*	*0*
(7)	$H + H + M = H_2 + M$	6.40×10^{17}	*-0.6*	*0*
(8)	$H + O + M = OH + M$	6.00×10^{16}	*0.*	*0*
(9)	$H + O_2 + M = HO_2 + M$	2.10×10^{15}	*0.*	*-1000*
(10)	$O + O + M = O_2 + M$	6.00×10^{13}	*0.*	*-1800*
(11)	$HO_2 + H = OH + OH$	1.40×10^{14}	*0.*	*1080*
(12)	$HO_2 + H = H_2O + O$	1.00×10^{13}	*0.*	*1080*
(13)	$HO_2 + O = O_2 + OH$	1.50×10^{13}	*0.*	*950*
(14)	$HO_2 + OH = H_2O + O_2$	8.00×10^{12}	*0.*	*0*
(15)	$HO_2 + HO_2 = H_2O_2 + O_2$	2.00×10^{12}	*0.*	*0*
(16)	$H + H_2O_2 = H_2 + HO_2$	1.40×10^{12}	*0.*	*3600*
(17)	$O + H_2O_2 = OH + HO_2$	1.40×10^{13}	*0.*	*6400*
(18)	$OH + H_2O_2 = H_2O + HO_2$	6.10×10^{12}	*0.*	*1430*
(19)	$H_2O_2 + M = OH + OH + M$	1.20×10^{17}	*0.*	*45500*

$k_{f_k} = AT^{n_k} exp(-E_k / RT)$; units are in seconds, moles, centimeters^3, calories and Kelvins.

Third body efficiencies relative to N_2:

Reaction (6) $H_2O = 6.0.$
Reaction (7) $H_2O = 6.0;$ $H_2 = 2.0.$
Reaction (8) $H_2O = 5.0.$
Reaction (9) $H_2O = 16.0;$ $H_2 = 2.0.$
Reaction (19) $H_2O = 15.0.$

II. 3 Governing Equations in Conservation Form

In the present study, a simplified form of equations is adopted under the assumption of axisymmetric flow for Chapters V, VI and VII. The derivation from the original three-dimensional form is described in Appendix C in detail. The final form of the governing system of equations that is transformed to the general curvilinear coordinate system is written below for inviscid flows over an axisymmetric geometry:

$$\frac{\partial \hat{Q}}{\partial \tau} + \frac{\partial \hat{E}}{\partial \xi} + \frac{\partial \hat{F}}{\partial \eta} + \lambda \hat{H} = \hat{S}, \tag{2.7}$$

where $\hat{E}$ and $\hat{F}$ are the inviscid flux vectors in ξ- and η-directions respectively. $\hat{S}$ is the chemical reaction source vector and $\hat{H}$ is the axisymmetric source term vector. λ is 0 for the two-dimensional governing equations, while λ is 1 for the axisymmetric governing equations.

The simplified two-step chemical reaction mechanism[1] is used to qualitatively understand the phenomena in Chapters III, V and VI. For the governing equations consisting of Euler equations and the simplified reaction mechanism, the inviscid flux vector, the axisymmetric source vector and the chemical source vector are

$$\hat{Q} = J^{-1}\begin{pmatrix} \rho \\ \rho u \\ \rho v \\ e \\ \rho\beta \\ \rho\alpha \end{pmatrix}, \quad \hat{E} = \begin{pmatrix} \rho U \\ \rho u U + \xi_x P \\ \rho v U + \xi_y P \\ (e+P)U \\ \rho\beta U \\ \rho\alpha U \end{pmatrix}, \quad \hat{F} = \begin{pmatrix} \rho V \\ \rho u V + \eta_x P \\ \rho v V + \eta_y P \\ (e+P)V \\ \rho\beta V \\ \rho\alpha V \end{pmatrix},$$

---

[1] More details on the simplified reaction mechanism are found in Chapter II.1

$$\hat{H} = J^{-1}\frac{\rho v}{y}\begin{pmatrix} 1 \\ u \\ v \\ (e+P)/\rho \\ \beta \\ \alpha \end{pmatrix}, \quad \hat{S} = J^{-1}\begin{pmatrix} 0 \\ 0 \\ 0 \\ 0 \\ \rho\omega_\beta \\ \rho\omega_\alpha \end{pmatrix}, \tag{2.8}$$

where U and V are the contravariant velocities given as

$$U = \xi_x u + \xi_y v, \quad V = \eta_x u + \eta_y v, \tag{2.9}$$

and the metrics and the Jacobian J are given as

$$\begin{gathered} \xi_x = Jy_\eta, \quad \xi_y = -Jx_\eta, \quad \eta_x = -Jy_\xi, \quad \eta_y = Jx_\xi, \\ \frac{1}{J} = x_\xi y_\eta - x_\eta y_\xi, \end{gathered} \tag{2.10}$$

where the variables α and β are the reaction progress variables, u and v are ξ- and η- component of the mass-averaged fluid velocity, e is the energy, P is the pressure, and ω_α and ω_β are the mass rate of production due to chemical reaction.

In Chapters III and VII, the H_2-O_2 reaction mechanism consisting of elementary reactions is used to quantitatively discuss the flowfield. For the governing equations, the inviscid flux vector, the axisymmetric source vector and the chemical source vector are

$$\hat{Q} = J^{-1}\begin{pmatrix} \rho \\ \rho u \\ \rho v \\ E \\ \rho_i \end{pmatrix}, \quad \hat{E} = J^{-1}\begin{pmatrix} \rho U \\ \rho u U + \xi_x P \\ \rho v U + \xi_y P \\ (E+P)U \\ \rho_i U \end{pmatrix}, \quad \hat{F} = J^{-1}\begin{pmatrix} \rho V \\ \rho u V + \eta_x P \\ \rho v V + \eta_y P \\ (E+P)V \\ \rho_i V \end{pmatrix},$$

$$\hat{H} = J^{-1}\frac{\rho v}{y}\begin{pmatrix} 1 \\ u \\ v \\ (E+P)/\rho \\ 1 \end{pmatrix}, \quad \hat{S} = J^{-1}\begin{pmatrix} 0 \\ 0 \\ 0 \\ 0 \\ \omega_i \end{pmatrix}, \qquad (2.11)$$

where ρ_i is the density of species i and ω_i is the mass rate of production of species i due to chemical reaction.

II. 4 Solution Algorithm

These equations are solved by a finite difference method and the unsteady solutions are obtained at each time step through the time marching procedure. A non-MUSCL-type TVD upwind algorithm developed by Yee (1987) is used in the present simulation. This algorighm is second-order accurate in time and in the space for the system of equations.

The explicit difference scheme of Eq. (2.7) is used for the simplified two-step chemical reaction mechanim, which is written as

$$\hat{U}^{n+1}_{j,k} = \hat{U}^{n}_{j,k} - \frac{\Delta t}{\Delta \xi}\left(\tilde{E}^{n}_{j+1/2,k} - \tilde{E}^{n}_{j-1/2,k}\right) - \frac{\Delta t}{\Delta \eta}\left(\tilde{F}^{n}_{j,k+1/2} - \tilde{F}^{n}_{j,k-1/2}\right) - \Delta t \hat{H}^{n}_{j,k} + \Delta t \hat{S}^{n}_{j,k}, \qquad (2.12)$$

where all terms are evaluated at the time n.

The point-implicit finite difference scheme of Eq. (2.7) is used for the

$H_2 - O_2$ reaction mechanim, which is written as

$$D^n_{j,k} \Delta \hat{U}_{j,k} = -\frac{\Delta t}{\Delta \xi}\left(\tilde{E}^n_{j+1/2,k} - \tilde{E}^n_{j-1/2,k}\right) - \frac{\Delta t}{\Delta \eta}\left(\tilde{F}^n_{j,k+1/2} - \tilde{F}^n_{j,k-1/2}\right) - \Delta t \hat{H}^n_{j,k} + \Delta t \hat{S}^n_{j,k}, \tag{2.13}$$

$$D^n_{j,k} = \left(I - \frac{\Delta t}{2}\frac{\partial \hat{S}}{\partial \hat{U}}\right)^n_{j,k}, \tag{2.14}$$

$$\hat{U}^{n+1}_{j,k} = \hat{U}^n_{j,k} + \Delta \hat{U}_{j,k}, \tag{2.15}$$

where the approximations are referred as "point-implicit" because all convection terms are evaluated at the time n, whereas the source term from chemical reaction is evaluated at the time $n+1$.

The Jacobians of the chemical source term $\partial \hat{S} / \partial \hat{U}$ in Eq. (2.14) both for the simplified reaction mechanism and the $H_2 - O_2$ reaction mechanism are written in Appendix D in detail.

The functions $\tilde{E}_{j+1/2,k}$ and $\tilde{F}^n_{j,k+1/2}$ are the numerical fluxes in ξ- and η-directions evaluated at $(j+1/2,k)$ and $(j,k+1/2)$, respectively. Typically, $\tilde{E}_{j+1/2,k}$ for a non-MUSCL TVD algorithm can be expressed as

$$\tilde{E}_{j+1/2,k} = \frac{1}{2}\left(\hat{E}_{j,k} + \hat{E}_{j+1,k} + R_{j+1/2,k}\Phi_{j+1/2,k}\right), \tag{2.16}$$

where $R_{j+1/2,k}$ is the matrix whose columns are right eigenvectors of flux Jacobian $\partial \hat{E} / \partial \hat{U}$. The elements of the vector $\Phi_{j+1/2,k}$ can be written as

$$\left(\phi^l_{j+1/2}\right)^U = \sigma\left(a^l_{j+1/2}\right)\left(g^l_{j+1} + g^l_j\right) - \psi\left(a^l_{j+1/2} + \gamma^l_{j+1/2}\right)\alpha^l_{j+1/2}, \tag{2.17}$$

where $a^l_{j+1/2}$ is the l-th eigenvalue of $\partial \hat{E} / \partial \hat{U}$ and $\alpha^l_{j+1/2}$ is the difference vector of the characteristic variables in the local ξ-direction denoted, for example, as

$$\alpha^l_{j+1/2} = R^{-1}_{j+1/2}\left(\hat{U}_{j+1} - \hat{U}_j\right). \tag{2.18}$$

$a^l_{j+1/2}$, $R_{j+1/2,k}$ and $\Phi_{j+1/2,k}$ are described by Yee (1987) in detail. $\psi(z)$ is an entropy correction function that is expressed as

$$\psi(z) = \begin{cases} |z| & |z| \geq \delta_1 \\ \left(z^2 + \delta_1^2\right)/2\delta_1 & |z| < \delta_1 \end{cases}, \tag{2.19}$$

and the functions $\sigma(z)$ and $\gamma^l_{j+1/2}$ are expressed as

$$\sigma(z) = \frac{1}{2}\left[\psi(z) - \lambda z^2\right],$$

$$\gamma^l_{j+1/2} = \sigma\left(a^l_{j+1/2}\right)\begin{cases} \left(g^l_{j+1} - g^l_j\right)/\alpha^l_{j+1/2} & \alpha^l_{j+1/2} \neq 0 \\ 0 & \alpha^l_{j+1/2} \neq 0 \end{cases}. \tag{2.20}$$

δ_1 is a function that defines the range of entropy correction, and should be a function of the contravariant velocity and the corresponding sound speed for the blunt body computations. The form of the function used here is

$$\delta_1 = \tilde{\delta}\left(|U| + |V| + c\sqrt{\xi_x^2 + \xi_y^2 + \eta_x^2 + \eta_y^2}\right), \tag{2.21}$$

with a constant $\tilde{\delta}$ set to 0.15.

Several types of the form of the limiter functions are suggested by Yee (1987). In the present study, the following limiter functions are used:

$$g^l_j = min\,mod\left(\alpha^l_{j-1/2}, \alpha^l_{j+1/2}\right), \tag{2.22}$$

where the minmod function is given as

$$minmod(x,y) = sgn(x) \cdot max\left\{0, \left[|x|, y \cdot sgn(x)\right]\right\}. \tag{2.23}$$

- *Approximate Riemann Solvers (Generalized Roe's Average)*

Among the various approximate Riemann solvers for a perfect gas, the most common one is the Roe's average because of its simplicity and its ability to satisfy the jump conditions. However, Roe's "property U conditions" cannot be uniquely satisfied for nonperfect gases. Various alternatives were proposed for real gases. Only the final solutions used in the present computations are described here; see the original paper by Wada et al. (1989) in detail. For the two-dimensional and axisymmetric equations, the Roe's average can be obtained as

$$\overline{u} = \frac{u^L + Du^R}{1+D}, \quad \overline{v} = \frac{v^L + Dv^R}{1+D}, \quad \overline{Y_i} = \frac{Y_i^L + DY_i^R}{1+D}, \quad D = \sqrt{\frac{\rho^R}{\rho^L}}, \tag{2.24}$$

and the generalized Roe averages, used in the cell-interface evaluation of R, R^{-1} and Φ, can be obtained as

$$\begin{gathered}
\overline{P_{\rho R}} = \frac{P_\rho^L + DP_\rho^R}{1+D}, \quad \overline{P_{ER}} = \frac{P_E^L + DP_E^R}{1+D}, \quad \overline{P_{\rho_i R}} = \frac{P_{\rho_i}^L + DP_{\rho_i}^R}{1+D}, \\
\overline{H} = \frac{H^L + DH^R}{1+D}, \quad \overline{P_\rho} = \overline{P_{\rho R}} - k\Delta\rho, \quad \overline{P_{\rho_i}} = \overline{P_{\rho_i R}} - k\Delta\rho_i, \\
\overline{P_E} = \overline{P_{ER}} + k\left\{\overline{u}\,\Delta(\rho u) + \overline{v}\,\Delta(\rho v) - \Delta E\right\}, \\
k = \frac{\overline{P_{\rho R}}\Delta\rho - \overline{P_{ER}}\left\{\overline{u}\,\Delta(\rho u) + \overline{v}\,\Delta(\rho v) - \Delta E\right\} + \sum_{j=1}^{N}\left(\overline{P_{\rho_j R}}\Delta\rho_j\right) - \Delta\rho}{(\Delta\rho)^2 + \left\{\overline{u}\,\Delta(\rho u) + \overline{v}\,\Delta(\rho v) - \Delta E\right\}^2 + \sum_{j=1}^{N}\left(\Delta\rho_j\right)}.
\end{gathered} \tag{2.25}$$

CHAPTER III

STANDING OBLIQUE DETONATION SUPPORTED BY TWO-DIMENSIONAL BLUNTED WEDGE

A study of standing oblique detonations can be useful in understanding combustion problems as an extreme of premixed burning in contrast to diffusive burning, since the actual combustion occurs in an intermediate regime. In 1960s to 1970s, many experiments[1] on hypersonic flying projectiles have been reported for understanding hypersonic combustion. During last few years, the numerical investigations about the shock-induced combustion and oblique detonation have been also reported[2].

There are a number of questions yet to be answered, where some of the important ones are:

(I) Whether a standing oblique detonation (SOD) is possible ?

(II) What are the critical parameters for SOD to exist ? Incident Mach number, size of the holder, blunted or pointed cone or a two-dimensional wedge, exothermicity and chemical reaction rates ?

(III) Whether the well-known triple shock structure always existing in a Chapman-Jouguet detonation persists in a standing oblique detonation ?

To answer the above questions, the characteristics of a standing oblique detonation over a two-dimensional blunted wedge are investigated in the following

---

[1] See Lehr (1972), McVey and Toong (1971), Alpert and Toong (1972), Behrens et al. (1965), Ruegg and Dorsey (1962)

[2] See Lee and Deiwert (1990), Wilson and MacCormack (1990), Yungster et al. (1991), Matsuo and Fujiwara (1988), Matsuo and Fujiwara (1991)

computations. First, the flow features of SOD are studied by changing the scale of the wedge tip radius, using the simplified two-step chemical reaction mechanism. Second, the characteristics of SOD are tested by a series of simulations, changing the parameters, which are the wedge tip radius, the wedge angle and the Mach number and temperature of the incoming flow, using the $H_2 - O_2$ reaction mechanism.

III. 1 Computational Domain and Grid Distributions

Figure 3.1 is the schematic picture showing the computational aspect of the present simulation. The solution is obtained on the grid system, consisting of 71 points in ξ-direction and 51 points in η-direction. In ξ-direction, 15 points are distributed on the blunted tip portion with equal spacings, while 55 points are distributed on the straight wedge part also with equal spacings. In η-direction, the grid spacing becomes exponentially smaller near the body surface. A technique of locally adaptive grids is used to capture the sharp leading bow shock and to resolve the rapid chemical reaction behind the shock wave.

III. 2 Boundary and Initial Conditions

The boundary conditions on each boundary of the computational domain (see in Fig. 3.1) are described as follows:

The variables at the inflow boundary AB are fixed to the freestream ones as

$$f\big|_{k=k_{max}} = f\big|_{\infty}, \tag{3.1}$$

where f denotes the dependent variables. On the outflow boundary AD, the variables are given by the zero-th order extrapolation from the internal grid points as

$$f\big|_{j=j_{max}} = f\big|_{j=j_{max}-1}. \tag{3.2}$$

Variables on the body surface CD are given by the slip and adiabatic wall conditions as

$$\begin{aligned} U\big|_{k=1} &= 2U\big|_{k=2} - U\big|_{k=3}, \\ V\big|_{k=1} &= 0, \\ P\big|_{k=1} &= P\big|_{k=2}, \\ T\big|_{k=1} &= T\big|_{k=2}. \end{aligned} \tag{3.3}$$

In addition, non-catalyticity $\partial\alpha / \partial n = \partial\beta / \partial n = 0$ is assumed.

On the axis of symmetry BC, zero-th order extrapolation is used since the condition represents no-flux across the axis:

$$f\big|_{j=1} = f\big|_{j=2}. \tag{3.4}$$

As the initial condition for the computation of reacting flows, the solution of non-reacting flows (the chemical source term $S = 0$) is used.

III. 3 Numerical Study Using Simplified Reaction Mechanism

The characteristics of a standing oblique detonation over a two-dimensional blunted wedge are studied by changing the holder radius.

Calculations are performed using the following parameters:

(I) Incident Mach number is 6, while the Chapman-Jouguet Mach number (M_{C-J}) of the premixed gas is 4.8.

(II) Wedge tip radii of curvature are $L = L^*$ and $3L^*$.

The geometry of the calculated holder is kept unchanged throughout the simulation even though the scales are different.

Wedge tip radius L^*

First, the result for the wedge tip radius L^* is presented. Figure 3.2 gives the temperature contour plots of the non-reacting gas; this was used as an initial condition to the reacting flow. Figure 3.3 is the temperature contour plots of the reacting gas, for which a schematic picture is given in Fig. 4 to help understand the flowfield of Fig. 3.3. Important is the separation between the bow shock and the reaction front: The reaction front is clearly observed between the oblique shock wave and the body surface in Fig. 3.3. In particular, the separation becomes linearly wider in the downstream direction.

Comparison between the temperature contour plots in Figs. 3.2 and 3.3 indicates that the heat release pushes the bow shock away from the body surface, giving a longer shock standoff distance; the tendency to increase the pressure by heat release is compensated by the increased shock standoff distance, thereby keeping the balance of momentum across the bow shock. Concerning the shock angle, the value of the straight portion in Fig. 3.2 is 42 degrees, while the angle in Fig. 3.3 is 50 degrees. Because the flow is inviscid, the flow behind the straight oblique shock wave must be parallel to the wedge angle (30 degrees). In addition, the flow must satisfy the shock relation of the shock angle 50 degrees, where the normal component of the Mach number is 4.6, as shown in Fig. 3.5. The temperature behind the oblique shock is about five times (1443.2 K) that of the incoming flow (288.64 K). The temperature behind the straight oblique shock is uniform, so that the induction time for the exothermic reaction must be uniform behind the entire straight portion of the oblique shock. As drawn in Figs. 3.4 and 3.5, the angles of the oblique shock, the reaction front and the wedge angle are all different, although the induction time and length must be the same at any portion of the flowfield except for the nose region. The explanation of this discrepancy is given below.

Figure 3.6 shows the normal shock relation (for $\gamma = 1.4$), i.e. the incident Mach number M_∞ versus the temperature ratio T_2/T_∞ and the induction length $l(T_2)/L^*$. The induction length l is given by multiplying the velocity u_2 immediately behind the normal shock and the induction time τ_{ind}, which can be derived from Eq. (2.1) using the flow variables behind the normal shock. The induction length is about $1.5\,L^*$ for the normal Mach number $M_\infty = 4.6$. The temperature behind the oblique shock is uniform, so that the exothermic reaction should occur uniformly $1.5\,L^*$ downstream normal to the oblique shock, as seen in Fig. 3.7. However, the large velocity component parallel to the oblique shock exists, and therefore the particle path is not normal to the oblique shock, as seen schematically in Fig. 3.8; this necessitates a long straight oblique shock before the shock and reaction front become parallel. If the larger calculated domain was used in the present study, the solution must have been the steady and coupled (ZND-type) SOD, where the position of the reaction front can be estimated by the ZND detonation theory. Since the shock on the stagnation streamline in front of the blunted portion is much stronger than the oblique shock, influence of the flowfield in front of the blunted portion has to be considered for the discussion of SOD structure.

Wedge tip radius $3\,L^*$

Figure 3.9 gives the temperature contour plots for the wedge tip radius $3\,L^*$. As seen in Fig. 3.9, the bow shock and the reaction front are completely coupled: A typical detonation front, which consists of the coupled shock and reaction front, is established; it gradually moves forward with an almost constant speed, as seen in

Figs. 3.10 (a) and (b). The shock standoff distance is greatly changed during this short time interval.

Note that the difference between Fig. 3.3 and Fig. 3.9 is only the curvature of the wedge tip. What caused the sudden change? The shock angle in Fig. 3.9 is 55 degrees, and it locally exceeds 70 degrees. The shock angle in Fig. 3.10 (a) is 65 degrees, and is more than 70 degrees in Fig. 3.10 (b). Assume that the angle of the oblique shock is 50 degrees for the case of wedge tip radius $3L^*$. The flow conditions behind the oblique shock are the same as those in the wedge tip radius L^*, so that the similar detonation structure would be established. However, the relative induction length (to the shock standoff distance) is shorter in this case because the induction length is unchanged and yet the shock standoff distance is three times longer. Thus, the burnt gas region is relatively much wider behind the bow shock around the increased wedge tip radius. Therefore, the oblique shock is pushed further away from the body surface by the exothermicity, and the shock angle is changed. Finally, the shock angle is increased to 70 degrees, the Mach number normal to the oblique shock becomes 5.64, which is higher than the C-J value 4.8 of the premixed gas; the oblique shock created by the wedge is stronger than that of the C-J detonation. Considering the oblique shock relation, the relations among the incident Mach number, deflection angle and shock angle can determine the existence limit of the attached oblique shock. Figure 3.11 gives the shock polar curve in terms of the $\theta-\beta$ (deflection angle and wave angle) relation for the incident Mach number 6, where the limiting angle of the weak shock is 67 degrees. If the shock angle is higher than 67 degrees, the Mach number behind the shock becomes subsonic, making it impossible to obtain the steady solution.

Discussion

The characteristics of SOD supported by the two-dimensional wedge were studied. When the radius is L^*, the reaction front is stationary and completely decoupled from the leading bow shock. The reaction front gets coupled with the bow shock in the case of the wedge tip radius $3L^*$. In addition, the coupled shock-flame (detonation) gradually moves forward. This phenomenon can be explained by the limiting angle of the oblique shock wave. The heat release changes the shock angle and, as a result, we run into the regime where there is no stationary solution, i.e. the shock angle exceeds the limit for the given incoming Mach number and the wedge angle. The present study confirms that there are critical values for the incident Mach number and the wedge tip radius for the establishment of SOD in a hypersonic premixed gas.

III. 4 Characteristics of SOD Using H_2-O_2 Mechanism

In this section, a numerical analysis based on the H_2-O_2 Mechanism is performed. The incoming hypersonic flow consists of a uniformly-premixed stoichiometric oxyhydrogen mixture diluted by 70% of Argon at a Mach number higher than its Chapman-Jouguet value 4.8. The effect of the wedge angle for the establishment of SOD is investigated by a series of the simulations. Calculations are performed in the following parameter range: $\theta = 30$, 35 and 40 degrees for the incoming Mach number 6.0, the temeprature 298 K and the pressure 0.1 atm.

When the wedge angle is increased, the angle of the oblique shock wave is also increased and the distance between the bow shock wave and the flame becomes shorter. Finally, the shock-deflagration system is changed to the coupled SOD from the decoupled one. The computed result in Fig. 3.14 shows the unsteady phenomenon. During the time evolution of the computation, the coupled shock-flame (detonation) gradually moves forward, as shown by the result in Figs. 3.9 and 3.10.

The bow shock proceeds forward never to give a stationary position, whereas a steady oblique shock in front of the blunted wedge was obtained in a non-reacting flow. As is mentioned in the last section, this phenomenon can be explained by the limiting angle of the oblique shock wave. After several attempts, the critical wedge angle is found to be θ = 37-40 degrees. This type of criterion is also suggested by Pratt, Humphrey and Glenn (1987), where existence of solution can not be explained easily without performing the numerical calculation.

III. 5 Scaling Effect of SOD around Axisymmetric Body

In this section, scaling effect of SOD around an axisymmetric blunted body is studied. The incoming hypersonic flow consists of a uniformly-premixed stoichiometric oxyhydrogen mixture diluted by 70% Argon at a Mach number higher than its Chapman-Jouguet value 4.8.

Calculations are performed in the following parameter range:

(i) Incident Mach number $M_\infty = 6$, temperature $T_\infty = 288.65$ and pressure $P_\infty = 0.1$ atm.

(ii) Tip radius of curvature $L^* = 2.25$ and 22.5 mm.

As shown in Figs. 3.15 and 3.16, a completely coupled SOD has been obtained by increasing the tip radius of sphere (attached to the downstream cylinder) from 2.25 mm to 22.5 mm (by a factor 10), in a $M_\infty = 6$ incident oxyhydrogen mixture. The scaling effect of SOD is clearly observed in the computations, and the effect in the two-dimensional blunted wedge in Chapter III.3 has been confirmed.

CHAPTER IV

BALLISTIC RANGE EXPERIMENTS AND PREVIOUSLY-PROPOSED MECHANISM

One of the famous phenomena of shock-induced combustion is a periodic "instability" around a hypersonic flying projectile body. There were many reports about such a periodic instability in physical experiments[1] from 1960s to early 1970s. Excellent data for studying supersonic combustion/detonation were provided by ballistic range experiments conducted in 1960s and 1970s. In these experiments, projectiles were fired in different kinds of premixed fuel/air mixtures and shock/deflagration or detonation structures around the projectiles were observed.

Ruegg and Dorsey (1962) investigated the effects of stabilizing combustion and detonation against hypersonic flows by 20 mm diameter spherical missiles in a stoichiometric hydrogen-air mixture. The oscillations with the frequency 0.1 MHz were observed in front of the sphere, when the Mach number was less than 6 at 0.5 atm pressure level, and less than 5 at 0.25 atm pressure level.

Behrens et al. (1965) conducted the ballistic range experiment by firing 9 mm diameter plastic spheres into stoichiometric hydrogen-air and hydrogen-oxygen mixtures at the velocities 1500-3000 m/sec. By firing them at velocities higher than the detonation velocity 1950 m/sec at 0.55 atm, a steady combustion front was established. However, instability appeared at lower projectile velocities.

IV. 1 Shadowgraphs of Lehr

---

[1] See Lehr (1972), McVey and Toong (1971), Alpert and Toong (1972), Behrens et al. (1965), Ruegg and Dorsey (1962)

Experimental shadowgraphs revealed the behavior of density profile in the flowfield of shock induced combustion. The density increase is noticed by the exposure change from light to dark across the bow shock. Across the reaction boundary, on the other hand, the exposure changes from dark to light, indicating a decrease in density. This density decrease is due to the heat release by the exothermic reaction; the gas is self-ignited behind the bow shock, since the temperature increases at the reaction boundary but the pressure remains relatively constant, and therefore the density must decrease.

Figures 4.1-4.5 are the shadowgraph outputs of Lehr's experiment. In his experiment, the projectile body has a 15-mm-diameter hemispherical nose and a cylindrical afterbody. The projectile is flying at Mach number 4.18 to 6.46 (1685 m/sec – 2605 m/sec, see Table 4.1), into a stoichiometric H_2/Air mixture at the initial pressure 0.421 atm (320 torr) and the sound velocity 403 m/s. Projectile Mach numbers are 4.18 (82% of C-J) in Fig. 4.1, 4.79 (94% of C-J) in Fig. 4.2, 5.04 (99% of C-J) in Fig. 4.3, 5.11 (100% of C-J) in Fig. 4.4 and 6.46 (127% of C-J) in Fig. 4.5.

Figures 4.2 and 4.3 have been well known for a long time as typical cases of periodic instablities with high frequency. There are some notable features in the flowfield. The first is the separation between the bow shock and reaction boundary. The second is the corrugated reaction boundary, while the third is the striations in the reaction region which are connected to the corrugated reaction boundary. The fourth is the numerous waves emanating from the corrugated reaction boundary between the bow shock wave and the reaction boundary. The high frequency oscillation, reported to be about 1 MHz, is created in front of the spherical projectile, whereas the lower frequency oscillation (0.15MHz) is observed in Fig. 4.1. The schematic picture of the flowfield structure observed in the shadowgraphs of Lehr's experiments is shown in Fig. 4.6. The periodic phenomena appear only under certain conditions. Although these phenomena have interesting features, their mechanism is not well understood.

Table 4.1 Lehr's Experimental Data

Figure	*Mach No.*	*u (m / sec)*	*u / D*	*f (MHz)*
1.1	4.18	1685	0.82	0.15
1.2	4.79	1931	0.94	0.712
1.3	5.04	2029	0.99	1.04
1.4	5.11	2058	1.00	1.96
1.5	6.46	2605	1.27	–

IV. 2 X-t Diagram by McVey and Toong

Based on the experimental observations and one-dimensional wave interaction theory, a model on the mechanism of periodic unsteadiness was proposed by McVey and Toong (1971), using the x-t diagram of the wave interaction on the stagnation streamline in front of the projectile body (see Fig. 4.7). Basically the one-dimensional galloping mechanism is rare in a detonable gas and the three-dimensional mode appears to be preferred[1]. However, McVey and Toong (1971) and Alpert and Toong (1972) discussed the generation mechanism of the cyclic combustion oscillations having one-dimensional longitudinal movement[2], based on the experimental results of shock-induced combustion and one-dimensional wave interaction theory. In their experimental works, two different unsteady regimes, *regular* and *large-*

---

[1] See Urtiew and Oppenheim (1967), Strehlow and Cohen (1962), Strehlow et al. (1972), Lee (1972), Lee (1977)

[2] One-dimensional instability has been numerically investigated by Fickett and Wood (1966), Abouseif and Toong (1981), Abouseif and Toong (1982)

disturbance regimes, were considered carefully. The *regular* regime corresponds to the periodic instability which will be discussed in this dissertation. In particular, the periodic mechanism was discussed using the history of physical variables on the stagnation streamline where a one-dimensional mode is dominant. Their works give an idea on the cyclic mechanism on longitudinal instability. Figure 4.7 is an x-t diagram between the bow shock wave and the reaction front on the stagnation streamline that explains the wave interaction model proposed by McVey and Toong (1971).

In their model, the instability originates in the induction zone which separates the bow shock from the exothermic reaction front in the nose region of the flowfield. It arises from the varying chemical induction time along the contact discontinuities (entropy waves) which are generated by the interaction of compression waves with the bow shock. The compression waves are generated at the reaction front as a result of spatially-varying reaction rates. The hot gas behind the contact discontinuity begins to react earlier than the gas in front of the contact discontinuity. At a somewhat later time, the contact discontinuity reaches the position of the original reaction front, where there is no more reaction and then a rarefaction wave is generated. According to this model, the wavelength and period are calculated from the flow variables behind the bow shock. Suppose this model represents the real mechanism on the periodic unsteadiness, the observed phenomena in the experiments should be universal, and the same periodic instability must occur in other gas mixtures if the gas is under a satisfied condition.

The term “instability” recalls an unexpected and irregular phenomenon, but the oscillation in the flowfield around the projectile body is very cyclic and the frequency of oscillation is constant. Therefore, not the term “instability” but the term “unsteadiness” will be used in this dissertation to describe such periodic phenomena on the reaction boundary behind the bow shock in Figs. 4.1-4.4.

IV. 3 Motivation of Present Study

Computational approach is becoming widely used for many engineering problems. For the last few years, simulation of hypersonic flows including chemical reactions has become one of the most advanced research topics in the computational fluid dynamics (CFD), because such flows are difficult to physically realize in the experimental apparatus such as wind tunnels or ballistic ranges. Many kinds of numerical techniques which include chemical reactions in high-temperature air have been developed for the study of re-entering space vehicles. Flows inside air-breathing engines have also been a target for study. For such internal flows, chemical reactions between fuel and oxygen occur, and generally the relevant stiffness makes the simulation difficult. Some techniques were developed to avoid such difficulty in the numerical simulations. Nowadays, the computational technique allows us to discuss the flow physics based on the simulated results, and we can find the detailed phenomena associated with chemically reacting flows using CFD.

The shock-induced combustion around a blunt body has been studied for a long time experimentally and analytically, as has been described above. During the last few years, many papers were reported about the research for the eventual use of shock-induced combustion for hypersonic air-breathing engines. With the recent advances in computational fluid dynamics, some studies[1] have been numerical, where the chemically-reacting flowfields were simulated and the results were compared with previous experiments. However, the accuracy and reliability of the software were their only emphasis and flow characteristics were not investigated. Besides, the projectile velocity was much higher than the C-J detonation

---

[1] See Lee and Deiwert (1990), Wilson and MacCormack (1990), Yungster et al. (1991)

speed of the test gas mixture and mainly steady-state solutions with no unsteadiness were only discussed. In this dissertation, the periodic unsteadiness in the shock-induced combustion is numerically investigated to clarify the underlying physics in detail.

Before studying the periodic unsteadiness of the shock-induced combustion numerically, the axisymmetric phenomenon of the periodic unsteadiness is assumed. Figure 4.8 is the off-axis-view shadowgraph of the ballistic-range output of Fig. 4.3. Figure 4.8 reveals that the vertical lines in the reaction region give the effect of reducing the axisymmetric pulsing structure at the reaction boundary to the vertical lines of two-dimensional shadowgraph output. Therefore, all the calculations are done under the axisymmetric assumption.

CHAPTER V

NUMERICAL STUDIES BASED ON A SIMPLIFIED TWO-STEP CHEMICAL REACTION MECHANISM

The experiment with the projectile provides us accurate experimental data, but does not provide the time evolving data (especially on the stagnation streamline) to explain the detailed mechanism for instability. The work in the present chapter qualitatively investigates the physics of the shock-induced combustion by the numerical simulations based on the simplified reaction model, with the focus on the mechanism of the periodic unsteadiness. A fine grid distribution such as 451×451 is used, so that the low amplitude and weak waves around the projectile are reproduced in the numerical simulations.

V. 1 Computational Domain and Grid Distributions

The periodic unsteadiness of the flowfield is created in front of the projectile body and the phenomenon is assumed to be axisymmetric based on the experimental observations. In this study, the computational domain is limited to the region in front of the hemispherical nose of the blunt body. The physical domain for the present computation is shown in Fig. 5.1. One of the grid distributions for the computations is shown in Fig. 5 2. Only every 4th points are plotted so that grid distributions can be easily seen. As observed in Fig. 5.2, the grid spacing for both ξ- and η-directions is equal because the unsteady wave interaction is expected to dominate the periodic phenomena in the entire region behind the bow shock. The final grid distribution is created by changing the grid system that adapts to the location of the bow shock during the computations for non-reacting flow. This reduces the unnecessary grid points in the upstream of the bow shock.

V. 2 Boundary and Initial Conditions

The boundary conditions on each boundary of the computational domain (see in Fig. 5.1) are described as follows:

The variables at the inflow boundary AB are fixed to the freestream ones as

$$f\big|_{k=k_{max}} = f\big|_{\infty} \tag{25}$$

where f denotes the dependent variables. On the outflow boundary AD, the variables are given by the zero-th order extrapolation from the internal grid points as

$$f\big|_{j=j_{max}} = f\big|_{j=j_{max}-1} \tag{26}$$

Variables on the body surface CD are given by the slip and adiabatic wall conditions as

$$\begin{aligned} U\big|_{k=1} &= 2U\big|_{k=2} - U\big|_{k=3} \\ V\big|_{k=1} &= 0 \\ P\big|_{k=1} &= P\big|_{k=2} \\ T\big|_{k=1} &= T\big|_{k=2} \end{aligned} \tag{27}$$

On the axis of symmetry BC, zero-th order extrapolation is used since the condition represents no-flux across the axis as

$$f\big|_{j=1} = f\big|_{j=2} \tag{28}$$

As the initial condition for the computation of the reacting flow, the solution of the non-reacting flow is used.

V. 3 Numerical Study for Various Projectile Body Sizes

As observed in the physical experiment done by Lehr (1972) (see Fig. 4.1-4.4), the reaction boundary is separated from the bow shock wave and the periodic unsteadiness occurs. The $\alpha-\beta$ two-step chemical reaction model used in this study does not exactly describe the behavior of each species of the gas mixture. Especially the treated gas mixture is not same as used by Lehr (1972). However, the basic characteristic of the oscillatory mechanism in the shock-induced combustion is considered to be a more universal phenomenon if the oscillatory mechanism is caused by the wave interaction as is proposed by McVey and Toong (1971).

Throughout our simulations we chose a Mach number of 4.8 as the incoming flow speed because the C-J detonation Mach number of the present gas mixture is 4.8. It is known that the behavior of shock-induced combustion firing around the C-J velocity is unstable; for examples, Lehr's experiment in Fig. 4.3 gives 0.99 for the projectile velocity over the C-J value. In our calculations we have two important parameters, one is the spherical projectile radius and the other is the incoming Mach number. A series of simulations were conducted for various projectile radii and the computed results for three projectile radii, $5L^*$, $7.5\ L^*$ and $10L^*$, are discussed in the following section. In order to understand the flowfield, the density and the $\rho\omega_\beta$ contour plots are used. The $\rho\omega_\beta$ is the chemical source term of equation (2.3). This plot shows the progress of the exothermic reaction.

(a) $5L^*$: Figures 5.1 shows (a): the density contour plots and (b): the $\rho\omega_\beta$ of the projectile radius $5\ L^*$ case. The sudden density change in the region between the bow shock and the body surface indicates the reaction boundary of the burned gas by the exothermic reaction. The $\rho\omega_\beta$ contour plots indicate the region progressing the exothermic reaction. No oscillations are observed along the reaction boundary and the reaction progresses smoothly. The projectile radius $5L^*$ can be understood as the case of a nearly steady solution, because the density residual converges gradually in time during the computation.

(a) *$7.5L^*$:* Figures 5.2 are the contour plots of the projectile radius $7.5L^*$ case. The corrugated reaction boundary along the whole projectile body behind the bow shock are observed in the density contour of Fig. 5.2 (a). The $\rho\omega_\beta$ contour plots in Fig. 5.2 (b) also shows the corrugated reaction region progressing only in front of the spherical projectile. The oscillation is almost periodic and the frequency is high, and the amplitude is relatively low. Comparing Fig. 5.2 (a) and Fig. 5.2 (b), the corrugated reaction boundary in the downstream is regarded as the pattern of the exothermic reaction.

(a) *$10L^*$:* Figures 5.3 show the contour plots of the projectile radius $10L^*$ case. The corrugated reaction boundary is observed behind the bow shock and the phenomenon is periodic, as similar to the density contour plots in the case of $7.5L^*$. However, the frequency in the case of $10L^*$ is lower relative to the projectile radius than that in the case of $7.5L^*$. The waves between the bow shock and the reaction boundary are similar to the waves seen in Fig. 4.2. It seems that the phenomenon in the experiment by Lehr (1972) is reproduced in the present simulations although the gas mixture considered is defferent. The $\rho\omega_\beta$ is generated only in front of the spherical body also in Fig. 5.3 (b), and the region of $\rho\omega_\beta$ forms the corrugated pattern that corresponds to the corrugated reaction boundary observed in the density contour plots. Although the corrugated reaction boundary is seen around the whole body surface, the $\rho\omega_\beta$ is not observed at the downstream of the flowfield. This indicates the termination of the exothermic chemical reaction in the downstream and also evidences that the reaction boundary moves with the fluid. These simulated results show that the tendency in the flowfield of shock-induced combustion in the cases of $7.5L^*$ and $10L^*$ is the same.

The striations in the reaction region seen in Fig. 4.3 are not observed in Figs. 5.2 (a) and 5.3 (a). The post processor by Tamura and Fujii (1990), which simulates the three-dimensional shadowgraph system and generates an output similar to the experiment from the computational result, is used to produce the real three-dimensional computational shadowgraph pattern. The vertical lines or the striations in the reaction region are now observed as is shown in Fig. 5.4.

The relation between the projectile radii and the instabilities were studied and it seems that the instabilities strongly depend on the relation between the shock stand-off distance and the induction length. Compare the induction length on the stagnation streamline in the 3 cases above. The geometry of the projectile is the same, but the physical length is different. It brings the difference of the induction length on the stagnation streamline for the shock stand-off distance. In a chemically reacting flowfield, two types of length scale exist; the body length and the reaction length. Although the projectile radius changes, the chemical reaction induction length does not change but becomes relatively small in comparison with the shock stand-off distance. Since the basic length scale is not unique, both length scales are important for the features of the flow.

V. 4 Detailed Mechanism on Periodic Unsteadiness

- *Time Evolution of Oscillatory Cycle*

Figure 5.5 is the close-up view of the time evolving contour plots of $\rho\omega_\beta$ in the nose region of the spherical projectile showing one cycle from an initiation to a termination of the reaction progress in the corrugated region in the case of projectile radius $10\,L^*$. The cycle is described as:

(1) at the time 2, a new reaction region is generated in front of an original reaction front around the stagnation streamline.

(2) from the time 2 to 5, the new reaction region grows up in front of the original reaction front.

(3) at the time 6, the original reaction front is coupled with the new reaction region.

(4) from the time 6 to 9, the corrugated pattern is moving along the original reaction front.

(5) After the time 10, a new cycle is started and the same cycle is repeated.

The corrugated pattern is moving with the fluid along the projectile body and disappears further from the projectile, where the exothermic chemical reaction does not occur any more.

A series of the time evolving contour plots gives us the unstable phenomenon which is observed in the experiment. Although the oscillatory instabilities are reproduced, the instability mechanism is not well understood in detail from Fig. 5.5. In order to understand the basic phenomenon, the physics on the stagnation streamline is discussed in the next section.

- *Wave Interaction*

The mechanism for the periodic unsteadiness is discussed using the numerical result of the $10\,L^*$ in Fig. 5.3. The history (x-t diagram) of the densitybetween the stagnation point of the body surface and the bow shock wave on the stagnation streamline is shown in Figs. 5.6. Figure 5.6 (a) is the history of the density level plots on the stagnation streamline. Each horizontal line shows the instantaneous density profile. Figure 5.6 (b) is the schematic representation of the Fig. 5.6 (a) in order to help understanding the wave interactions.

Some remarkable features are observed between the reaction front and the stagnation point. In the wave interaction model in Fig. 4.7, the waves propagating toward the stagnation point were neglected and thus the region between the reaction front and the stagnation point was not discussed. However, our numerical result indicates that the new reaction front generates compression waves not only toward the bow shock wave but also toward the stagnation point. The shock stand-off distance is approximately 0.24 × (radius) = $2.4L^*$ in this case. The induction length L^* can be obtained from the experimental result at the C-J velocity where the steady ZND wave structure model holds. The induction zone must be theoretically L^* on the stagnation streamline behind the normal segment of the bow shock. The result says, only about 40% of the shock stand-off distance is the induction zone region. The region between the reaction front and the stagnation point is about 60% of the shock stand-off distance, and may not be negligible in the wave interaction model. Actually Figs. 5.6 show the induction zone whose length is approximately L^*. Our proposed mechanism is based on the whole region between the bow shock and the stagnation point on the stagnation streamline.

All kinds of waves and changes of physical variables are observed in the density history profile. In Fig. 5.6 (a) the trace of the bow shock is noticed as a sudden density increase of an incoming uniform flow and the reaction front is indicated by a sudden density decrease after the bow shock. There are new reaction zones between the original reaction front and the bow shock. Some of them are generated as an isolated area in front of the original reaction surface, connected with the original one and formed as a peninsula. Also many wave interactions between the bow shock wave and the stagnation point are observed. There are two kinds of cyclic mechanisms. Basically the compression waves are generated at the new reaction front. One wave goes backward (to the bow shock) and the other forward (to the projectile body). The former interacts with the bow shock and generates a contact discontinuity. In general, the temperature on one side of a contact discontinuity is higher than that on the other side. The formation is more like a one-dimensional shock-tube problem. The induction length is highly dependent on the temperature determining the induction time (see equation (2.1)). The higher temperature fluid has the shorter induction time since the fluid velocity across the contact discontinuity is basically the same speed. On the other hand, the latter wave propagates toward the projectile body and reflects on the stagnation point. The reflected wave eventually hits the bow shock and generates a contact discontinuity like the former. These two cyclic motions are basically repeated but do not have an exact periodicity.

- *Occurrence and Extinguishment of New Reaction Front*

The strength of the compression waves has an important role to determine the position and the strength of a new reaction front. The strength depends on the strength of the explosive reaction. The mass production rate, $\rho\omega_\beta$, is useful as a parameter to measure the strength of the reaction and to know where the exothermic reaction progresses. Suppose the mass production per unit time is high, a strong energy release occurs and compression waves are generated. Figure 5.7 (a) shows the history plot of the mass production rate on the stagnation streamline for the same result of Fig. 5.6. Figure 5.7 (b) is the schematic representation of the Fig. 5.7 (a) in order to specify the progress along the reaction front. The exothermic reaction progressing region can be recognized in Fig. 5.7 (a). The reaction hardly progresses behind the reaction front, which means that the condition reaches chemical equilibrium. Also there is a notable difference between the original reaction front (1) and the region (2, 3) in which the compression waves are generated.

The extinguishment of the reaction front is observed in Figs. 5.6 and 5.7, where it is specified as (4) in Fig. 5.7 (b). As seen in Fig. 5.7 (a), reaction progress is observed at (4) but it is not very strong so that new waves are not generated there.

- *Cycle of Oscillation*

As observed in Figs. 5.2 (a) and 5.3 (a), the frequency relative to the projectile radius in the case of $7.5L^*$ is higher than that in case of $10L^*$ even though the induction length of $7.5L^*$ projectile is longer. If the flow variables behind the bow shock are assumed to be the same, the $10L^*$ case should have a higher frequency than $7.5L^*$ case. However, as shown in the density history on the stagnation streamline of $7.5L^*$ in Fig. 5.8, there are two cycles creating the wave interaction so that the frequency of $7.5L^*$ is two times higher than the result of the one cycle case.

V. 5 Enhanced Model Based on Present Simulations

Figure 5.9 is the x-t diagram of an enhanced model proposed here based on our calculations. It shows the whole region between the stagnation point and the bow shock on the stagnation streamline. In this proposed diagram, compression waves generated at a new reaction region have an important role to sustain the oscillatory mechanism. One of the generated compression waves goes to the bow shock and the other to the stagnation point on the body surface, finally resulting in a contact discontinuity for the wave interaction with the bow shock wave. The new reaction fronts are formed as a peninsula in the induction reaction region or an additional region of the original reaction front, as seen in Fig. 5.9.

Although this cyclic mechanism is generated by compression waves created at the new reaction region, the compression waves are not always effective to make the new reaction, depending on the strength of the compression wave. The basic pattern of the cyclic mechanism repeats itself in Fig. 5.9, but the features are not exactly the same in detail.

V. 6 Summary

The basic characteristics of shock-induced combustion around an axisymmetric blunt body have been qualitatively clarified by the numerical simulations. The cyclic mechanism for the generation of periodic unsteadiness is caused by the wave interactions between the stagnation point and the bow shock wave on the stagnation streamline and the enhanced model to explain the mechanism for the periodic unsteadiness was proposed. The periodic unsteadiness in the shock-induced combustion obtained is numerically reproduced even though the gas mixture is different from H_2 / Air, so that the cyclic mechanism is considered as universal.

CHAPTER VI

PARAMETRIC STUDIES FOR VARIOUS PROJECTILE VELOCITIES

A computational study on the mechanisms of the periodic unsteadiness for projectiles in detonable gas mixtures was reported in Chapter V. The enhanced model of mechanism of the periodic unsteadiness is newly proposed by the x-t diagram of the wave interactions. In Chapter VI, the projectile velocity is parametrically changed for further understanding of the mechanism of the periodic unsteadiness, since the Lehr's experimental results shows various flow features when the projectile velocity is changed. A fine grid distribution such as 301×301 is used, because the complicated wave interactions among the low-amplitude weak wave in front of the projectile is important and should be resolved.

VI. 1 Numerical Study on Effect of Projectile Speed

According to the Lehr's experiments, a high frequency oscillation occurs at the projectile velocity around the detonation velocity (D). A lower frequency is observed at a lower projectile velocity. This indicates that the frequency depends on the projectile velocity. The dependency of the peojectile speed is investigated and the key parameter for the frequency of the oscillations is conducted in this study.

- 82% of D

The exothermic reaction does not occur after the bow shock in the case of 82% of detonation velocity. It means that the temperature compressed by the bow shock is not high enough to induce the exothermic reaction in this case. Therefore, the flow features does not change from the non-reacting flow.

- 90% of D in Figs. 6. 1

The corrugated reaction boundary with the low frequency and amplitude is observed at a velocity 10% below the detonation velocity shown in Figs. 6.1. The flow features relative to the projectile scale is similar to the experimental result in Fig. 4.1; the contact discontinuities emanating from the corrugated reaction fronts and compression waves reflecting from the bow shock wave. The schematic picture of the flowfields behind the bow shock is shown in Fig. 6.1 (c). However, the projectile scale is not the same as the experimental one, so that the frequency of the oscillations is different.

- 100% of D in Figs. 6.2

The projectile body flies at the detonation velocity. A corrugated reaction front is clearly observed with the constant interval along the reaction boundary. The phenomenon is nearly periodic with the two families of waves, compression waves and contact discontinuities, in the region between the bow shock wave and the reaction boundary. In the pressure contour plots of Fig. 6.2 (b), the spherical compression wave in front of the projectile body is observed and goes forward and backward on the stagnation streamline. The compression wave reflected at the projectile body is also observed. The schematic picture of the pressure contour plots is seen in Fig. 6.2 (c).

- 110% of D in Figs. 6.3

Figure 6.3 is the case for 110% of detonation velocity. Here, the constant and high frequency appears on the reaction boundary as well as Figs. 4.2 and 4.3. Again, two families of waves (contact discontinuity and compression waves) can be seen. Contact discontinuities are especially clear in the density contour plots in Fig. 6.3 (a). Most of the main flow features drawn in Fig. 4.6 are captured in the computation. Only one missing feature in the density contour plots when compared with Figs. 6.2 and 6.3 is the "striation" which is vertical line between the body surface and the corrugated reaction front. As mentioned in the explanation of Fig. 4.8, it would appear when three-dimensional image is created based on the simulation result. The corrugated pattern surprisingly resembles the experimental result although the computational condition is not the same as the experiment. Since the flow feature is governed by the wave interaction at the stagnation streamline, similar flow pattern could be obtained for different mixture of gases. The basic mechanism of the peirodic unsteadiness in shock-induced combustion is an universal phenomenon based on the wave interaction mechanism.

The pressure contour plots of the 110% case is additionally shown in Fig. 6.3 (b) to clarify the behavior of the spherical pressure wave created at the reaction front in front of the projectile. Since the pressure contour plots do not show the contact discontinuity and the reaction front, they simply represent forward and backward waves. The schematic picture of the pressure contour plots is drawn in Fig. 6.3 (c).

- 120% of D in Fig. 6.4

The flow features in both the denstiy and the pressure contour plots drastically changed. The periodic unsteadiness disappeared on the reaction boundary and the reaction boundary becomes nearly smooth, as seen in Fig. 6.4 (a). The spherical compression wave and their interactions in front of the projectile body disappear in the pressure contour plots in Fig. 6.4 (b).

- 140% of *D* in Fig. 6.5

The smooth reaction boundary is obtained in the density contour plots of 40% above the detonation velocity as is shown in Fig. 6.5 (a). As seen in Fig. 4.5, the higher projectile velocity case does not shows any instabilities in the flowfield. Here again, the computational result shows the same tendency as in the experimental results.

VI. 2 X-t Diagram of Stagnation Streamline

For understanding of the transition of the frequency by changing the projectile velocity, the history (x-t diagram) of the density and pressure distribution between the body surface and the bow shock wave on the stagnation streamline is plotted as follows; (a) level plots at each time and (b) contour plots of history profile.

Before discussing the histories of the flow variable, the characteristics of the induction length are reported. The induction length, which is the distance between the bow shock wave and the reaction front, corresponds to the induction time. The induction time depends on the temperature behind the bow shock (see equation (2.1)). At the lower projectile velocity, the temperature increase is smaller than the higher case, so that the induction length is longer. See the case of 82% of *D*, the exothermic reaction does not occur behind the bow shock because the temperature behind the bow shock is lower than the ignition temperature.

- 90% of *D* in Figs. 6.6 and 6.7

Figures 6.6 and 6.7 are the history of the density and the pressure distributions in the case of 90% of *D*, respectively. The mechanism of the periodic unsteadiness is the same as the enhanced model in Fig. 5.9. The new reaction region generates the compression waves forward to the body surface and backward to the bow shock. The reflected compression wave also makes a contact discontinuity by the interaction with the bow shock. However, the reflected compression wave is weak so that the backward compression wave only contributes the cyclic mechanism. Then, the constant frequency of the oscillations is observed. The interval period of oscillation is about 20.0 (μsec) in this case.

- 100% of D in Figs. 6.8 and 6.9

Figures 6.8 and 6.9 show the density and pressure history, respectively. The periodic unsteadiness is observed in the density history in Fig. 6.8. The regular compression wave interaction is also observed in the pressure history in Fig. 6.9. The frequency is mainly determined by the cycle of the backward compression wave. The interval period of each pulsation is about 6.9 (μsec) in this case.

- 110% of D in Figs. 6.10 and 6.11

The periodic and high frequency oscillation on the stagnation streamline is observed in Figures 6.10 and 6.11. The frequency is determined by the cycle of the backward compression wave, and the reflected compression wave goes through the new reaction region after two cycles. The induction length is shorter, and the frequency is higher than the above cases. The interval period of oscillation is about 3.7 (μsec).

In Figs. 6.6 - 6.11, the same type of wave interaction proposed in Fig. 5.9 is observed. The slowest projectile velocity has the lowest frequency, and the frequency becomes higher gradually with an increase of the projectile velocity. As the projectile velocity becomes faster, the compressed temperature behind the bow shock becomes higher. Therefore, the induction length becomes shorter and shorter as the projectiel velocity is increased. It would be a main reason for the various frequencies.

- 120% of *D* in Figs. 6.12 and 6.13

As observed in Fig. 6.4, the flow feature in the axisymmetric plane changed drastically. The mechanism of the wave interaction is also changed from that of the cases above. The reason for the drastic change is that the induction length is too short to repeat the cyclic wave interaction consisting of the backward compression waves, because the frequecy is mainly determined by the wave interactin of the backward compression wave in the cases above. However, the cyclic wave interaction is slightly observed in the Figs. 6.12 and 6.13. However, the mechanism of the periodic unsteadiness in Fig. 5.9 is not applicable in this wave interaction.

- 140% of *D* in Figs. 6.14 and 6.15

In Figs. 6.14 and 6.15, the wave interaction between the bow shock and the reaction front is not observed because of short inuction length. As observed in Figs. 6.5, the bow shock and the reaction front are almost coupled in front of the projectile body so that the assumption of the logitudial wave interaction on the stagnation streamline is not appropriate for explaining the mechanism in Fig. 6.14 and 6.15.

VI. 3 Summary

Hypersonic reacting flows over an axisymmetric blunt body traveling at various speeds have been computationally simulated. A series of simulations revealed dependency of the mechanism of periodic unsteadiness on the projectile velocity. The enhanced mechanism in Fig. 5.9 is basically adequate to explain the periodic or nearly periodic unsteadiness. The periodic unsteadiness appears in the flowfield when the projectile velocity is around the detonation velocity and the projectile diameter is $10L^*$. In this condition, the reaction mainly progresses near the stagnation streamline and thus the flow feature can be discussed based on the x-t diagram on stagnation streamline. The frequency of the oscillation becomes higher as the projectile velocity is increased mainly because the induciton length becomes shorter.

As mentioned earlier, the basic mechanism of the periodic unsteadiness is believed to be universal, and thus the proposed mechanism can explain Lehr's experiment. However, the quantitative discussion compared with the experimental results would be required to validate the wave interaction model in Fig. 5.9.

CHAPTER VII

FLOW FEATURES OF SHOCK-INDUCED COMBUSTION BASED ON REALISTIC H_2-O_2 REACTION MECHANISM

The generation mechanism of the periodic unsteadiness was numerically investigated using the simplified two-step chemical reaction mechanism for the gas diluted by argon in Chapter V and VI. Based on the computed result, the enhanced model in Fig. 5.9 for the mechanism of the periodic unsteadiness was proposed in Chapter V. This model includes the whole region between the stagnation point and the bow shock on the stagnation streamline, and the model extended the mechanism proposed by McVey and Toong (1971) in Fig. 4.7. It should be noted that the enhanced model was proposed based on the numerical simulations in a difference gas mixture. To confirm that the periodic unsteadiness observed in the tow-step reaction mechanism for the different gas mixture is the same phenomena. As the Lehr's experiments, the same gas mixture as the Lehr's experiment is used for the further analysis in this chapter. Use of the same gas mixture[1] also allow the quantitative discussion. In addition, the discussion on the key parameters supporting the periodic unsteadiness is presented.

VII. 1 Recent Works

Wilson and Sussman (1993) has investigated the shock-induced combustion with the periodic unsteadiness by the numerical simulation. He reproduced the flow pattern observed in Lehr's experiments using the same gas mixture under the same flow conditions as the experiment. He used the Euler equations with the logarithmic form of the species conservation equations as the governing equations.

---

[1] Recently, numerical studies for the periodic unsteadiness are seen in Singh et al. (1992), Ahuja et al. (1992), Ahuja and Tiwari (1993), Willson and Sussman (1993) and Sussman (1993)

The mechanism of the unsteadiness on the stagnation streamline simulated by his work also shows the similar wave interaction as that in Fig. 5.9. However, the frequency of the periodic unsteadiness for the projectile speed of 1,931 m/sec was reported to vary from 530 to 820 KHz. He has concluded that the uncertainties in the rate constants for the reaction mechanism could explain the differences of the frequency between the experiment and the computation because two kinds of the reaction rate constant were used for the simulation. His work has indicated that the effect of the characteristics of the selected rate constants is not negligible for the computation of such supersonic combustion flowfield.

The mechanism of the periodic unsteadiness in shock-induced combustion observed in the experiments is becoming clear by these recent works. However, it has not been found what are the key parameters to trigger the instability and to determine the frequency of the periodic unsteadiness. To discuss the mechanism quantitatively and find out the key parameters, Lehr's experiments are simulated. The time-evolving data of the temperature profiles under Lehr's experimental condition are calculated by the zero dimensional time-integration of the species equations to clarify the characteristics. Finally, the effect of the ratio of the chemical scale with respect to the projectile body scale is examined by changing the projectile body size.

VII. 2 Simulations of Lehr's Experiments

A flow condition for the first computation was selected to be the same as Lehr's experimental conditions. The pressure and the temperature in the gas mixture are set to be 0.421 atm and 292 K. Both 1,931 m/sec (in Fig. 4.2) and 1,685 m/sec (in Fig. 4.1) projectile speeds are simulated using the Euler equations with the species conservation equations under the axisymmetric assumption. A fine grid distribution, especially normal to the body surface, such as 161×321 is used in the present study, since the low amplitude and weak waves in front of the projectile is important.

- *The Projectile Velocity 1,931 m/sec (case of Fig. 4.2)*

Figure 7.1 shows the instantaneous density contour plots under the same conditions as the experiment in Fig. 4.2. Periodic unsteadiness along the reaction boundary is observed. The interaction of compression waves in front of the projectile body is clearly observed in the instantaneous pressure contour plots in Fig. 7.2. At this time instance, the compression waves created by the new reaction which has just occurred around the stagnation streamline move both toward the bow shock and the projectile body. Strong energy is released at the reaction boundary in front of the projectile body. However, no compression waves are observed in the downstream of the flowfield, which suggests that there is no reaction progressing region. In order to confirm the reaction progressing region, the source term of the water, is plotted in Fig. 7.3. Reaction mainly progresses along the reaction boundary, and especially the strong reaction progresses in front of the projectile. The reaction progressing region is considered to create the compression waves and would be the trigger for the periodic unsteadiness.

Figure 7.4 (a) is the history of the density distribution on the stagnation streamline. The wave interaction occurs not only between the bow shock and the reaction front but also between the reaction front and the projectile surface. The creation of the corrugated reaction peninsula is dominated by the wave interaction between the bow shock and the reaction front although the compression wave reflected on the projectile surface contributes to strengthen the compression wave released at the reaction front. Figure 7.4 (b) is the history of the pressure distribution on the stagnation streamline, where only the compression waves are clearly observed. The new reaction zone in Fig. 7.4 (a) obviously creates the compression waves both upstream and downstream, and the compression waves toward the projectile body is reflected at the body surface. The phenomena observed in Figs. 7.4 are exactly periodic.

According to the experimental result obtained by Lehr (1972), the frequency is 712 KHz. One cycle of the periodic unsteadiness is 1.38 μsec in Figs. 7.4, so the frequency is 725 KHz. The frequency of the periodic unsteadiness agrees well with the experimental observation. However, Wilson and Sussman (1993) have reported that the interaction of the reflected waves makes the flow not to be exactly periodic. A nearly periodic unsteadiness was reported and the frequency in their result was approximately 820 KHz. The present simulation uses the same reaction model and rate constants although the nitrogen reactions were omitted from their model. There are several differences in the numerical aspects between the present simulation and their work where the logarithmic transformation of the species conservation equations are adopted for the point-implicit integration. However, the numerical aspects should not cause the difference under the same reaction mechanism. After the discussion about this problem with Wilson and Sussman, they continued running the program code, and eventually the pattern of oscillations became much regular like our computation. The frequency became about 725 KHz, as we reported in the present simulations. They simply did not run th ecode long enough in their original report. According to the experiment in Fig. 4.2, the clear periodic striations in the reaction region are observed, so the physics in the experiment may be accurately simulated in the current computation.

To exactly compare it with the experimental output of the shadowgraph image, the post processor by Tamura and Fujii (1990) which simulates the three-dimensional shadowgraph system is used and an output similar to the experiment from the computational result is generated. The result is shown in Fig. 7.5. All the main features can be seen in this picture including the striations that can not be observed in the two-dimensional plots in Fig. 7.1.

- *The Projectile Velocity 1,685 m / sec (case of Fig. 4.1)*

As seen in Fig. 4.1, the small amplitude oscillations with the constant and low frequency along the reaction boundary are extremely weak. Figure 7.6 is the density contour plots of the simulated result under the experimental condition in Fig. 4.1 at the same speed. The calculated result in Fig. 7.6 also shows the weak wave interaction in front of the projectile body and the extremely small corrugated pattern is observed on the reaction boundary. To make the phenomenon clear, the density gradient are plotted in Fig. 7.7. Contact discontinuities and compression waves between the bow shock and reaction boundary are clearly observed just like the experimental output in Fig. 4.1.

Figures 7.8 (a) and (b) show the history of the density and the pressure distribution on the stagnation streamline. The density distribution shows the bow shock, the reaction front, the compression wave and the contact discontinuity as are shown in Fig. 7.4 (a). The wave interaction in Fig. 7.8 (a) can also be explained by the mechanism in Fig. 5.9 although reaction occurs much closer to the body in this case. The compression waves released at the new reaction region propagate to the upstream and downstream, and the compression waves interact with the bow shock and make the contact discontinuity. Basically two contact discontinuities are generated after the interaction. However, these contact discontinuities are closely and parallelly located and make one new reaction peninsula. One cycle of the periodic unsteadiness corresponds to 6.256 μsec in this calculation and the frequency is 159.8 KHz. The experimental result says that the frequency is 150 KHz, and the agreement is quite good also in this case.

• *Discussion*

From the plots of the numerical results in the previous section, the mechanism of periodic unsteadiness in the shock-induced combustion of Lehr's experiments was much better understood. In addition, it suggested that such periodic unsteadiness is universal phenomena in the shock-induced combustions and could occur in any gas mixture under certain conditions because the fluid dynamic wave interaction on the stagnation streamline is the cause for the unsteadiness. The periodic unsteadiness observed for the different gas mixture in Chapter V is now considered to be the same type of phenomenon as Lehr's experiment.

So far, the key parameters for the periodic unsteadiness are the followings:

1. *induction time (ignition delay time) on the stagnation streamline and the corresponding induction length, which determines frequency.*
2. *compression wave reflected on projectile surface, which may smear periodicity.*
3. *relative scale of the induction length and the shock stand-off distance, which determines the wave interaction pattern.*

However, the effect of the characteristics of the chemical kinetics of gas-phase hydrogen-air combustion has not been discussed. The reaction profiles using the time-evolving temperature profile will be discussed in the next section.

VII. 3 Characteristics of Chemical Kinetics

The time-integration of species equations in zero dimension in space under a *constant volume mode* is carried out in order to clarify the characteristics of the reaction profile in Table 4.1. We assume that all the flow variables are given at the conditions after the bow shock on the stagnation streamline and the flow speed corresponds to the projectile speed. The integration procedure is the following;

1. *flow variables after the normal shock wave are given as a initial condition by the Rankin-Hugoniot relation of the real gas.*
2. *all the species equations are time-integrated. During the reaction progress, no total density change is allowed under the constant volume mode.*

For the calculation of species-specific heat, the thermodynamics data and their curve fit coefficients developed at the NASA Thermochemical Polynomials (see Appendix A) are used. This procedure provides an accurate data for the characteristics of a non-equilibrium reaction under the *constant volume mode*. If the fluid velocity after the bow shock wave on the stagnation streamline is constant (without gradual isentropic compressions toward the body surface), the induction reaction length is given. So, the relation between the shock stand-off distance and the induction length is roughly estimated.

Two projectile speeds of 1,685 and 1,931 m/sec, which were simulated in this chapter, are tested. The conditions of the gas mixture are selected to fit the Lehr's experiments. Since the exothermic reaction occurs after the ignition delay and causes a sudden temperature increase, the time-evolving temperature profiles are plotted in Fig. 7.9. The time period required for the temperature increase due to the exothermic reaction, called the *reaction time*, is almost the same for both cases. However, the induction times are 1.0 μsec for 1,931 m/sec and 8.8 μsec for 1,685 m/sec and significant difference exists. The flow velocities after the bow shock by the Rankin-Hugoniot relation are 361.26 m/sec for the projectile speed 1,931 m/sec and 340.35 m/sec for the projectile speed 1,685 m/sec. The induction length is roughly calculated by (the flow velocity) × (the induction time). They are 0.36126 mm and 2.995 mm, respectively. The induction times and lengths in the real simulations can be measured in the manner shown in Fig. 5.10. See Fig. 7.4 (a) and 7.8 (a), the induction time and length in the real simulations are 1.0 μsec and 0.36 mm for 1,931 m/sec, and 5.7 μsec and 1.2 mm for 1,685 m/sec. The induction time and length of the projectile speed 1,931 m/sec in Fig. 7.4 (a) exactly agree with those in the reaction profile in Fig. 7.9. As the induction length in Fig. 7.4 (a) is only 1/6 of the shock stand-off distance and contact discontinuities, which indicate the particle path line, are straight, the effect of the isentropic compression can be neglected.

On the other hand, the induction time and length of the projectile speed 1,685 m/sec in Fig. 7.8 (a) do not agree with the reaction profile in Fig. 7.9. As seen in Fig. 7.8 (a), the contact discontinuitiesare not straight but curved due to the deceleration, isentropic compressions after the bow shock wave has to be considered in this case. The discrepancy may come from the effect of isentropic compression during the induction length that occupies 2/3 of the shock stand-off distance.

The observation above suggested that the induction time is one of the important key parameters that determines the frequency of the periodic unsteadiness. In addition, it was shown that frequency may be predicted from the analysis of the zero-dimensional time-integration of species equations without simulating the flowfield.

VII. 4 Smaller Projectile Cases

In the simulations of the simplified two-step reaction mechanism, the periodic unsteadiness was reported when the projectile radius is $10\,L^*$. (The L^* is the induction length of the plane C-J detonation.) However, when the smaller projectile radius ($5\,L^*$) was used for the simulation, the unsteadiness disappeared from the flowfield. The absence of the unsteadiness has not been clarified. The study to identify why the unsteadiness disappeared may reveal another key parameters for the unsteadiness. Therefore, the case for the smaller projectile body is simulated using hydrogen/air gas mixture under the same condition of the projectile speed 1,931 m/sec for the quantitative discussion. The projectile diameter is selected to be 2.5 mm.

- *Projectile Diameter 2.5 mm*

Figure 7.11 is the density contour plots in the case of projectile diameter 2.5 mm and the speed 1,931 m/sec. The relative length of the shock stand-off distance to the region of the burned gas on the stagnation streamline is almost the same as that in the case of projectile speed 1,685 m/sec in Fig. 7.6. However, no wave interaction on the stagnation streamline is observed in this case. Figure 7.12 is the pressure contour plots, which only show the smooth contour lines in the whole flowfield even in front of the projectile. The steady solution is obtained in this simulation.

- *Another Key Parameters for the Periodic Unsteadiness*

The location of the reaction boundary in Fig. 7.11 is almost the same as that in Fig. 7.6, but one shows the periodic unsteadiness, the other does not show it. It indicates that relative scale of the induction length and the shock stand-off distance is not solely the key parameter for the periodic unsteadiness. What is additional important key parameters for the unsteadiness?

Based on the previous discussion about Fig. 7.9, the induction time determines the frequency of the periodic unsteadiness. The reaction times due to the exothermic reaction are almost the same for both cases in Fig. 7.9. Let's compare the two cases of the diamtr 15.0 mm and 2.5 mm at the speed 1,931 m/sec. The projectile speeds are the same and therefore the physical induction lengths are the same. The reaction times are also the same. The difference is a relative scale of the induction length and the shock stand-off distance.

To help understanding the complicated comparisons, the schematic picture showing the difference is proposed in Fig. 7.13. The relation between the reaction period and the shock stand-off distance is shown for the three cases. Let's pay attention to the reaction period relative to the shock stand-off distance. It corresponds to the relative concentration of the energy release by the exothermic reaction. Reaction period relative to the shock stand-off distance is much larger in the case 3 compared to cases 1 and 2. Thus, in the case 3, when physical (or fluid dynamic) length scale is small, reaction period is relatively large and temperature increase rather gradually within that small physical scale. Therefore, compression waves are created gradually rather than abruptly. This is the reason for the disappearance of unsteadiness.

The key parameters are the followings;

1. *induction time (ignition delay time), which determines the frequency of the periodic unsteadiness.*
2. *heat release, which is considered the temperature rise in the reaction profile. In the simulations of the flowfield, the location of the bow shock wave, which is caused by the change of the reaction*

region, is changed by the heat release, then the path of the reflected compression waves is changed.

3. *concentration of heat release, which is given by the ratio of the reaction period with respect to the shock stand-off distance, is an important parameter for unsteadiness. It also change the location of the bow shock.*

VII. 5 Summary

A series of the simulations clarified the key parameters of the periodic unsteadiness around the projectile travelling at hypervelocity. They are considered to be the induction time, heat release and concentration of the heat release. Induction time is a key parameter for the frequency of unsteadiness. The concentration of heat release is important for the unsteadiness itself. Amount of heat release is important because the total energy creating the compression waves depends on it. Simple zero-dimensional analysis is useful because all these features can be recognized in such an analysis.

CHAPTER VIII

CONCLUSIONS

The characteristics of the standing oblique detonation (SOD) around a two-dimensional blunted wedge and an axisymmetric blunt body have been investigated by the numerical simulations to clarify the relations between thermodynamic, chemical kinetics and fluid mechanical considerations because the underlying physics of the SOD has not been fully investigated.

Three different modes in the SOD supported by the two-dimensional wedge are obtained by changing the wedge tip radius and the angle of half wedge; the steady oblique coupled detonations, the steady oblique decoupled detonation and run-away detonations which are unable to stand in front of a wedge. Whether a coupled oblique detonation is obtained or not significantly depends on the scale of the wedge tip radius. The mode change can be explained by the limiting angle of the oblique shock wave. The present study confirms that there are critical values for the incident Mach number, the wedge tip radius and the wedge angle for the establishment of the SOD in a hypersonic premixed gas.

The ballistic range experiments for the combustible gas at hypervelocities have been numerically simulated for the study of the SOD supported by the axisymmetric blunt body. A series of the simulations have clarified the detailed mechanism of the periodic unsteadiness observed in the experiments. First, using the simplified chemical reaction mechanism, the basic characteristics of the periodic unsteadiness in the shock-induced combustion around an axisymmetric blunt body have been qualitatively studied, and the enhanced model to explain the mechanism for the periodic unsteadiness has been proposed. The dependency of the mechanism on the projectile velocity has also been investigated, and the enhanced model is considered to be basically appropriate to explain the periodic unsteadiness in the various projectile velocities. Though the gas mixture is different from the experimental conditions, the periodic unsteadiness in the shock-induced combustion was reproduced in the computed results. It indicated that the detailed mechanism of the periodic unsteadiness is mainly dominated by the fluid dynamics coupled with the energy release by the exothermic reactions, and therefore the phenomenon is universal for any gas mixtures.

Secondly, the key parameters for the periodic unsteadiness have been quantitatively studied by the parametric study using the H_2/Air gas mixture. They are considered to be the induction time, heat release and concentration of the heat release. The induction time is a key parameter to determine the frequency of the unsteadiness. Concentration of the heat release is important for the unsteadiness itself. Amount of the heat release is important because the total energy creating the compression waves depend on it.

In this dissertation, the numerical simulations revealed the underlaying physics of the flowfields of the shock-induced combustion. Recent computational fluid dynamics techniques give us a new experimental apparatus (numerical wind tunnel/ballistic range), which provides the complete time evolving data of the entire flowfields that would never be available in the physical experiments.

BIBLIOGRAPHY

Abouseif, G.E. and Toong, T.Y., (1981), "Nonlinear Wave-Kinetic Interactions in Irreversibly Reacting Media," Journal of Fluid Mechanism, 103, pp. 1-22.

Abouseif, G.E. and Toong, T.Y., (1982), "Theory of Unstable One-Dimensional Detonations," Combustion and Flame, 45, pp. 67-94.

Ahuja, J.K., Tiwari, S.N. and Singh, D.J., (1992), "Investigation of Hypersonic Shock-Induced Combustion in a Hydrogen-Air System," AIAA Paper 92-0339.

Ahuja, J.K. and Tiwari, S.N., (1993), "Numerical Simulation of Shock-Induced Combustion in a Superdetonative Hydrogen-Air System," AIAA Paper 93-0242.

Alpert, R.L. and Toong, T.Y., (1972), "Periodicity in Exothermic Hypersonic Flow around Blunt Projectiles," Astronautica Acta, 17, pp. 539-560.

Behrens, H., Struth, W. and Wecken, F., (1965), "Studies of Hypervelocity Firings into mixtures of Hydrogen With Air or With Oxygen," Tenth Symposium (Internatilnal) on Combustion, pp. 245-252.

Bukiet, B., (1989), "The Effect of Curvature on Detonation Speed," SIAM Journal on Applied Mathematics, 49, (5), pp. 1433-1446.

Chernyi, G.G. and Gilinskii, S.M., (1970), "High Velocity Motion of Solid Bodies in Combustible Gas Mixtures," Astronautica Acta, 15, pp. 539-545.

Drummond, J.P. and Weidner, E.H., (1981), "Numerical Study of a Scramjet Engine Flow Field," AIAA Paper 81-0186.

Fickett, W. and Wood, W.W., (1966), "Flow Calculations for Pulsating One-Dimensional Detonations," Physics of Fluids, 9, (5), pp. 903-916.

Fujiwara, T. and Matsuo, A., (1990), "Oxyhydrogen Oblique Detonation Supported by Two-Dimensional Wedge," Nagoya University Memoirs of the Faculty of Engineering Vol. 41, No. 2.

Goyal, G., Maas, U. and Warnatz, J., (1990), "Simulation of the Transition from Deflagration to Detonation," SAE Technical Paper Series 900026.

Hertzberg, A., Bruckner, A.P., and Bagdanoff, D.W., (1988), "Ram Accelerator: A New Chemical Method for Accelerating Projectiles to Ultrahigh Velocities," AIAA Journal, 26, pp. 195-203.

Jachimowski, C.J., (1988), "An Analytical Study of the Hydrogen-Air Reaction Mechanism With Application to Scramjet Combustion," NASA TP 2791.

Korobeinikov, V.P., Levin, V.A., Markov, V.V. and Chernyi, G.G., (1972), "Propagation of Blast Waves in a Combustible Gas," Astronautica Acta, 17, pp. 529-537.

Lee, J.H.S., (1972), "Gasdynamics of Detonations," Astronautica Acta, 17, pp. 455-466.

Lee, J.H.S., Initiation of Gaseous Detonation, in Ann. Rev. Phys. Chem. : 75-104, Annual Reviews Inc. (1977).

Lee, S.H. and Deiwert, G.S., (1989), "Calculation of Nonequilibrium Hydrogen-Air Reactions with Implicit Flux Vector Splitting Method," AIAA Paper 89-1700.

Lee, S.H. and Deiwert, G.S., (1990), "Flux-Vector Splitting Calculation of Nonequilibrium Hydrogen-Air Reactions," Journal of Spacecraft and Rockets, 27, (2), pp. 167-174.

Lehr, (1972), "Experiments on Shock-Induced Combustion," Astronautica Acta, 17, pp. 589-597.

Majda, A. and Rosales, R., (1983), "A Theory for Spontaneous Mach Stem Formation in Reacting Shock Fronts, I. The Basic Perturbation Analysis," SIAM Journal on Applied Mathematics, 43, (6), pp. 13101334.

Matsuo, A. and Fujiwara, T., (1991), "Numerical Simulation of Shock-Induced Combustion Around an Axisymmetric Blunt Body," AIAA Paper 91-1414.

Matsuo, A., Fujiwara, T. and Fujii, K., (1993), "Flow Features of Shock-Induced Combustion around Projectile Travelling at Hypervelocities," AIAA Paper 93-0451.

McVey, J.B. and Toong, T.Y., (1971), "Mechanism of Instabilities of Exothermic Hypersonic Blunt-Body Flow," Combustion Science and Technilogy, 3, pp. 63-76.

Pratt, D.T., Humphrey, J.W. and Glenn, D.E., (1987), "Morphology of a Standing Oblique Detonation Wave," AIAA Paper 87-1785.

Rabie, R.L., Fowles, G.R. and Fickett, W., (1979), "The Polymorphic Detonation," Phisics of Fluids, 22, (6), pp. 422-435.

Reddy, K.V. and Fujiwara, T., (1988), "Role of Transverse Waves in a Detonation Wave - a Study Based on Propagation in a Porous Wall Chamber," Nagoya University Memoirs of the Faculty of Engineering 40.

Ruegg, F.W. and Dorsey, W., (1962), "A Missile Technique for the Study of Detonation

Wave," J. Res. Natl. Bur. Std, 66C, pp. 51-58.

Ruegg, F.W. and Dorsey, W.W., (1963), "General Discussion," Nineth Symposium (International) on Combustion, pp. 474-481.

Singh, D.J., Ahuja, J.K. and Carpenter, M.H., (1992), "Numerical Simulation of Shock-Induced Combustion /Detonation," Computing Systems in Engineering, 3, (14), pp. 201-215.

Strehlow, R.A. and Cohen, A., (1962), "Initiation of Detonation," The Physics of Fluids, 5, (1), pp. 97-101.

Strehlow, R.A., Adamczyk, A.A. and Stiles, R.J., (1972), "Transient Studies of Detonation Waves," Astronautica Acta, 17, pp. 509-527.

Sugimura, T., Fujiwara, T. and Lee, J.H., (1990), "Cellular Detonation - Instability and Sub-Structure," Nagoya University Memoires of the Faculty of Engineering 42.

Sussman, M.A., (1993), "Source Term Evaluation for Combustion Modeling," AIAA Paper 93-0239.

Taki, S. and Fujiwara, T., (1978), "Numerical Analysis of Two-Dimensional Nonsteady Detonation," AIAA Journal, 16, pp. 73-77.

Tamura, Y. and Fujii, K., (1990), "Visualization for Computational Fluid Dynamics and The Comparison With Experiments," AIAA Paper 90-3031.

Urtiew, P.A. and Oppenheim, A.K., (1967), "Detonative Ignition Induced by Shock Merging," Eleventh Symposium (International) on Combustion, pp. 665-670.

Wada, Y., Kubora, H., Ogawa, S. and Ishiguro, T., (1988), "A Diagonalizing Formulation of General Real Gas-Dynamic Matrices With a New Class of TVD Schemes," AIAA Paper 88-3596.

Wada, Y., Ogawa, S., Ishiguro, T. and Kubota, H., (1989), "A Generalized Roe's Approximate Reimann Solver for Chemically Reacting Flows," AIAA Paper 89-0202.

Wang, Y. and Fujiwara, T., (1988), "Three-Dimensional Standing Oblique Detonation Wave," AIAA Paper 88-0478.

Wilson, G.J. and MacCormack, R.W., (1990), "Modeling Supersonic Combustion Using a Fully-Implicit Numerical Method," AIAA Paper 90-2307.

Wilson, G.J. and MacCormack, R.W., (1992), "Modeling Supersonic Combustion Using a Fully-Implicit Numerical Method," AIAA Journal, 30, (4), pp. 1008-1015.

Wilson, G.J. and Sussman, M.A., (1993), "Computation of Unsteady Shock-Induced Combustion Using Logarithmic Species Conservation Equations," AIAA Journal, 31, (2), pp. 294-301.

Yee, H.C., (1987), "Upwind and Symmetric Shock Capturing Schemes," NASA TM 89464.

Yee, H.C. and Shinn, J.L., (1989), "Semi-Implicit and Fully Implicit Shock-Capturing Methods for Nonequilibrium Flows," AIAA Journal, 27, (3), pp. 299-307.

Yungster, S., Eberhardt, S. and Bruckner, A.P., (1991), "Numerical Simulation of Hypervelocity Projectile in Detonable Gases," AIAA Journal, 29, pp. 187-199.

APPENDIX A

MOLECULAR CONSTANTS

This appendix gives the molecular constants and thermochemical data used for the nine species in hydrogen-ari gas model. The source of thermochemical data is NASA polynomicals from Appendix A of Wilson (1991) which have the following form for each species

$$\frac{h^\circ}{RT} = a_1 + a_2\frac{T}{2} + a_3\frac{T^2}{3} + a_4\frac{T^3}{4} + a_5\frac{T^4}{5} + \frac{a_6}{T}$$

$$\frac{s^\circ}{R} = a_1 \, ln T + a_2 T + a_3\frac{T^2}{2} + a_4\frac{T^3}{3} + a_5\frac{T^4}{4} + a_7$$

where the superscript on the enthalpy H° and the entropy S° are for a reference state of one stmosphere. The coefficients for these curve fits are found in Table D.1. There is one set of coefficents for the temperature range 300K to 1000K and the another for the temperature range 1000K to 5000K. The enthalpy H° includes the found in Table D.2.

Molecular Weight of Species (Kg/Kmole)

H_2	O_2	H	O	OH	H_2O	H_2O_2	N_2
2.016	32.000	1.008	16.000	17.008	18.016	34.016	28.016

Table D.1 NASA Thermochemical Polynomials

Temperature Rnage 300K to 1000K							
species	a_1	a_2	a_3	a_4	a_5	a_6	a_7
N_2	.37044177e+01	-.14218753e-02	.28670392e-05	-.12028885e-08	-.13954677e-13	-.10640795e+04	.22336285e+01
O_2	.37837135e+01	-.30233634e-02	.99492751e-05	-.98189101e-08	.33031825e-11	-.10638107e+04	.36416345e+01
H_2	.33553514e+01	.50136144e-03	-.23006908e-06	-.47905324e-09	.48522585e-12	-.10191626e+04	-.35477228e+01
OH	.38737300e+01	-.13393772e-02	.16348351e-05	-.52133639e-09	.41826974e-13	.35802348e+04	.34202406e+00
HO_2	.35964102e+01	.52500748e-03	.75118344e-05	-.95674952e-08	.36597628e-11	-.89333502e+03	.66372671e+01
H_2O	.41677234e+01	-.18114970e-02	.59471288e-05	-.48692021e-08	.15291991e-11	-.30289969e+05	-.73135474e+00
H_2O_2	.33887536e+01	.65692260e-02	-.14850126e-06	-.46258055e-08	.24715147e-11	-.17663147e+05	.67853631e+01
O	.30309401e+01	-.22525853e-02	.39824540e-05	-.32604921e-08	.10152035e-11	.29136526e+05	.26099342e+01
H	.25000000e+01	0.0	0.0	0.0	0.0	.25471627e+05	-.46011762e+00

Temperature Rnage 1000K to 5000K							
species	a_1	a_2	a_3	a_4	a_5	a_6	a_7
N_2	.28532899+01	.16022128e-02	-.62936893e-06	.11441022e-09	-.78057465e-14	-.89008093e+03	.63964897e+01
O_2	.36122139e+01	.74853166e-03	-.19820647e-06	.33749008e-10	-.23907374e-14	-.11978151e+04	.36703307e+01
H_2	.30667095e+01	.57473755e-03	.13938319e-07	-.25483518e-10	.29098574e-14	-.86547412e+03	-.17798424e+01
OH	.28897814e+01	.10005879e-02	-.22048807e-06	.20191288e-10	-.39409831e-15	.38857042e+04	.55566427e+00
HO_2	.40173060e+01	.22175883e-03	-.57710171e-05	.71372882e-10	-.36458591e-14	-.11412445e+04	.37846051e+01
H_2O	.26110472e+01	.31563130e-02	-.92985438e-06	.13331538e-09	-.74689351e-14	-.29868167e+05	.72091268e+01
H_2O_2	.45731667e+01	.43361363e-02	-.14746888e-05	.23489037e-09	-.14316536e-13	-.18006961e+05	.50113696e+00
O	.25342961e+01	-.12478170e-04	-.12562724e-07	.69029862e-11	-.63797095e-15	.29231108e+05	.49628591e+01
H	.25000000e+01	0.0	0.0	0.0	0.0	.25471627e+05	-.46011762e+00

APPENDIX B

CHEMICAL SOURCE TERM FOR THE EQUATIONS OF SPECIES

The general form of each chemical reaction can be written as

$$\sum_{i=1}^{N} \nu''_{ik} A_i \Leftrightarrow \sum_{i=1}^{N} \nu'_{ik} A_i$$

where A represents species and ν'' and ν' are the stoichiometric coefficients of the reactant and products for each chemical reaction k. Then the source terms for the different species equations i can be written

$$\omega_i = W_i \sum_{k=1}^{K} (\nu''_{ik} - \nu'_{ik}) R_k$$

Note that $\sum_{i=1}^{N} \omega_i = 0$ satisfying overall mass conservation. The R_k indicates the rate of progress variable of chemical reaction k and is given as

$$R_k = k_{f,k} \prod_{i=1}^{N} \left(c_{\chi i}\right)^{\nu'_{ik}} - k_{b,k} \prod_{i=1}^{N} \left(c_{\chi i}\right)^{\nu''_{ik}}$$

where $c_{\chi i}$ is mole concentration of species i, and $k_{f,k}$ and $k_{b,k}$ are the forward and backward rate constant of reaction k. The forward rate constants $k_{f,k}$ for each reaction k are given by the extended Arrhenius expression

$$k_{f,k} = A_k T^{n_k} \, exp(-E_k / RT)$$

where T is the temperature and A_k. n_k, and E_k are constants found in reaction mechanism in Table. The backward rate constants $k_{b,k}$ are calculated using the equilibrium constant $K_{eq,k}$ for each reaction and the relation

$$K_{eq,k} = \frac{k_{f,k}}{k_{b,k}}.$$

The equilibrium constant $K_{eq,k}$ is related with the pressure equilibrium constant as

$$K_{eq,k} = K_{Peq,k}\left(\frac{P_{atm}}{RT}\right)^{\sum_{i=1}^{N}(\nu''_{ik}-\nu'_{ik})}$$

where $P_{atm} = 1(atm)$ and R is the universal gas constant. The pressure equilibrium constant $K_{Peq,k}$ are calculated using the enthalpy and the standard state entropy as

$$K_{Peq,k} = exp\left[\sum_{i=1}^{N}\left\{(\nu''_{ik} - \nu'_{ik})\frac{s_i^o}{R_i}\right\} - \sum_{i=1}^{N}\left\{(\nu''_{ik} - \nu'_{ik})\frac{h_i}{R_i T}\right\}\right].$$

If the third-body efficiency is considered in chemical reaction, the rate of progress variable is given as

$$R_k = \left\{\sum_{i=1}^{N}(\alpha_{ik} c_{\chi i})\right\}\left\{k_{f,k}\prod_{i=1}^{N}(c_{\chi i})^{\nu'_{ik}} - k_{b,k}\prod_{i=1}^{N}(c_{\chi i})^{\nu''_{ik}}\right\}$$

The α_{ik} is the third efficiency factor for reaction k and is described in Table 1. The equations of state for pressure is given by the Dalton's law for a mixture of thermally perfect gases,

$$P = \sum_{i=1}^{N}\frac{\rho_i}{W_i}R_u T$$

where R_u is the universal gas constant, W_i is the molecular weight of species i and the sum is over all N species present.

APPENDIX C

AXISYMMETRIC EULER EQUATIONS

The Cartesian coordinated three-dimensional Euler equations in non-dimensional and strong conservation law form are written as

$$\frac{\partial U}{\partial t}+\frac{\partial E}{\partial x}+\frac{\partial F}{\partial y}+\frac{\partial G}{\partial z}=0$$

where

$$U=\begin{pmatrix}\rho\\ \rho u\\ \rho v\\ \rho w\\ E\end{pmatrix},\quad E=\begin{pmatrix}\rho u\\ \rho u^2+P\\ \rho uv\\ \rho uw\\ (E+P)u\end{pmatrix},\quad F=\begin{pmatrix}\rho v\\ \rho uv\\ \rho v^2+P\\ \rho vw\\ (E+P)v\end{pmatrix},\quad G=\begin{pmatrix}\rho w\\ \rho uw\\ \rho vw\\ \rho w^2+P\\ (E+P)w\end{pmatrix}$$

Three original equations are firstly transformed to the cylindrical coordinates (x',r,θ,t') in order to establish the final axisymmetric form. The relationship between the Cartesian and cylindrical coordinates are

$$\begin{aligned}&x=x'\\ &y=r\cos\theta\\ &z=r\sin\theta\\ &t=t'\end{aligned}$$

and partial derivatives in the Cartesian coordinate are also transformed as

$$\begin{aligned}&\frac{\partial}{\partial x}=\frac{\partial}{\partial x'}\\ &\frac{\partial}{\partial y}=\cos\theta\frac{\partial}{\partial r}-\frac{\sin\theta}{r}\frac{\partial}{\partial\theta}\\ &\frac{\partial}{\partial z}=\sin\theta\frac{\partial}{\partial r}+\frac{\cos\theta}{r}\frac{\partial}{\partial\theta}\\ &\frac{\partial}{\partial t}=\frac{\partial}{\partial t'}\end{aligned}$$

As a result, the cylindrical velocity components (u',v',w') are expressed as

$$\begin{aligned} u &= u' \\ v &= v' \cos\theta - w' r \sin\theta \\ w &= v' \sin\theta + w' r \cos\theta \end{aligned}$$

and for example, the partial derivative of v respect with y can be transformed to a slightly complex form as

$$v_y = v'_r \cos^2\theta + \left(2w' - rw'_r - \frac{v'_\theta}{r}\right)\sin\theta\cos\theta + \left(\frac{v'}{r} + w'_\theta\right)\sin^2\theta$$

Once all terms in the original equations are transformed, we can obtain the cylindrical coordinated Euler equations. Under the following assumptions

$$w' = \frac{\partial}{\partial\theta} = 0, \qquad \theta = 0,$$

resulting Euler equations are

$$\frac{\partial Q}{\partial t} + \frac{\partial E}{\partial x} + \frac{\partial F}{\partial r} + H = 0$$

where

$$U = \begin{pmatrix} \rho \\ \rho u \\ \rho v \\ E \end{pmatrix}, \quad E = \begin{pmatrix} \rho u \\ \rho u^2 + P \\ \rho uv \\ (E+P)u \end{pmatrix}, \quad F = \begin{pmatrix} \rho v \\ \rho uv \\ \rho v^2 + P \\ (E+P)v \end{pmatrix}, \quad H = \frac{1}{r}\begin{pmatrix} \rho v \\ \rho uv \\ \rho v^2 \\ (E+P)v \end{pmatrix}$$

The above Cartesian coordinated Euler equations are usually transformed to the general curvilinear coordinates before the computations. The final expressions have been presented in Chapter II.

APPENDIX D

JACOBIAN OF CHEMICAL SOURCE TERM FOR THE EQUATIONS OF SPECIES

The chemical reaction source term vector S that described in Appendix B indetail is described as

$$S=\begin{pmatrix} 0 \\ 0 \\ 0 \\ 0 \\ \omega_i \end{pmatrix}$$

The $\partial\hat{S}/\partial\hat{U}\ (=\partial S/\partial U)$ in equation (2.14) for the equations of species is written in the followings.

$$\frac{\partial\hat{S}}{\partial\hat{U}}=\begin{bmatrix} 0 & 0 & 0 & 0 & 0 & \cdots & 0 & \cdots & 0 \\ 0 & 0 & 0 & 0 & 0 & \cdots & 0 & \cdots & 0 \\ 0 & 0 & 0 & 0 & 0 & \cdots & 0 & \cdots & 0 \\ 0 & 0 & 0 & 0 & 0 & \cdots & 0 & \cdots & 0 \\ \frac{\partial\dot{\omega}_1}{\partial\rho} & \frac{\partial\dot{\omega}_1}{\partial(\rho u)} & \frac{\partial\dot{\omega}_1}{\partial(\rho v)} & \frac{\partial\dot{\omega}_1}{\partial E} & \frac{\partial\dot{\omega}_1}{\partial\rho_1} & \cdots & \frac{\partial\dot{\omega}_1}{\partial\rho_j} & & \frac{\partial\dot{\omega}_1}{\partial\rho_N} \\ \vdots & \vdots & \vdots & \vdots & \vdots & & \vdots & & \vdots \\ \frac{\partial\dot{\omega}_i}{\partial\rho} & \frac{\partial\dot{\omega}_i}{\partial(\rho u)} & \frac{\partial\dot{\omega}_i}{\partial(\rho v)} & \frac{\partial\dot{\omega}_i}{\partial E} & \frac{\partial\dot{\omega}_i}{\partial\rho_1} & \cdots & \frac{\partial\dot{\omega}_i}{\partial\rho_j} & \cdots & \frac{\partial\dot{\omega}_i}{\partial\rho_N} \\ \vdots & \vdots & \vdots & \vdots & \vdots & & \vdots & & \vdots \\ \frac{\partial\dot{\omega}_N}{\partial\rho} & \frac{\partial\dot{\omega}_N}{\partial(\rho u)} & \frac{\partial\dot{\omega}_N}{\partial(\rho v)} & \frac{\partial\dot{\omega}_N}{\partial E} & \frac{\partial\dot{\omega}_N}{\partial\rho_1} & \cdots & \frac{\partial\dot{\omega}_N}{\partial\rho_j} & \cdots & \frac{\partial\dot{\omega}_N}{\partial\rho_N} \end{bmatrix}$$

where the elements of the matrix are given as

$$\frac{\partial\dot{\omega}_i}{\partial\rho}=\frac{\partial T}{\partial\rho}\cdot W_i\sum_{k=1}^{K}\left[\left(\nu''_{ik}-\nu'_{jk}\right)\left\{\sum_{l=1}^{n}\left(\alpha_{lk}c_{\chi l}\right)\right\}\left\{\frac{\partial k_{f,k}}{\partial T}\prod_{l=1}^{N}\left(c_{\chi l}\right)^{\nu'_{ik}}-\frac{\partial k_{b,k}}{\partial T}\prod_{l=1}^{N}\left(c_{\chi l}\right)^{\nu''_{ik}}\right\}\right]$$

$$\frac{\partial\dot{\omega}_i}{\partial(\rho u)}=\frac{\partial T}{\partial(\rho u)}\cdot W_i\sum_{k=1}^{K}\left[\left(\nu''_{ik}-\nu'_{jk}\right)\left\{\sum_{l=1}^{n}\left(\alpha_{lk}c_{\chi l}\right)\right\}\left\{\frac{\partial k_{f,k}}{\partial T}\prod_{l=1}^{N}\left(c_{\chi l}\right)^{\nu'_{ik}}-\frac{\partial k_{b,k}}{\partial T}\prod_{l=1}^{N}\left(c_{\chi l}\right)^{\nu''_{ik}}\right\}\right]$$

$$\frac{\partial\dot{\omega}_i}{\partial(\rho v)}=\frac{\partial T}{\partial(\rho v)}\cdot W_i\sum_{k=1}^{K}\left[\left(\nu''_{ik}-\nu'_{jk}\right)\left\{\sum_{l=1}^{n}\left(\alpha_{lk}c_{\chi l}\right)\right\}\left\{\frac{\partial k_{f,k}}{\partial T}\prod_{l=1}^{N}\left(c_{\chi l}\right)^{\nu'_{ik}}-\frac{\partial k_{b,k}}{\partial T}\prod_{l=1}^{N}\left(c_{\chi l}\right)^{\nu''_{ik}}\right\}\right]$$

$$\frac{\partial\dot{\omega}_i}{\partial E}=\frac{\partial T}{\partial E}\cdot W_i\sum_{k=1}^{K}\left[\left(\nu''_{ik}-\nu'_{jk}\right)\left\{\sum_{l=1}^{n}\left(\alpha_{lk}c_{\chi l}\right)\right\}\left\{\frac{\partial k_{f,k}}{\partial T}\prod_{l=1}^{N}\left(c_{\chi l}\right)^{\nu'_{ik}}-\frac{\partial k_{b,k}}{\partial T}\prod_{l=1}^{N}\left(c_{\chi l}\right)^{\nu''_{ik}}\right\}\right]$$

$$\frac{\partial \dot{\omega}_i}{\partial \rho_j} = W_i \sum_{k=1}^{K}\left[\left(\nu''_{ik} - \nu'_{jk}\right)\left(\frac{\alpha_{jk}}{W_j}\right)\left\{k_{f,k}\prod_{l=1}^{N}\left(c_{\chi l}\right)^{\nu'_{lk}} - k_{b,k}\prod_{l=1}^{N}\left(c_{\chi l}\right)^{\nu''_{lk}}\right\}\right]$$

$$+W_i \sum_{k=1}^{K}\left[\left(\nu''_{ik} - \nu'_{jk}\right)\left\{\sum_{l=1}^{n}\left(\alpha_{lk} c_{\chi l}\right)\right\}\left\{k_{f,k}\frac{\nu'_{jk}}{\rho_j}\prod_{l=1}^{N}\left(c_{\chi l}\right)^{\nu'_{lk}} - k_{b,k}\frac{\nu''_{jk}}{\rho_j}\prod_{l=1}^{N}\left(c_{\chi l}\right)^{\nu''_{lk}}\right\}\right]$$

$$+\frac{\partial T}{\partial \rho_j}\cdot W_i \sum_{k=1}^{K}\left[\left(\nu''_{ik} - \nu'_{jk}\right)\left\{\sum_{l=1}^{n}\left(\alpha_{lk} c_{\chi l}\right)\right\}\left\{\frac{\partial k_{f,k}}{\partial T}\prod_{l=1}^{N}\left(c_{\chi l}\right)^{\nu'_{lk}} - \frac{\partial k_{b,k}}{\partial T}\prod_{l=1}^{N}\left(c_{\chi l}\right)^{\nu''_{lk}}\right\}\right]$$

The derivatives of the temperature and the reaction rate constant in the elements of the matrix are written as

$$\frac{\partial T}{\partial \rho} = \frac{1}{\sum_{j=1}^{N}\rho_j R_j}\left[\frac{1}{1-\sum_{j=1}^{N}\rho_j C_{pj} / \sum_{j=1}^{N}\rho_j R_j}\left\{-\frac{1}{2}\left(u^2+v^2\right)\right\}\right]$$

$$\frac{\partial T}{\partial (\rho u)} = \frac{1}{\sum_{j=1}^{N}\rho_j R_j}\left[\frac{u}{1-\sum_{j=1}^{N}\rho_j C_{pj} / \sum_{j=1}^{N}\rho_j R_j}\right]$$

$$\frac{\partial T}{\partial (\rho v)} = \frac{1}{\sum_{j=1}^{N}\rho_j R_j}\left[\frac{v}{1-\sum_{j=1}^{N}\rho_j C_{pj} / \sum_{j=1}^{N}\rho_j R_j}\right]$$

$$\frac{\partial T}{\partial E} = \frac{1}{\sum_{j=1}^{N}\rho_j R_j}\left[\frac{-1}{1-\sum_{j=1}^{N}\rho_j C_{pj} / \sum_{j=1}^{N}\rho_j R_j}\right]$$

$$\frac{\partial T}{\partial \rho_i} = \frac{1}{\sum_{j=1}^{N}\rho_j R_j}\left[\frac{1}{1-\sum_{j=1}^{N}\rho_j C_{pj} / \sum_{j=1}^{N}\rho_j R_j}\left\{h_i - \frac{\sum_{j=1}^{N}\rho_j C_{pj}}{\sum_{j=1}^{N}\rho_j R_j}R_i T\right\} - R_i T\right]$$

$$\frac{dk_{b,k}}{dT} = \frac{1}{K_{eq,k}}\left[\frac{dk_{f,k}}{dT} - \frac{k_{f,k}}{T}\left[\sum_{j=1}^{N}\left\{\left(\nu''_{ik} - \nu'_{jk}\right)\frac{h_i}{R_i T}\right\} - \sum_{j=1}^{N}\left(\nu''_{ik} - \nu'_{jk}\right)\right]\right].$$

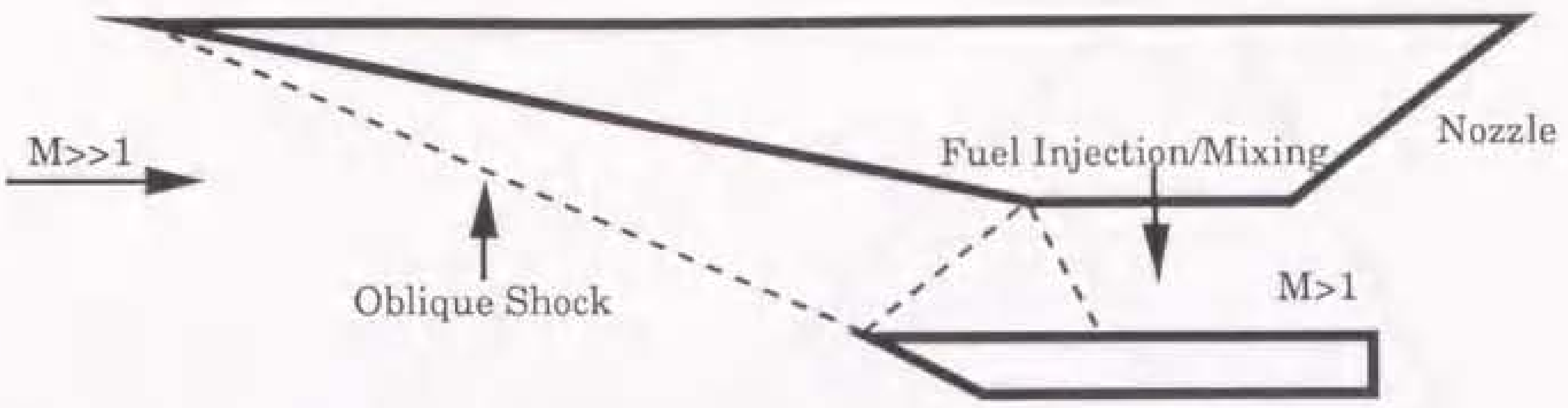

Figure 1.1 Schematic picture of propulsion concept for a hypersonic vehicle as the supersonic combustion ramjet (SCRAMJET), where fuel is injected, mixed, and burned in the combustor section.

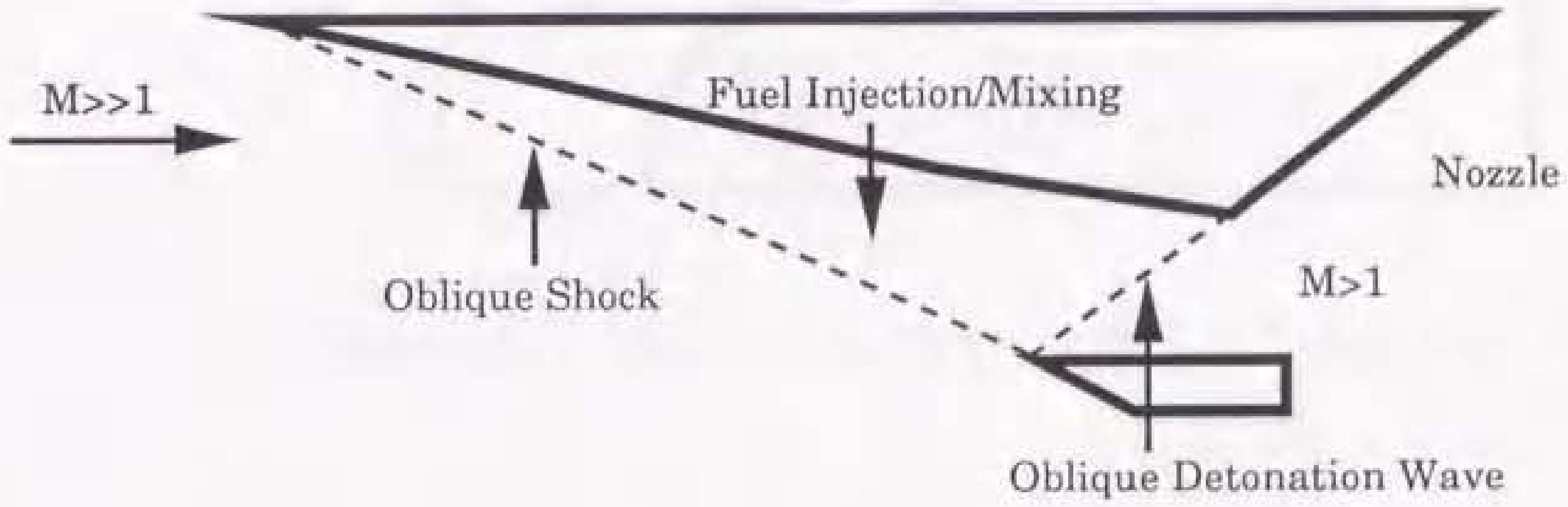

Figure 1.2 Schematic picture of propulsion concept for a hypersonic vehicle as the oblique detonation wave engine (ODWE), where fuel is injected on the forebody and detonation occurs later due to oblique shocks (little or no combustor length is needed).

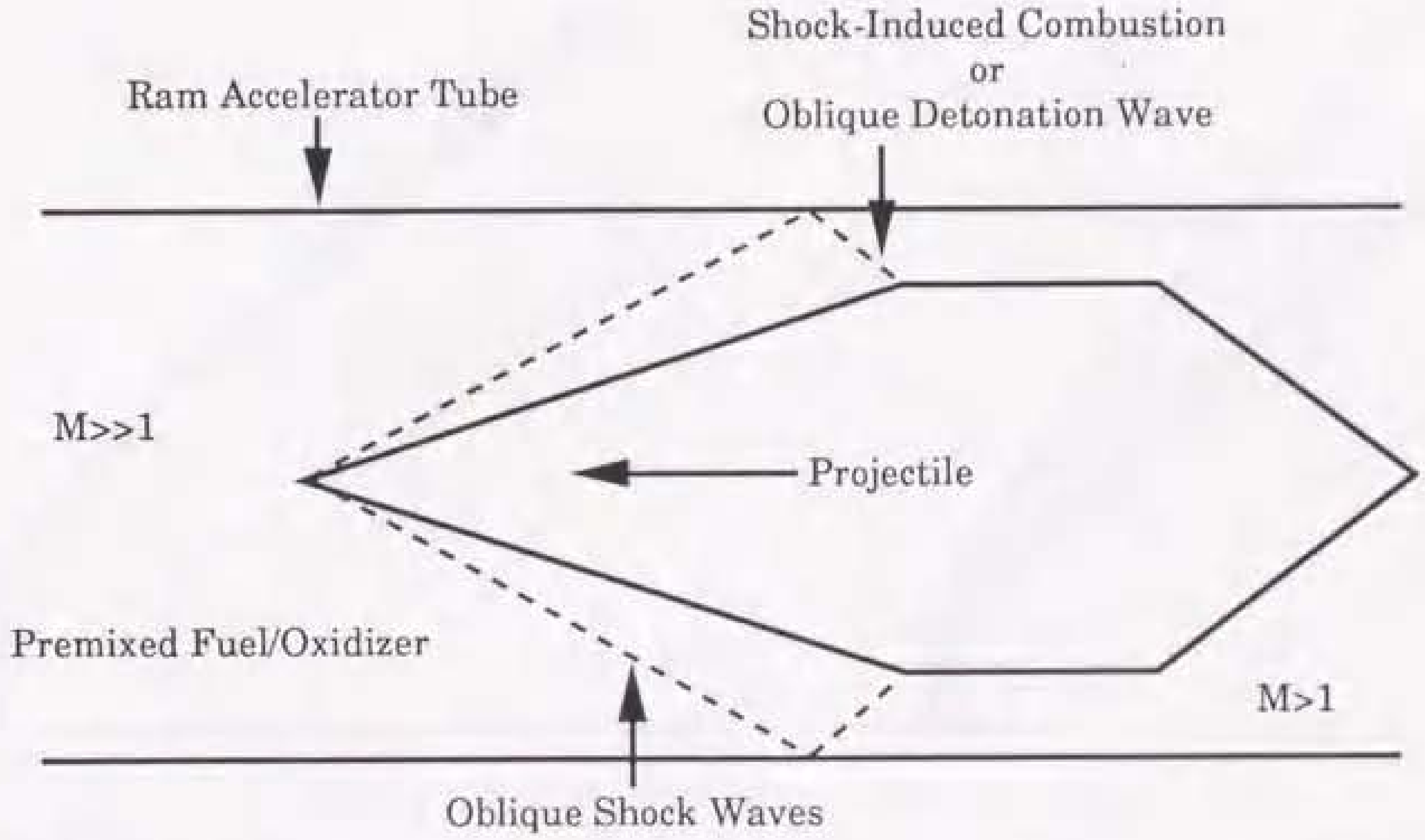

Figure 1.3 Schematic picture of propulsion concept for a hypersonic vehicle as the ram accelerator in a tube concept: A projectile inside a tube filled with a combustible mixture is self propelled to high velocities by burning of the mixture around and behind the projectile.

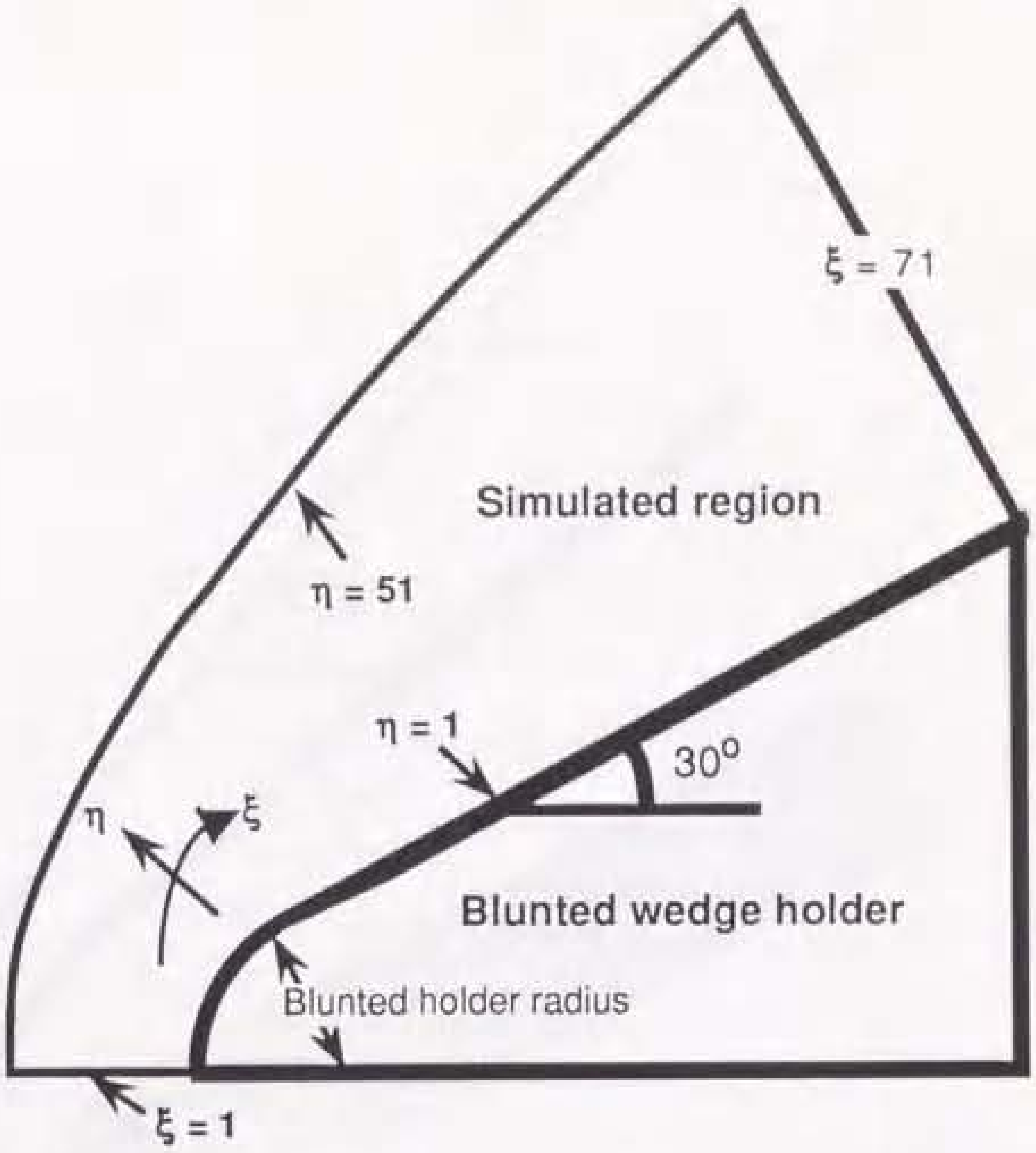

Figure 3.1 Schematic pisture showing the computational flowfield

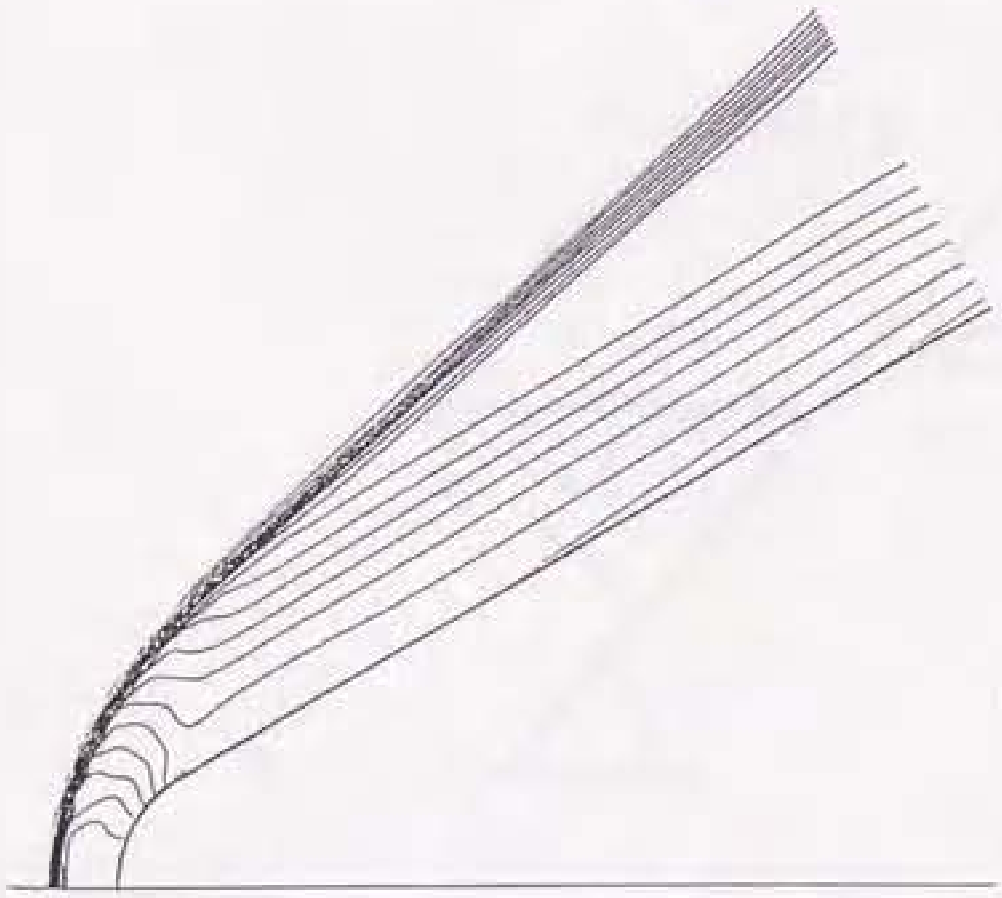

Figure 3.2 Temperature contour plots of a non-reacting flow; the incident Mach number M_∞=6 and the wedge tip radius=L^*

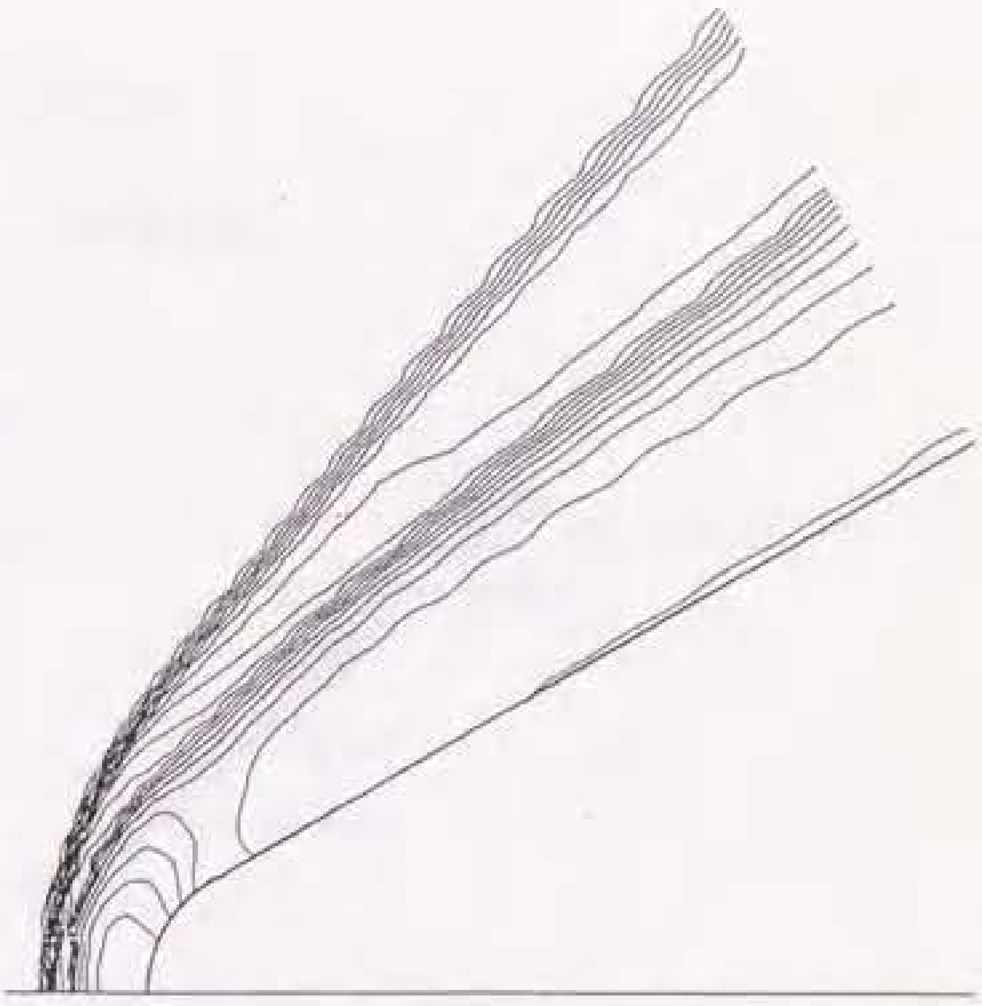

Figure 3.3 Temperature contour plots of a reacting flow; the incident Mach number M_∞=6 and the wedge tip radius=L^*

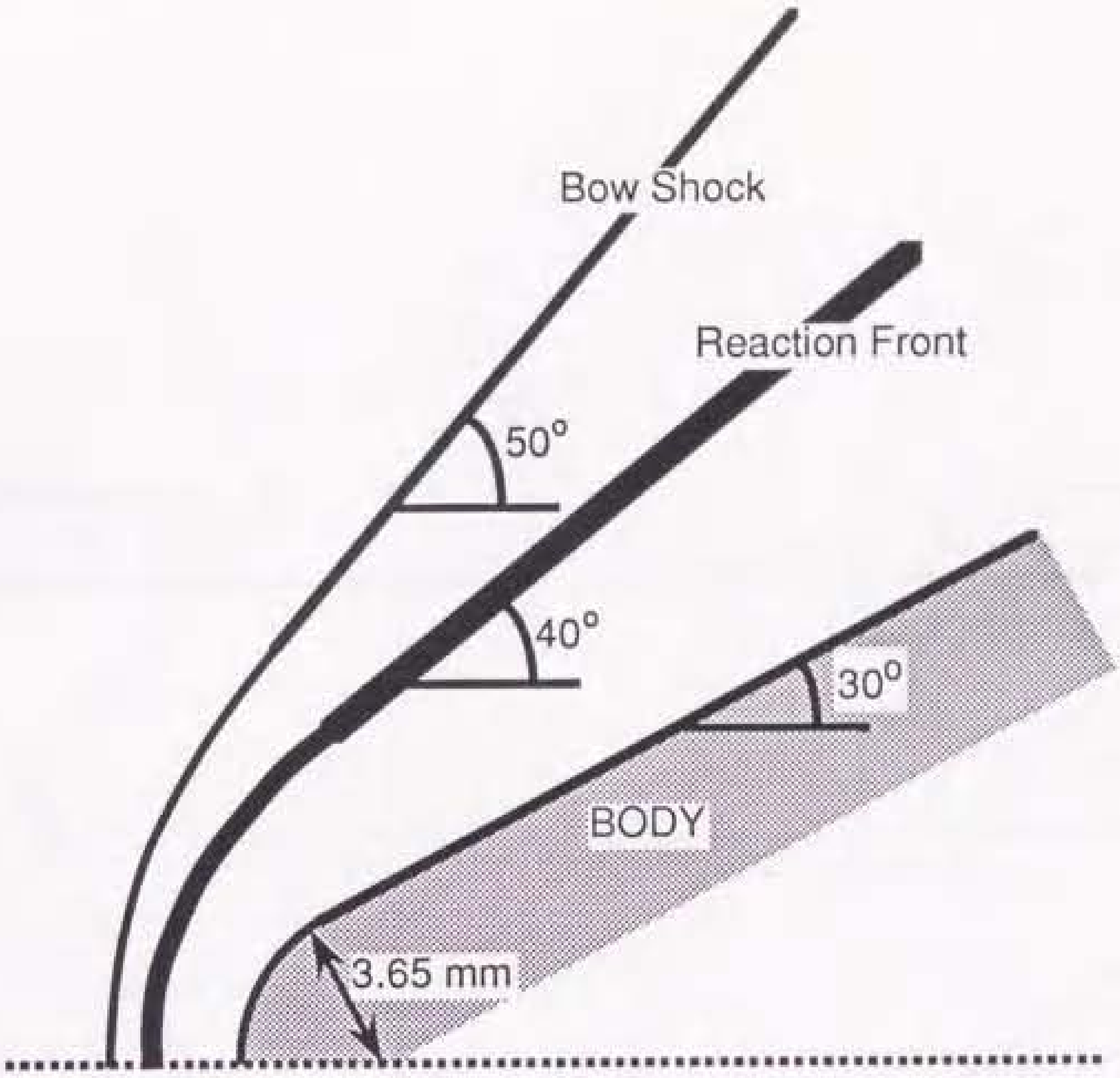

Figure 3.4 Schematic picture of the temperature contour plots to explain the flow features of Fig. 3.3

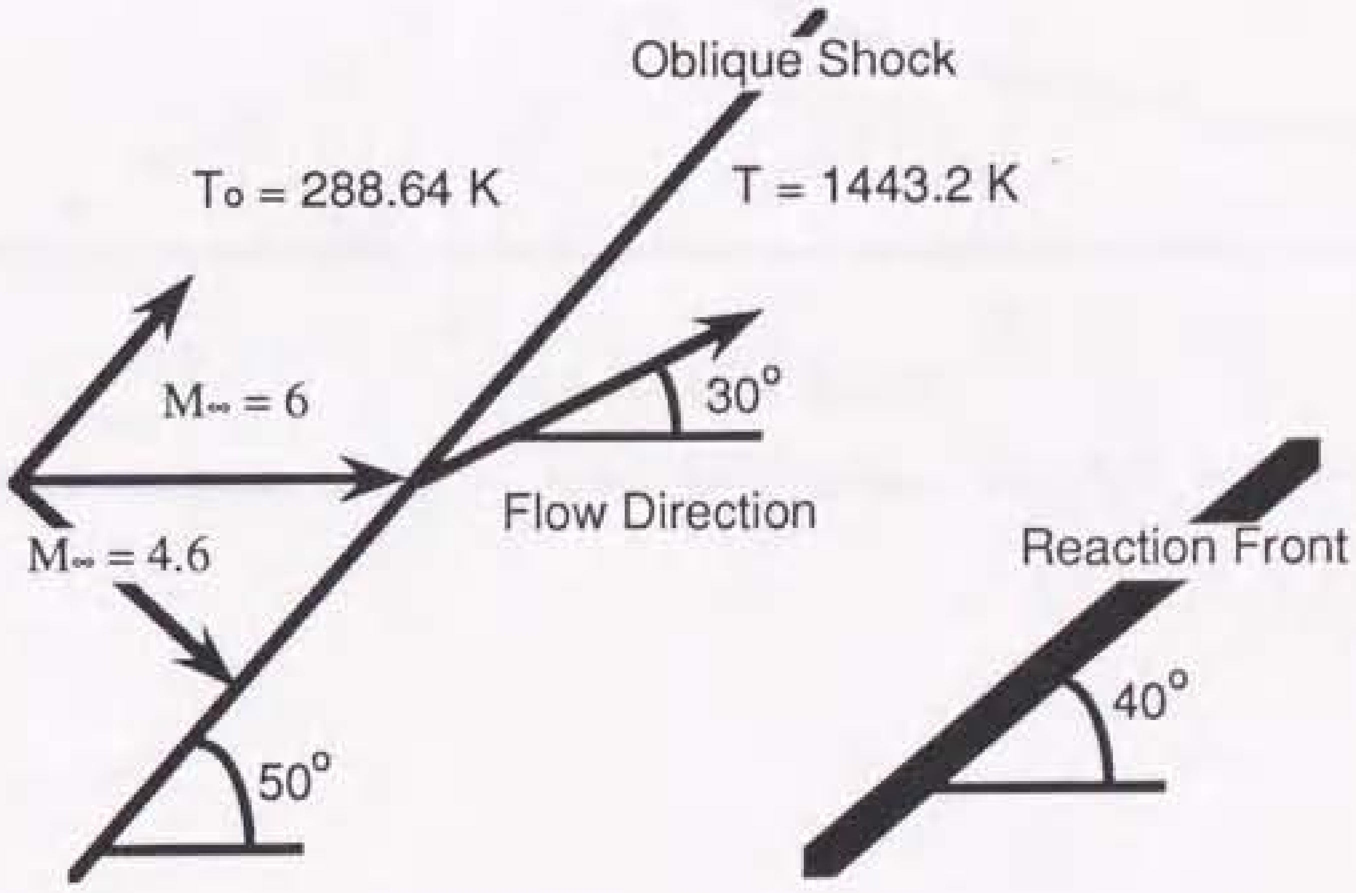

Figure 3.5 Schematic picture showing the relation between the oblique shock and the reaction front

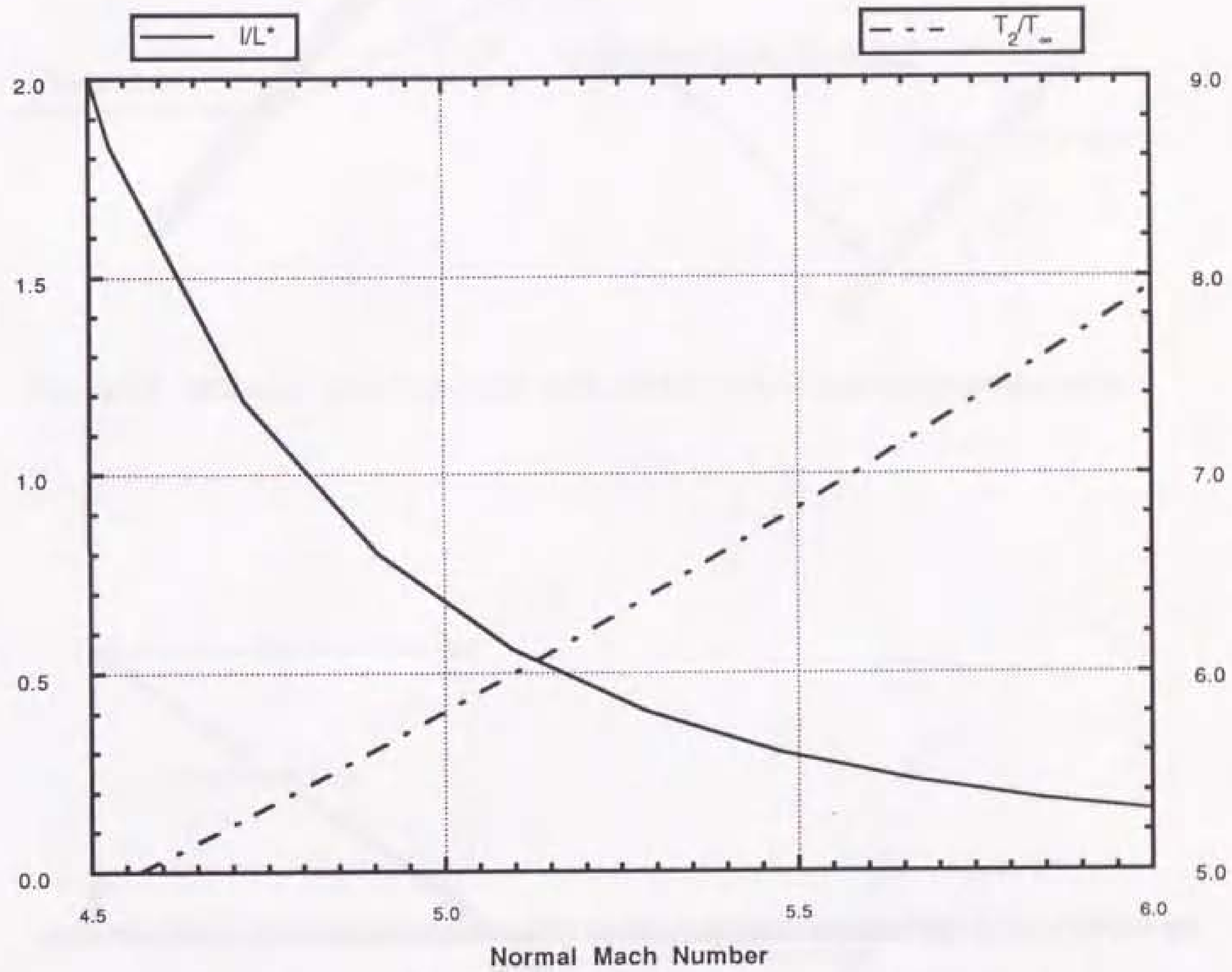

Figure 3.6 Shock-relationl Mach number M_∞ versus the temperature ratio T_2/T_∞ and the induction length $l(T_2)$

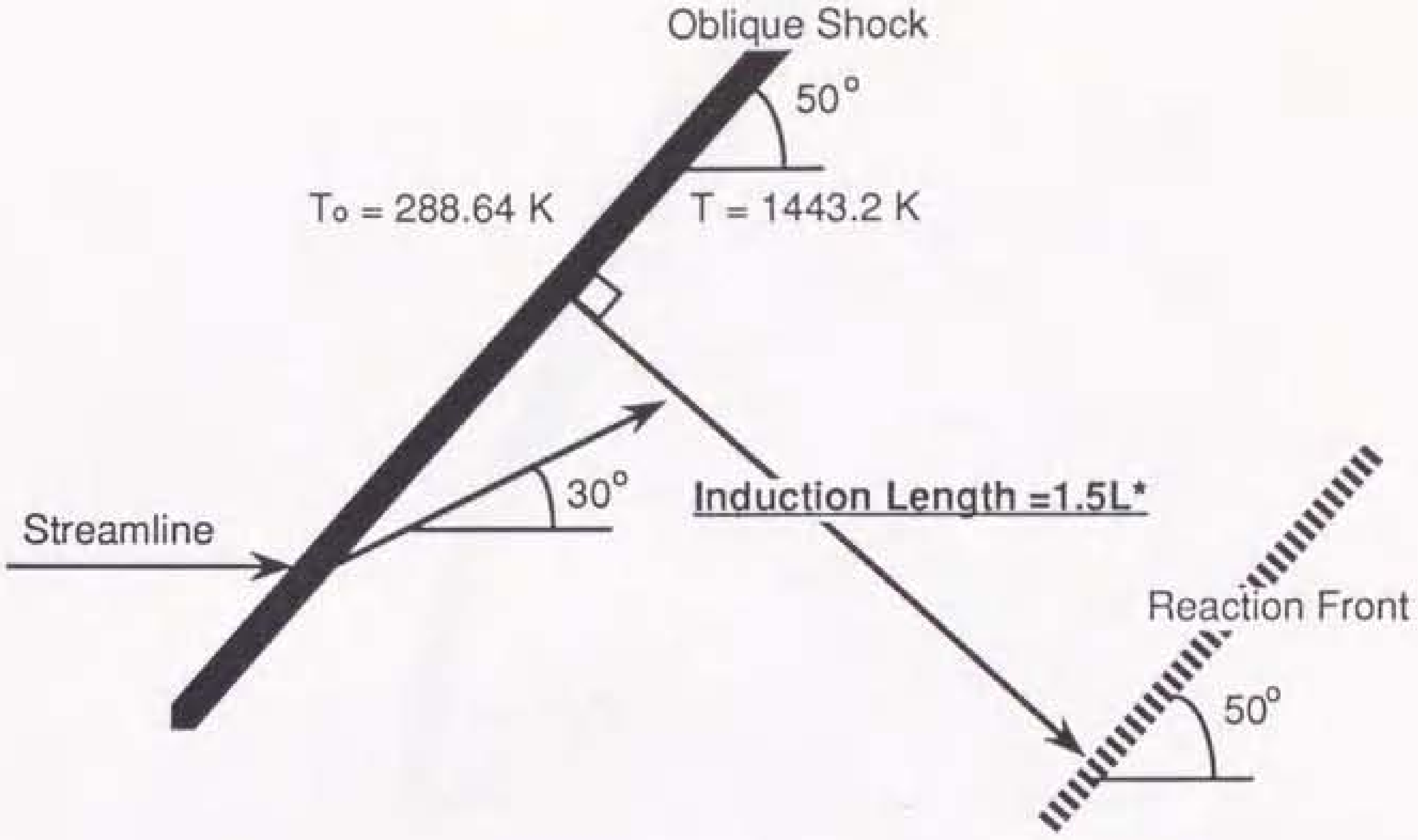

Figure 3.7 Schematic picture showing the flowfield behind a stationary oblique shock

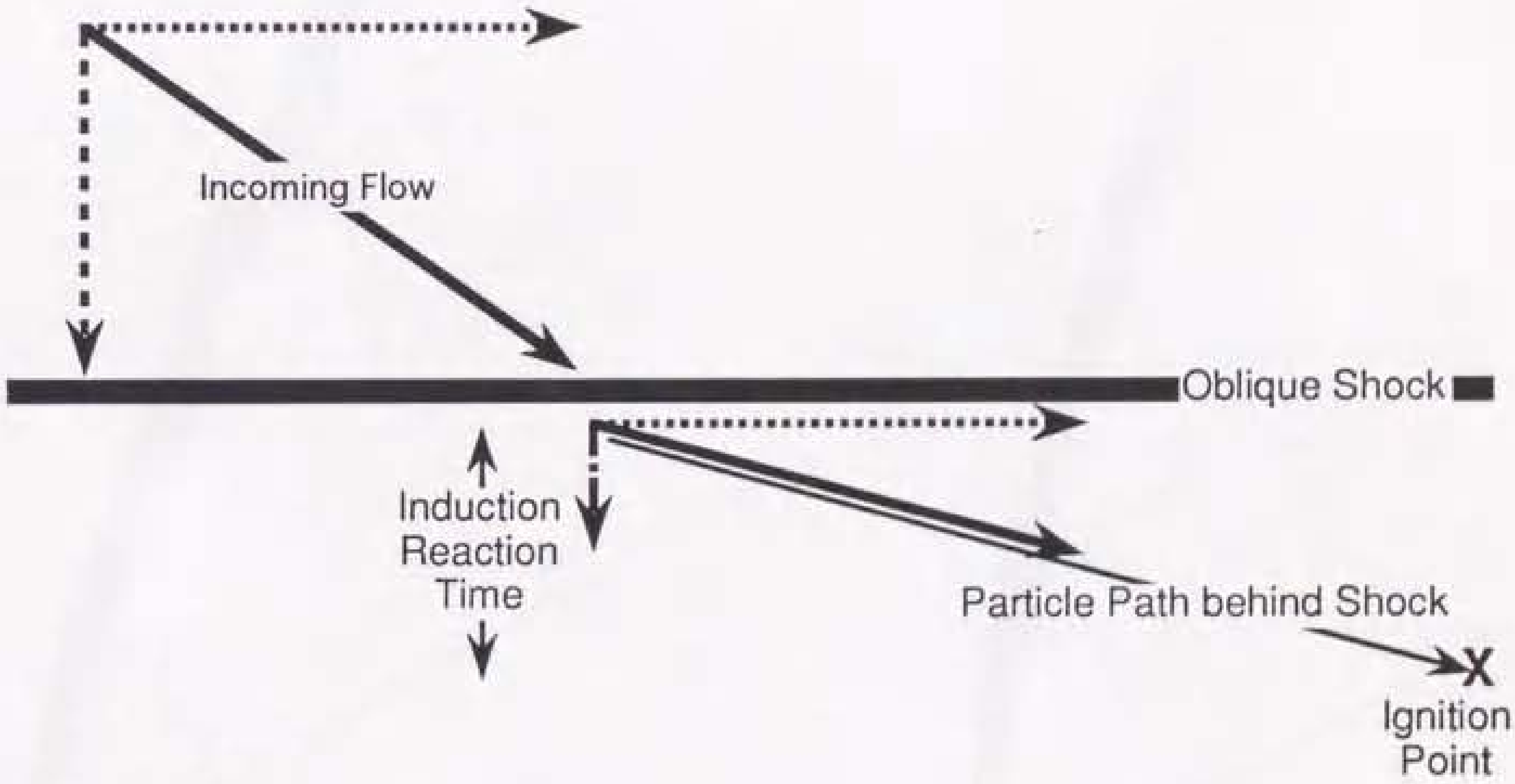

Figure 3.8 Schematic picture showing the particle path behind an oblique shock and the ignition point

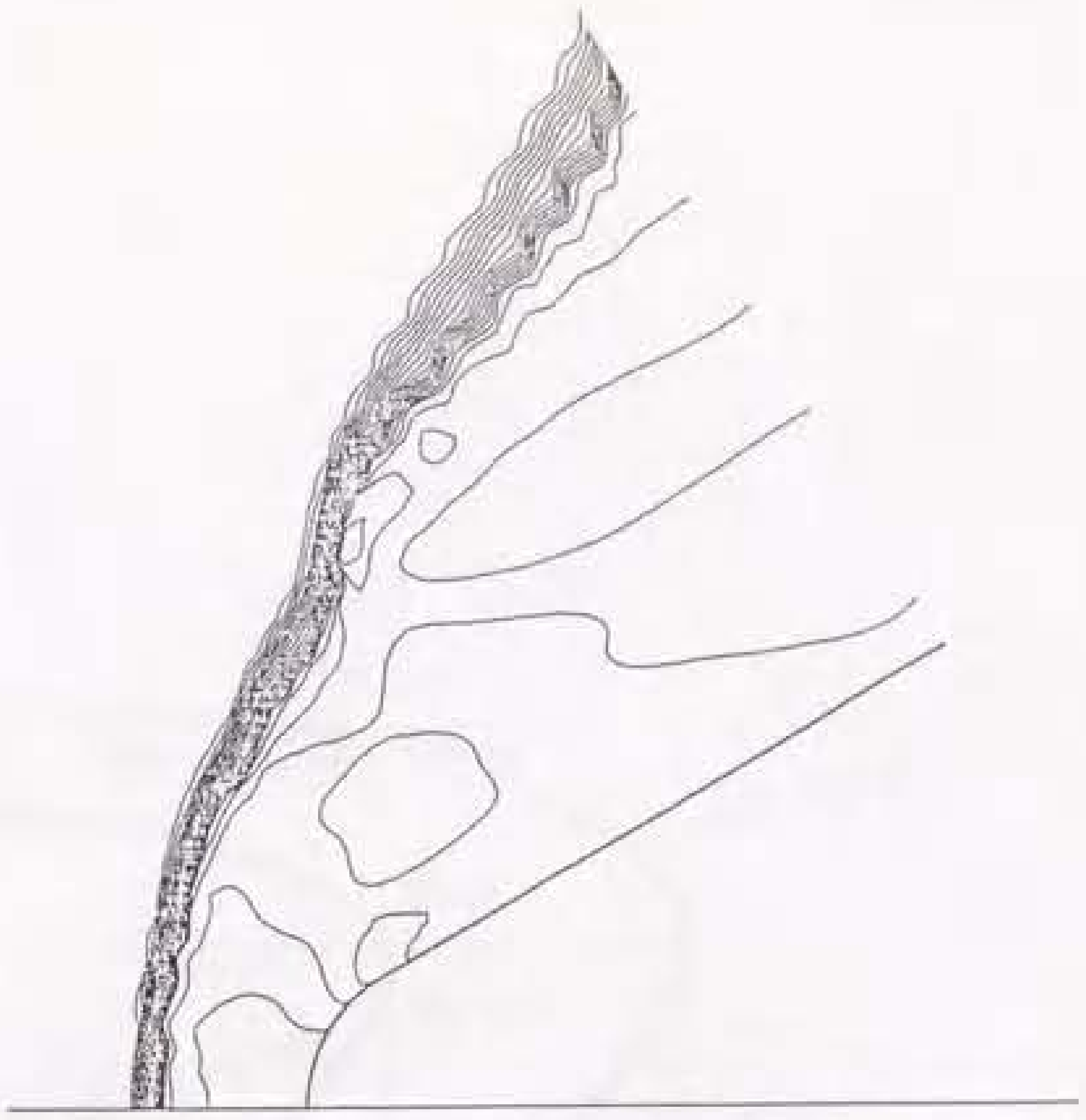

Figure 3.9 Temperature contour plots of a reacting flow; the incident Mach number M∞=6 and the wedge tip radius=$3L^*$, at time t=44

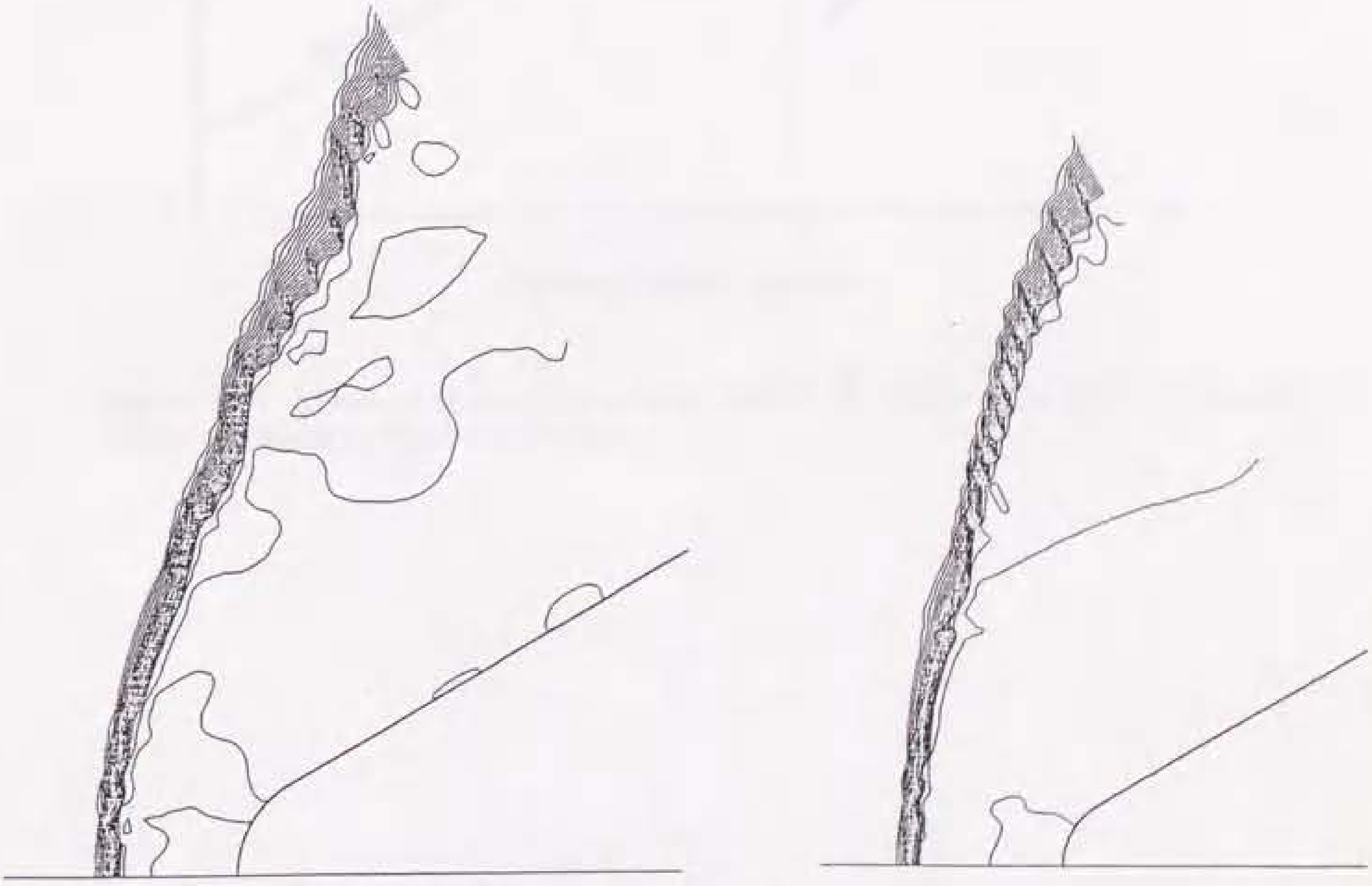

(a)

(b)

Figure 3.10 Temperature contour plots of a reacting flow; the incident Mach number M∞=6 and the wedge tip radius=$3L^*$, (a) at time t=111, (b) at time t=522

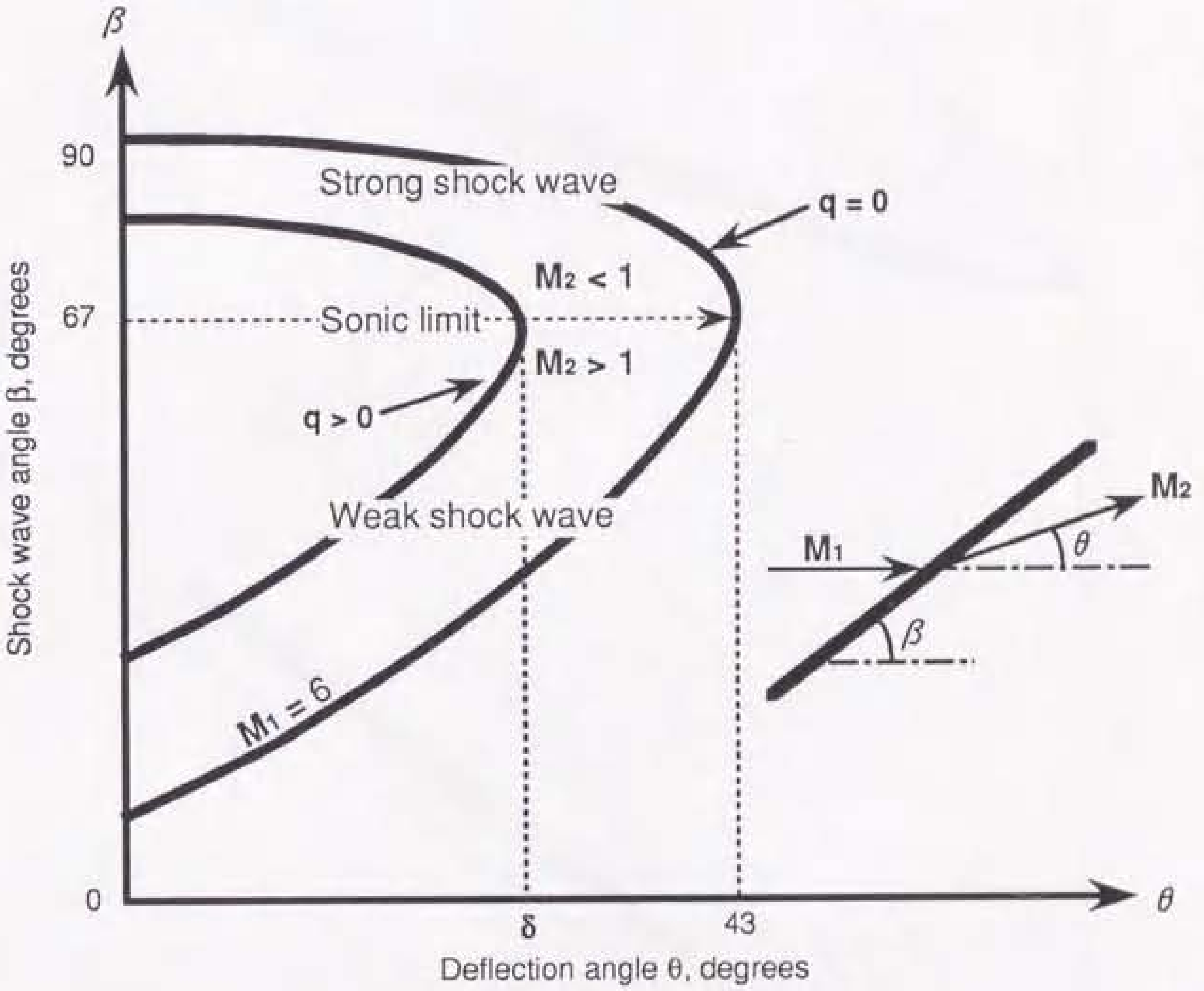

Figure 3.11 Shock polar curve represented by θ–β (deflection angle and shock angle) plot for the incident Mach number M_∞

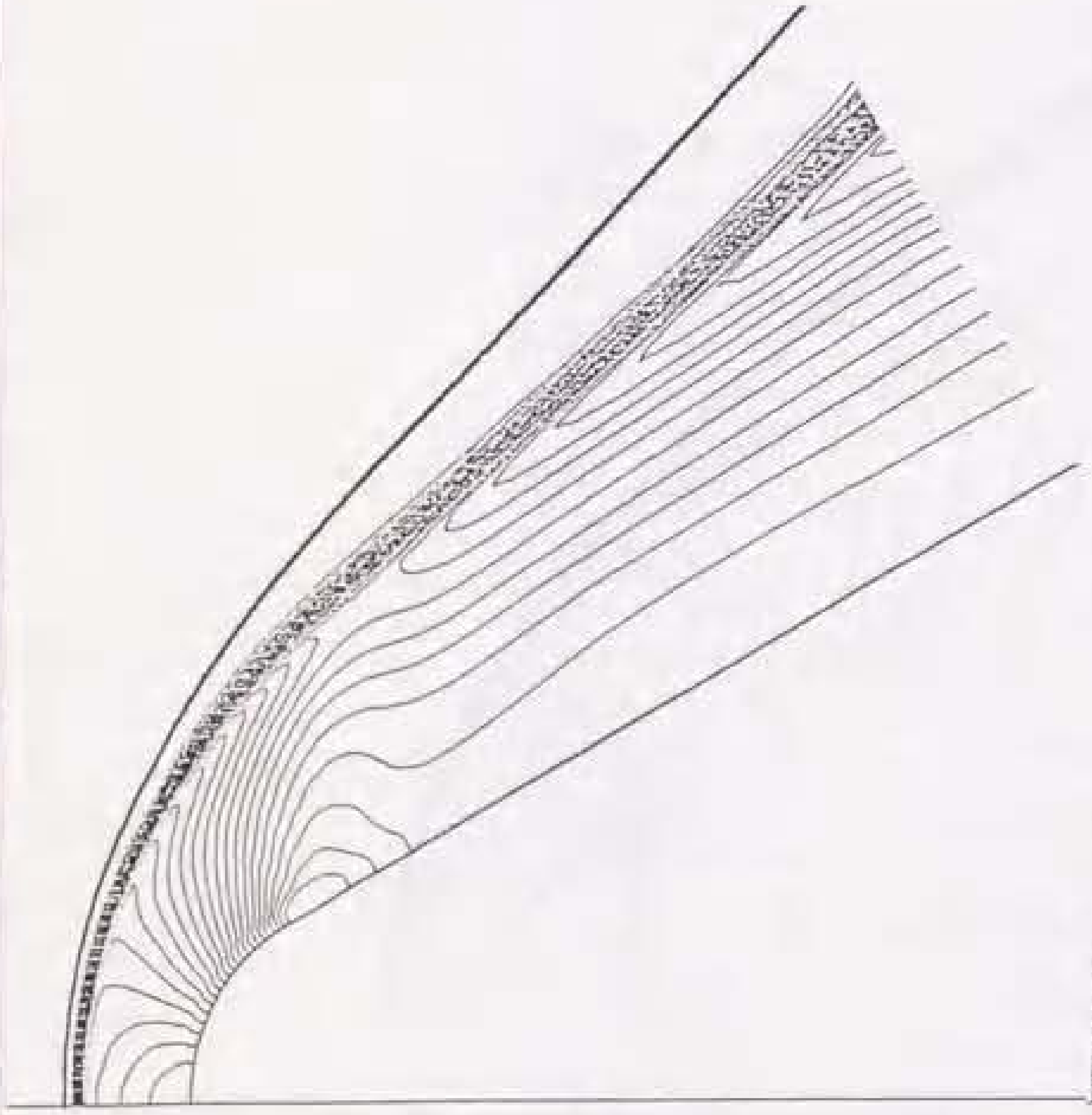

Figure 3.12 The shock location and water density contour plots; half angle 30 degrees, Mach number M_∞=6 and wedge tip radius=*2.25 mm*

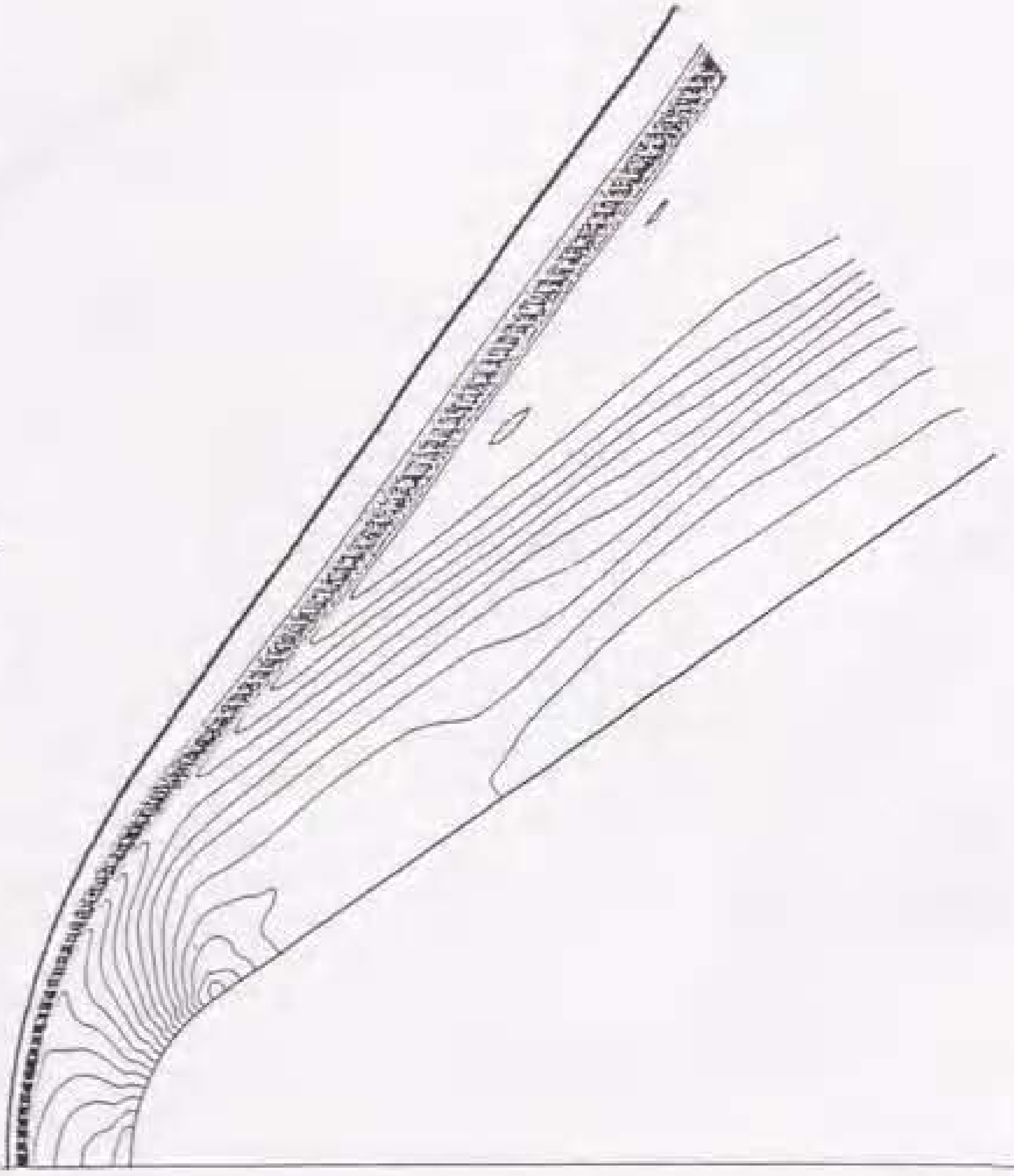

Figure 3.13 The shock location and water density contour plots; half angle 35 degrees, Mach number M_∞=6 and wedge tip radius=*2.25 mm*

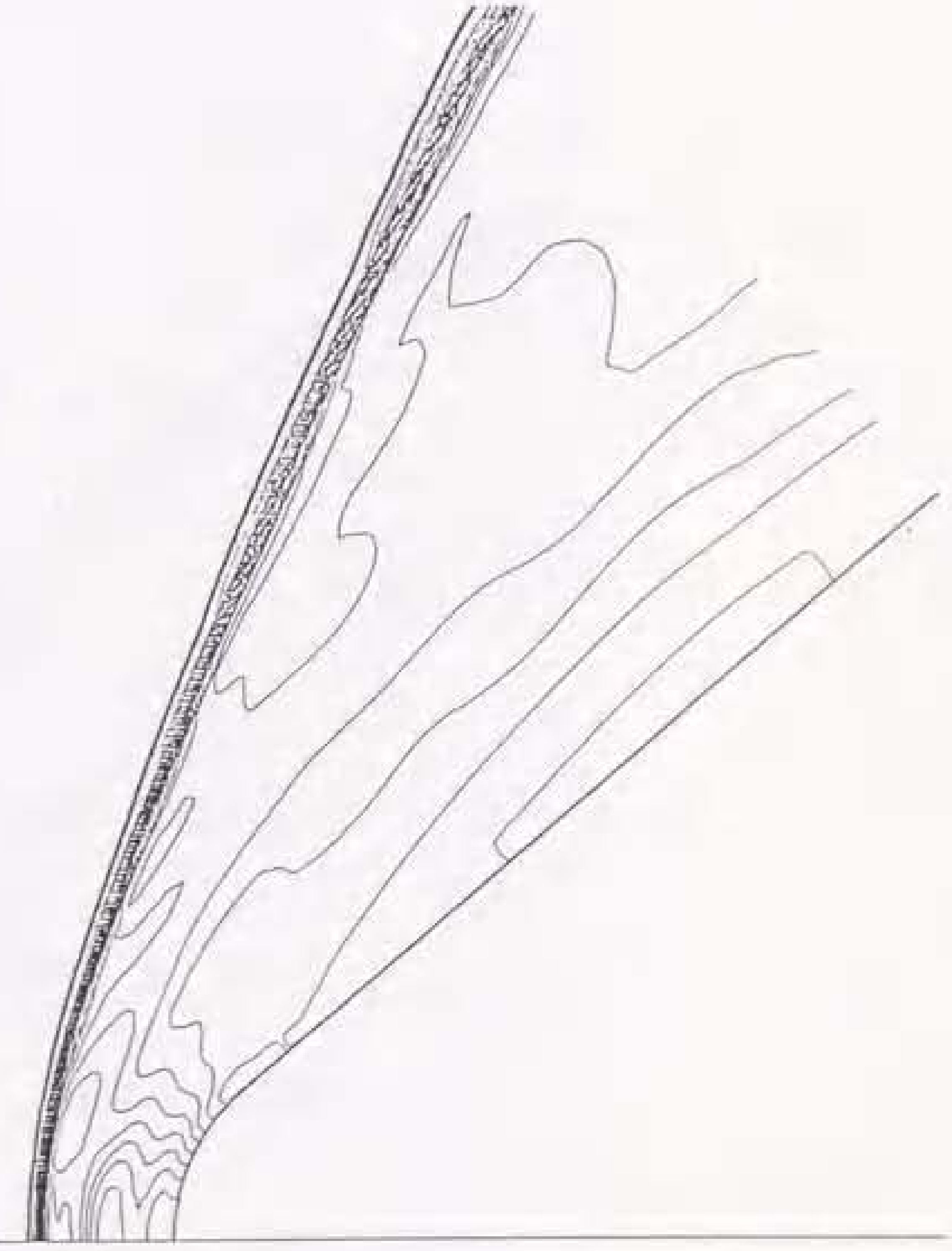

Figure 3.14 The shock location and water density contour plots; half angle 40 degrees, Mach number M_∞=6 and wedge tip radius=*2.25 mm*

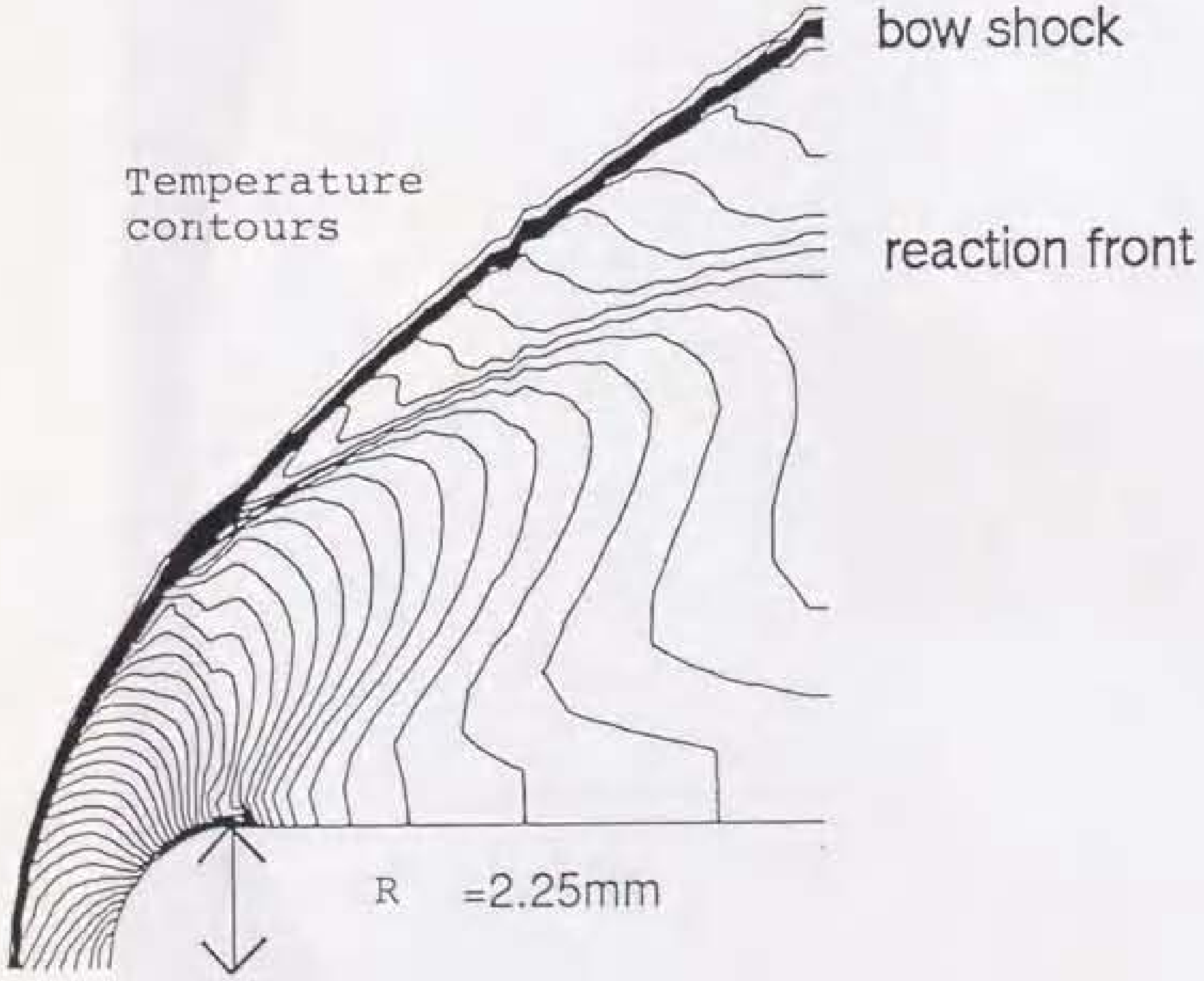

Figure 3.15 Temperature contour plots of an axisymmetric blunt body for $L_\infty=22.5mm$, $M_\infty=6$, $T_\infty=288.65K$, $P_\infty=0.1atm$

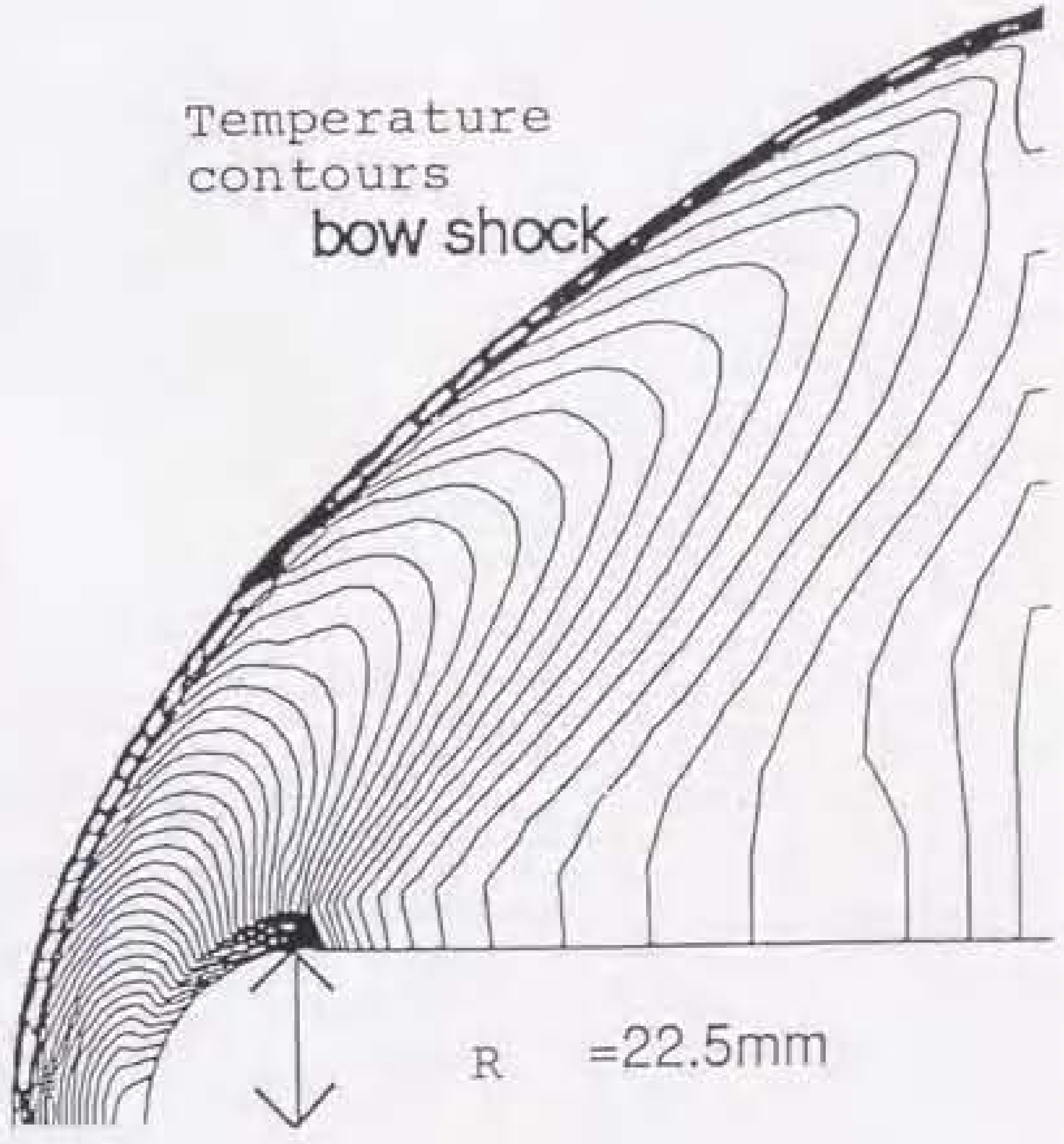

Figure 3.16 Temperature contour plots of an axisymmetric blunt body for $L_\infty=2.25mm$, $M_\infty=6$, $T_\infty=288.65K$, $P_\infty=0.1atm$

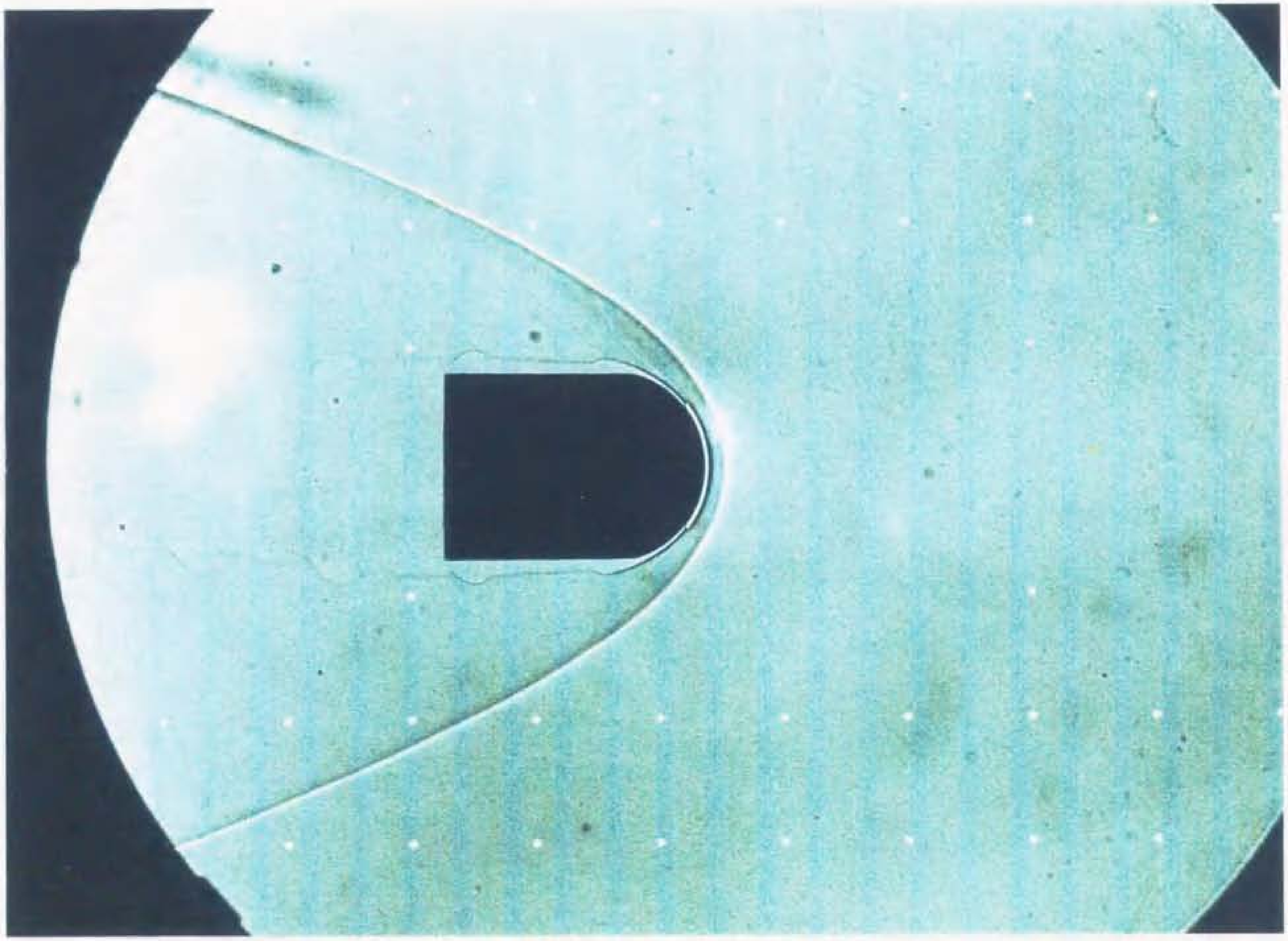

Figure 4. 1 Shadowgraph of a 15 mm blunt-nosed ballistic-range projectile at 1,685 m/sec in premixed stoichiometric hydrogen-air (Courtesy of H.F.Lehr)

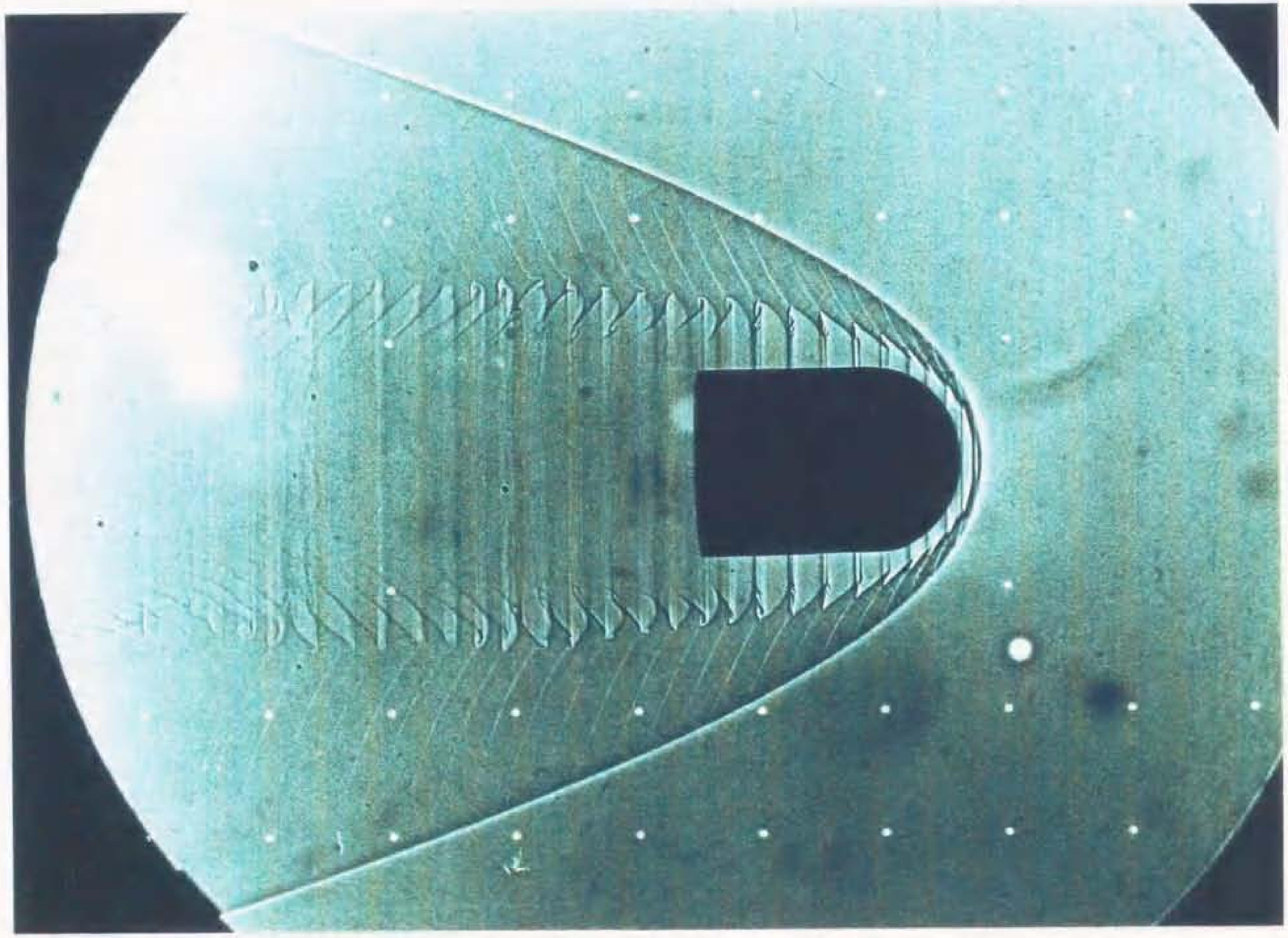

Figure 4. 2 Shadowgraph of a 15 mm blunt-nosed ballistic-range projectile at 1,931 m/sec in premixed stoichiometric hydrogen-air (Courtesy of H.F.Lehr)

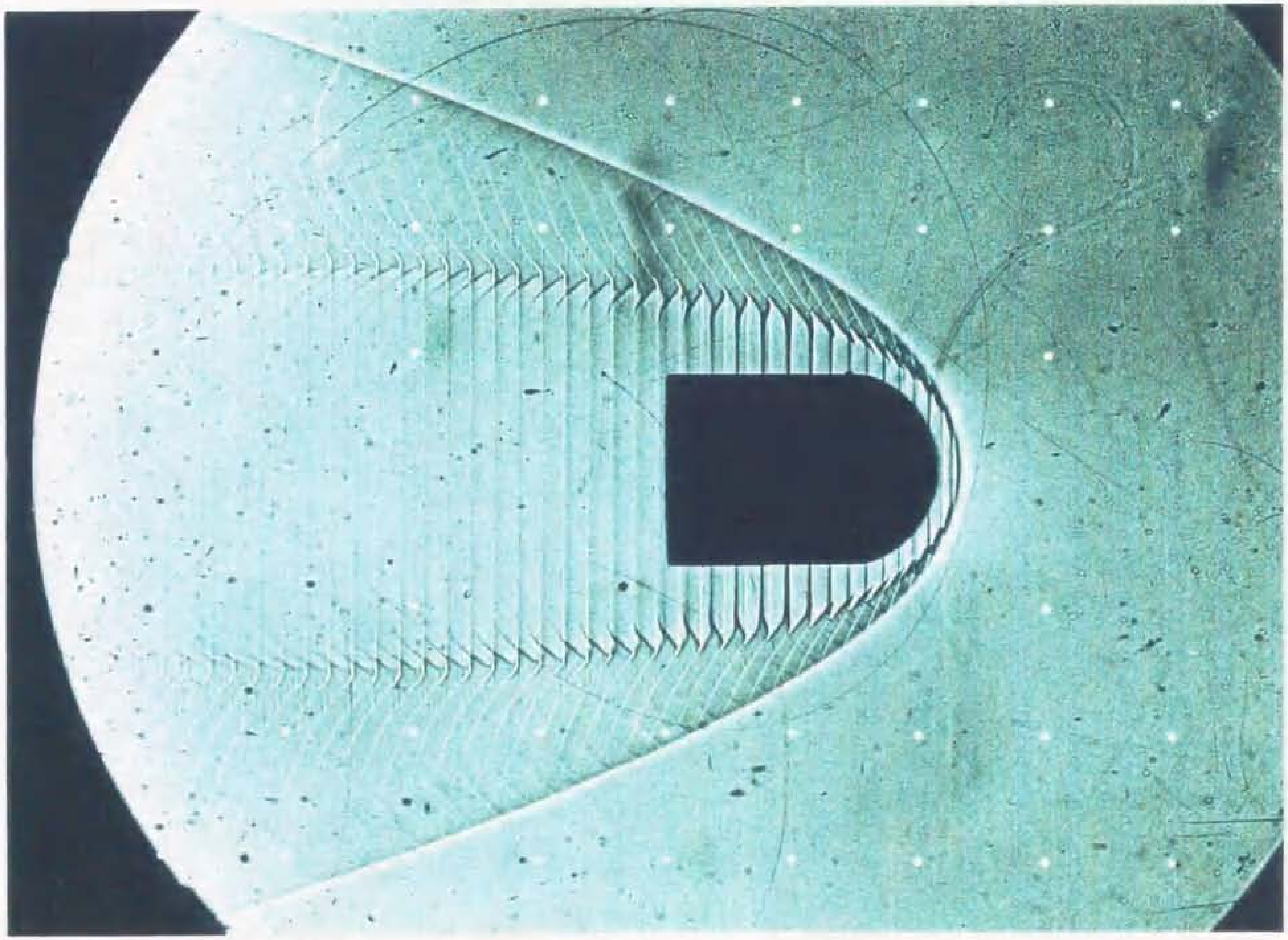

Figure 4. 3 Shadowgraph of a 15 mm blunt-nosed ballistic-range projectile at 2029 m/sec in premixed stoichiometric hydrogen-air (Courtesy of H.F.Lehr)

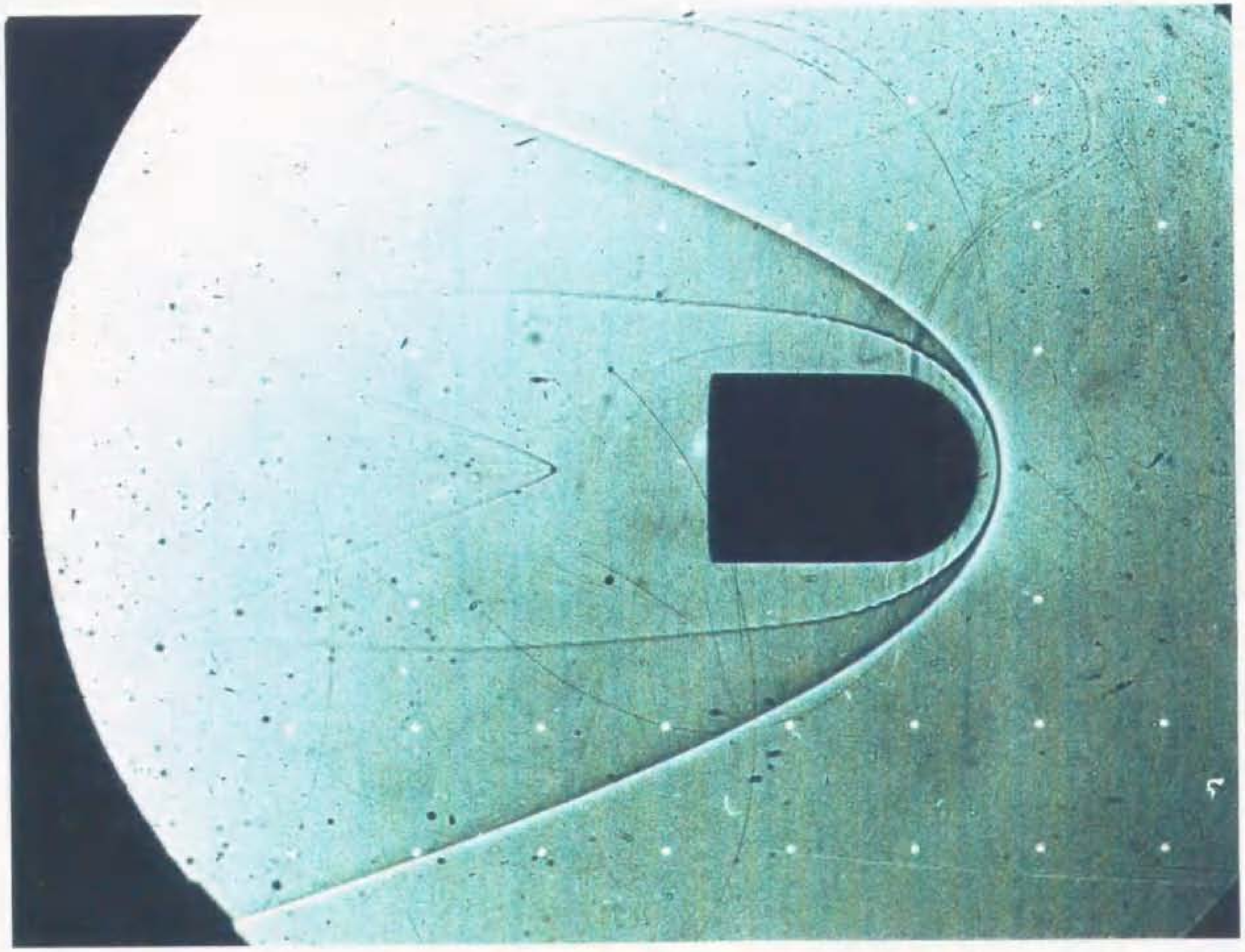

Figure 4. 4 Shadowgraph of a 15 mm blunt-nosed ballistic-range projectile at 2058 m/sec in premixed stoichiometric hydrogen-air (Courtesy of H.F.Lehr)

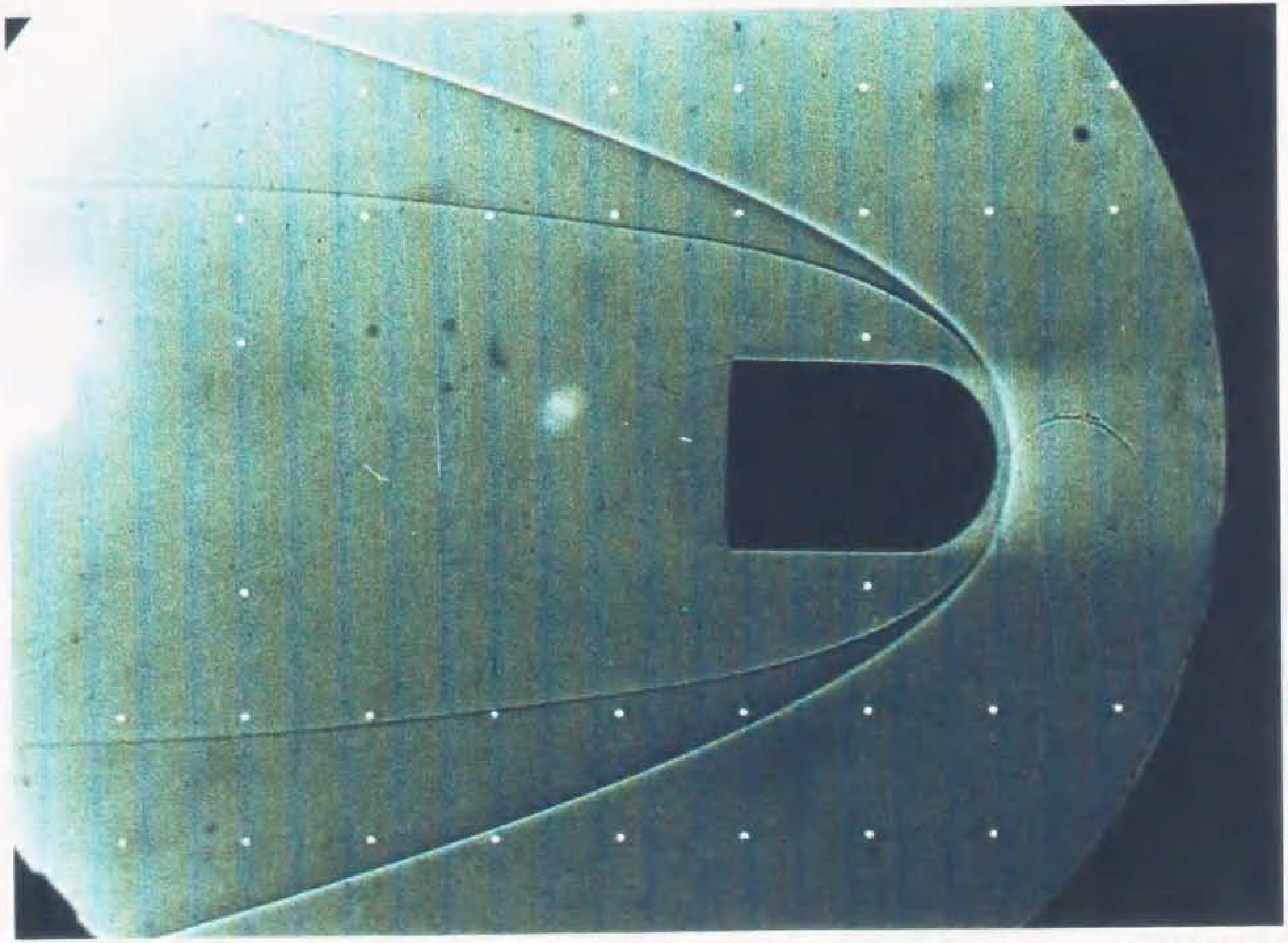

Figure 4. 5 Shadowgraph of a 15 mm blunt-nosed ballistic-range projectile at 2605 m/sec in premixed stoichiometric hydrogen-air (Courtesy of H.F.Lehr)

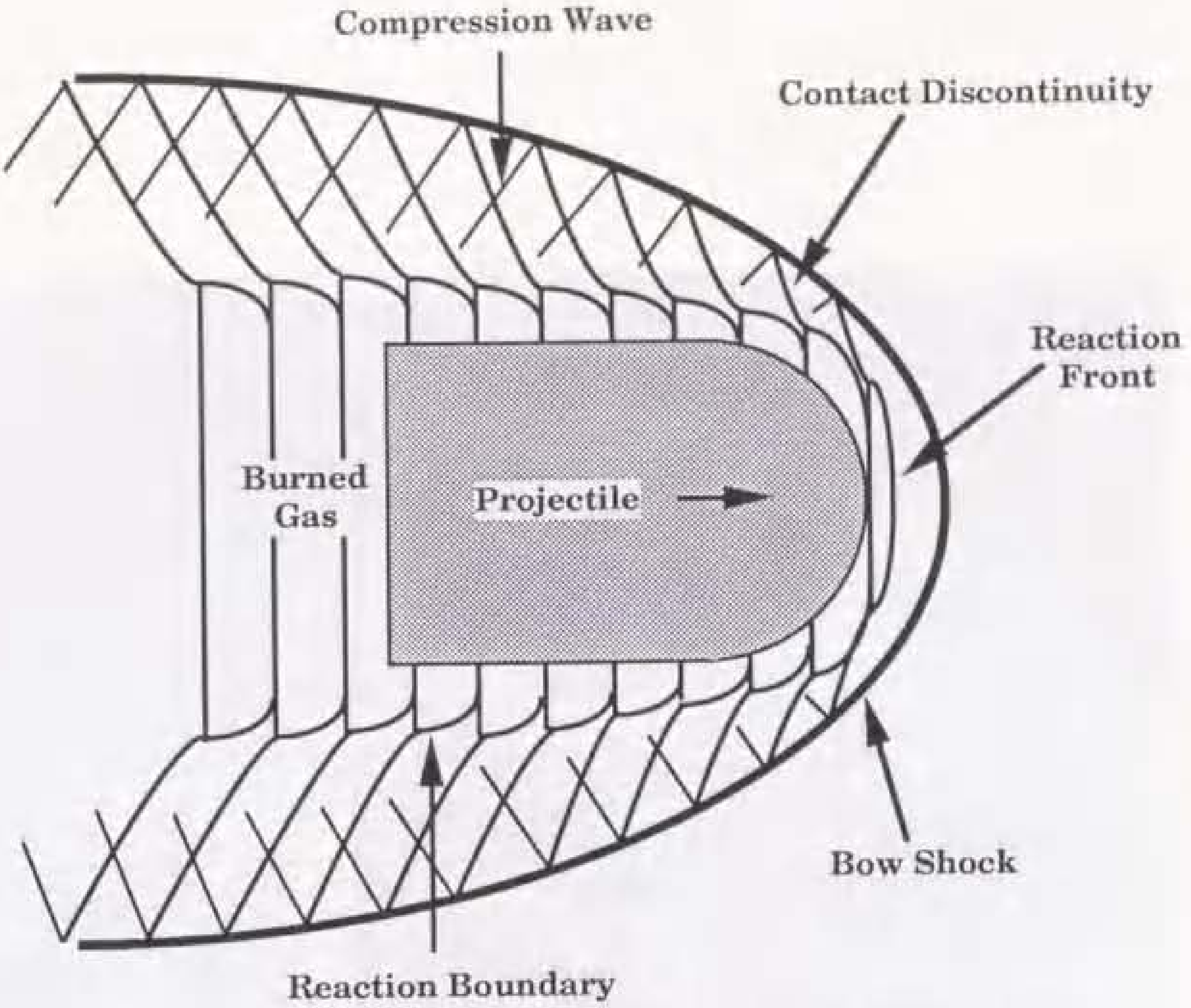

Figure 4.6 Schematic of the flow fields structures seen in shadowgraphs of periodic ballistic-range experiments

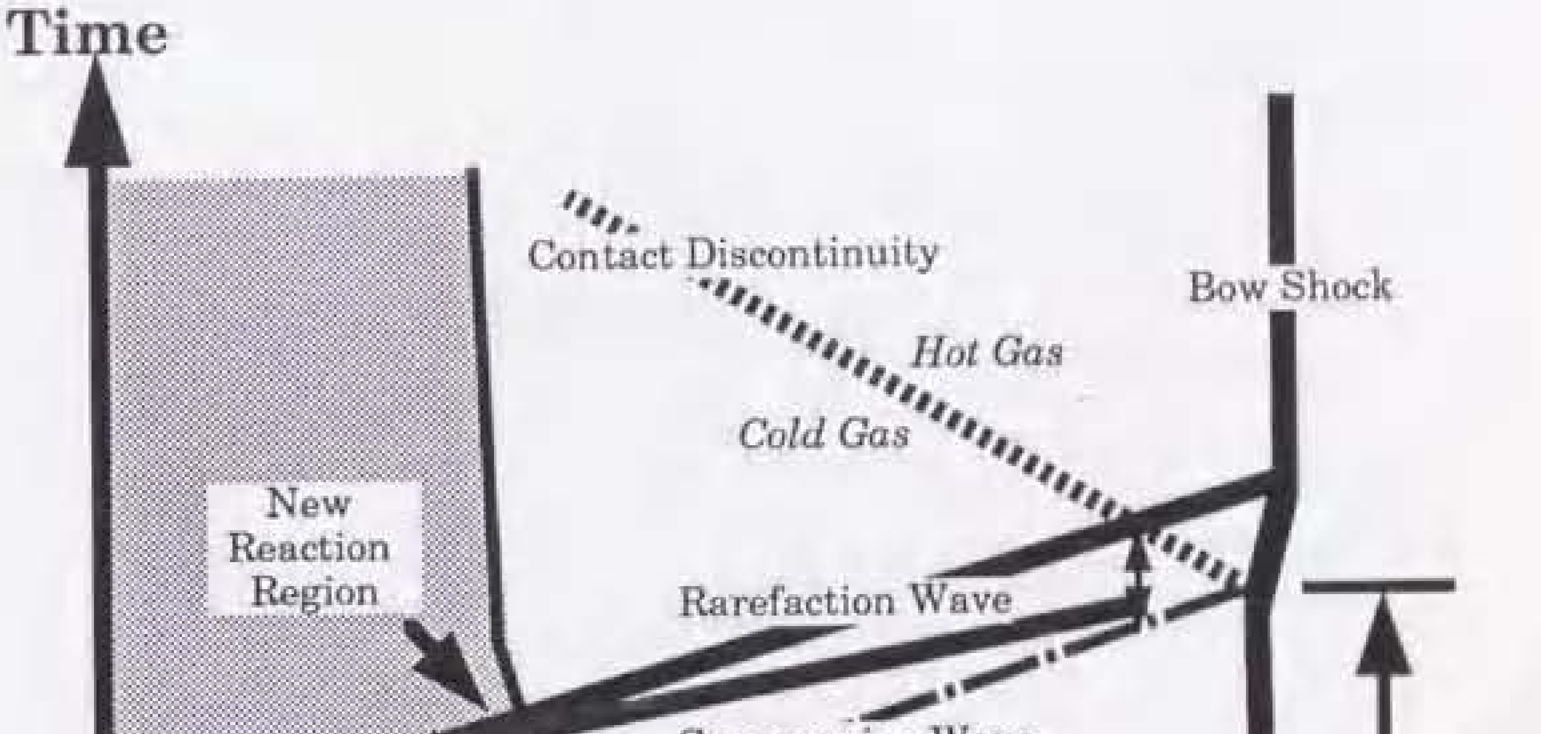

Figure 4.7 X-t diagram of the wave interaction model proposed by McVey and Toong (1971)

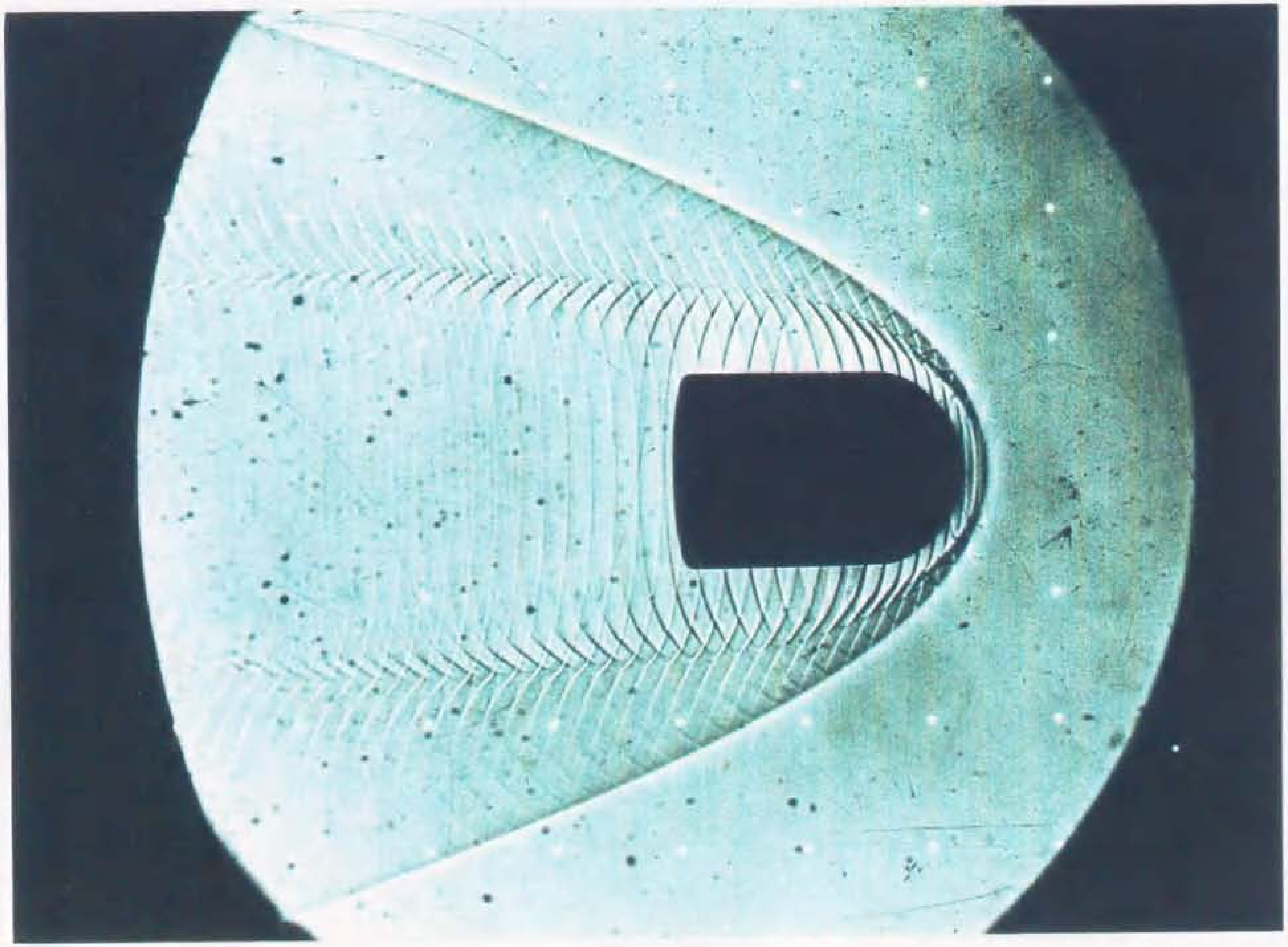

Figure 4.8 Off-axis view shadowgraph of the Lehr's experiment in Figure 4.3 (Courtesy of H.F.Lehr)

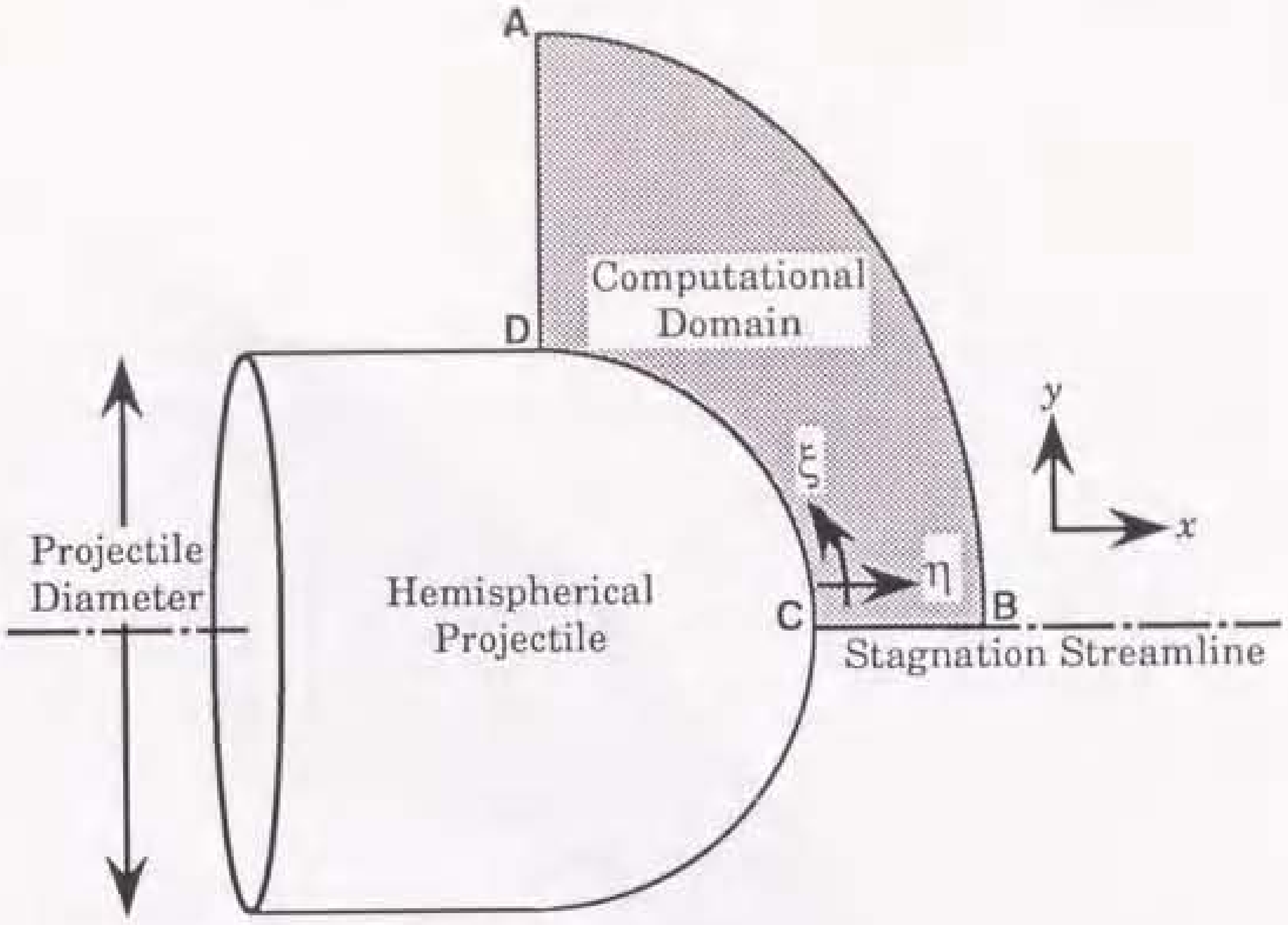

Figure 5.1 Computational domain

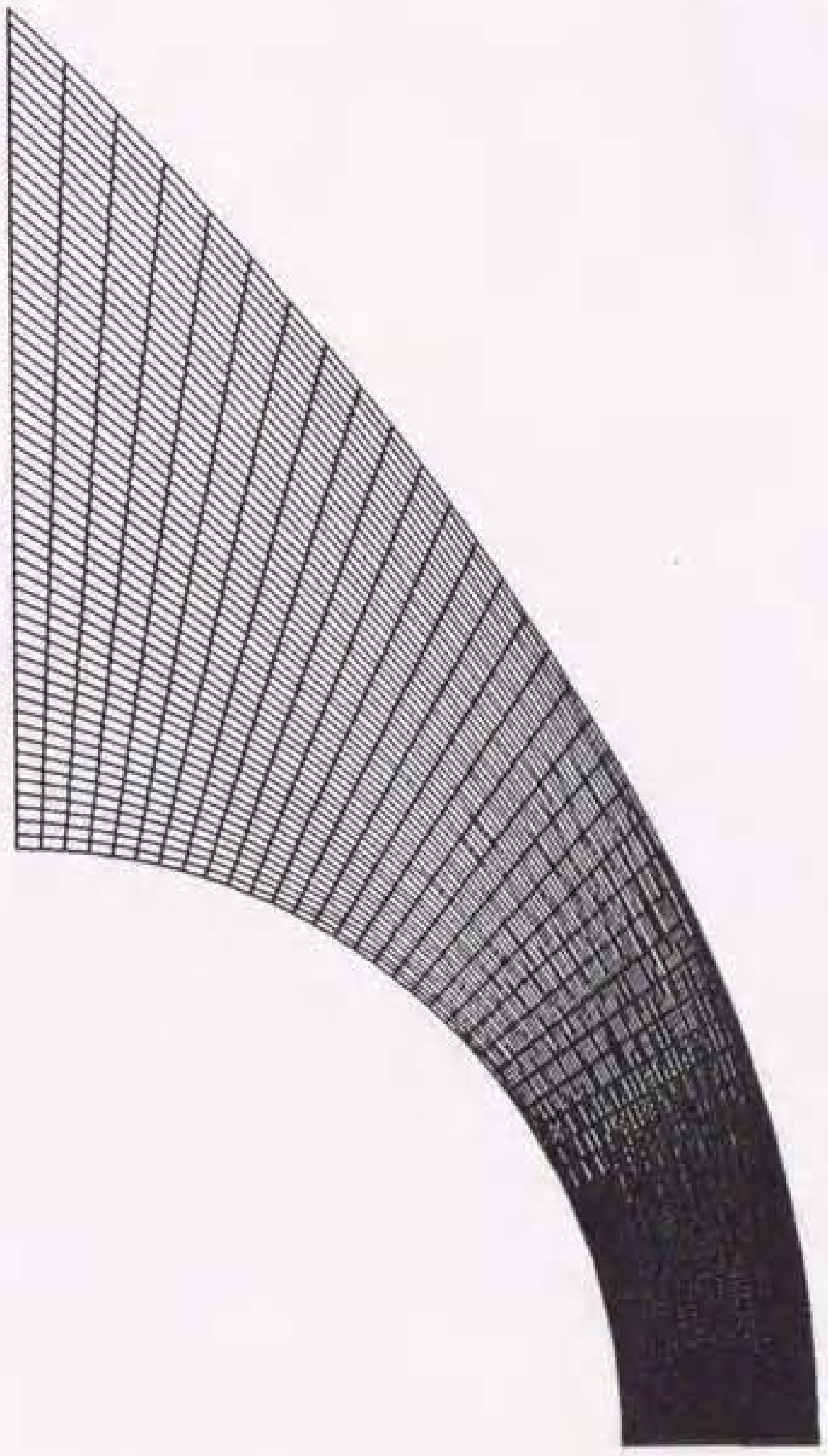

Figure 5.2 Computational grid distributions

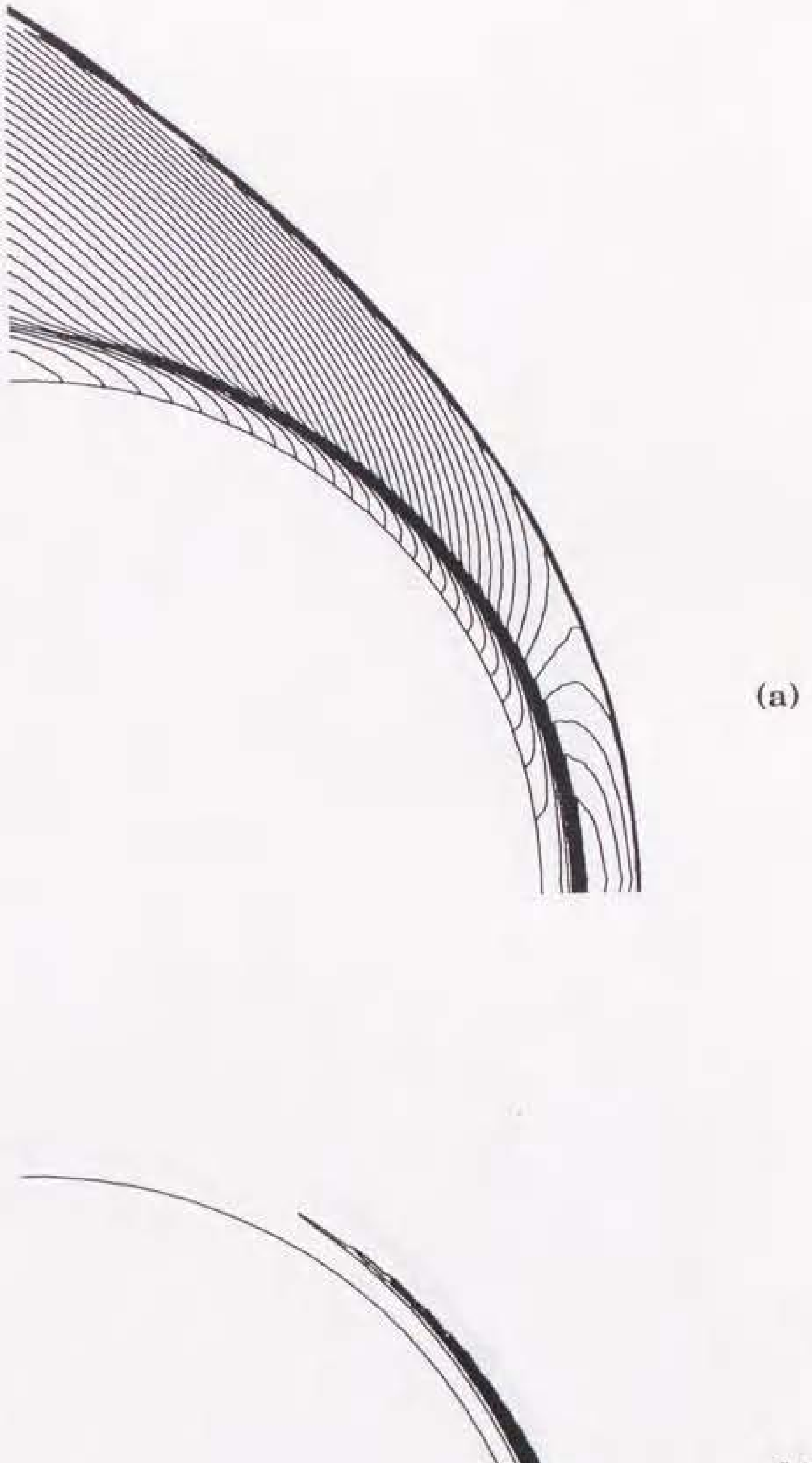

Figure 5.3 Contour plots for the projectile radius $5L_\bullet$ with the simplified chemical reaction mechanism: (a) density contour plots, (b) $\rho\omega_\beta$ contour plots

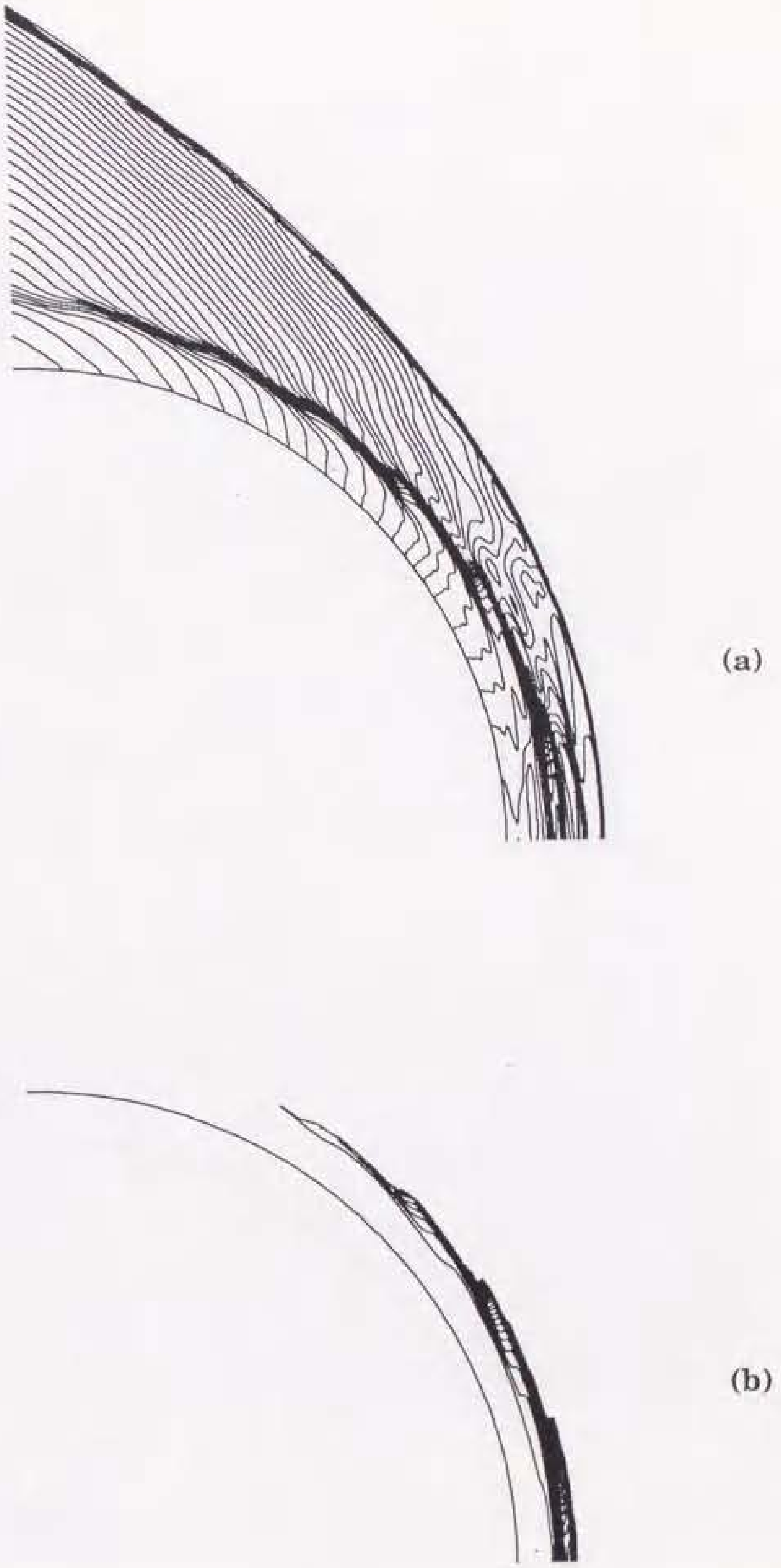

Figure 5.4 Contour plots for the projectile radius $7.5L_*$ with the simplified chemical reaction mechanism: (a) density contour plots, (b) $\rho\omega_8$ contour plots

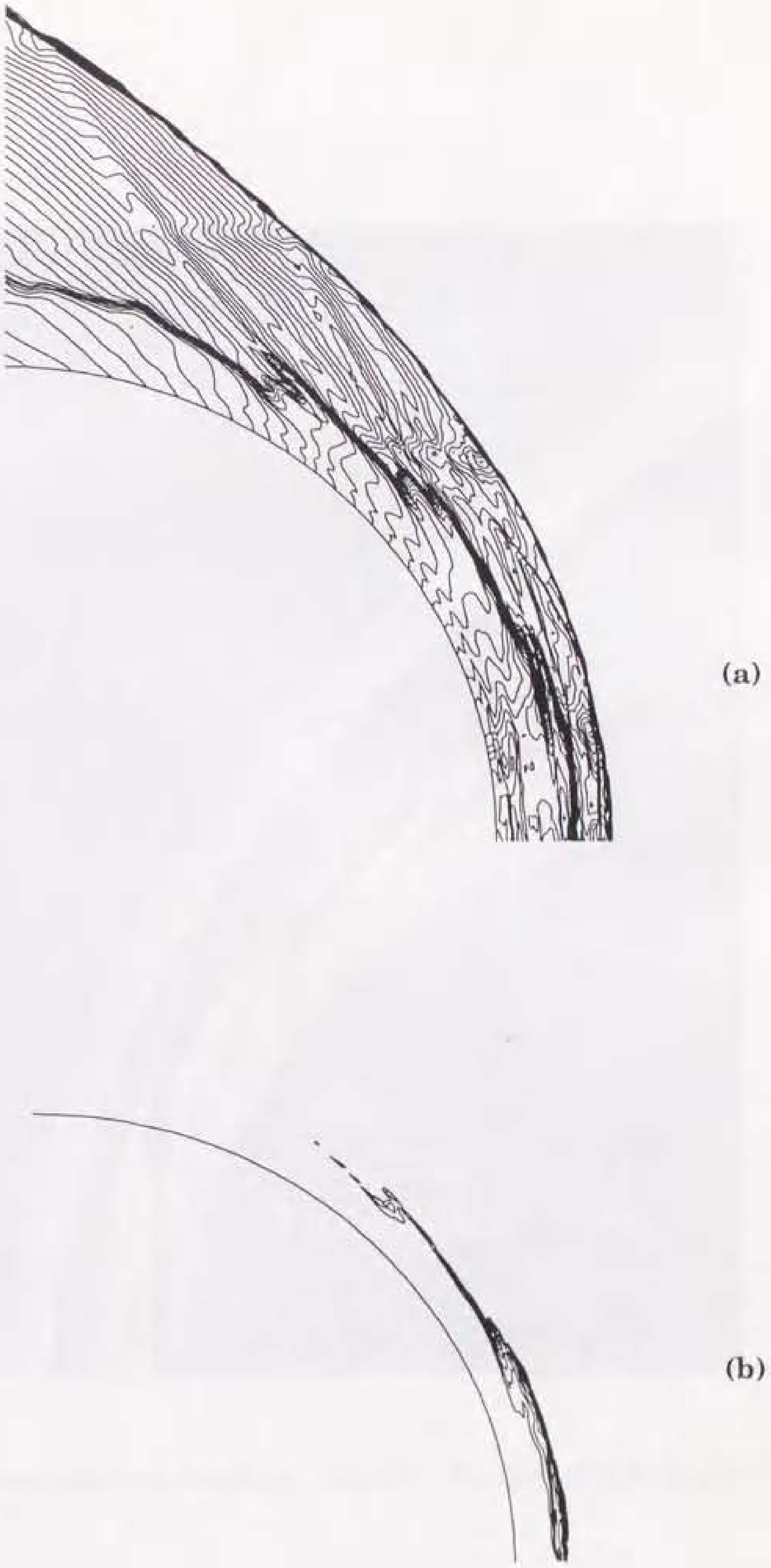

Figure 5.5 Contour plots for the projectile radius $10L\cdot$ with the simplified chemical reaction mechanism: (a) density contour plots, (b) $\rho\omega_{\beta}$ contour plots

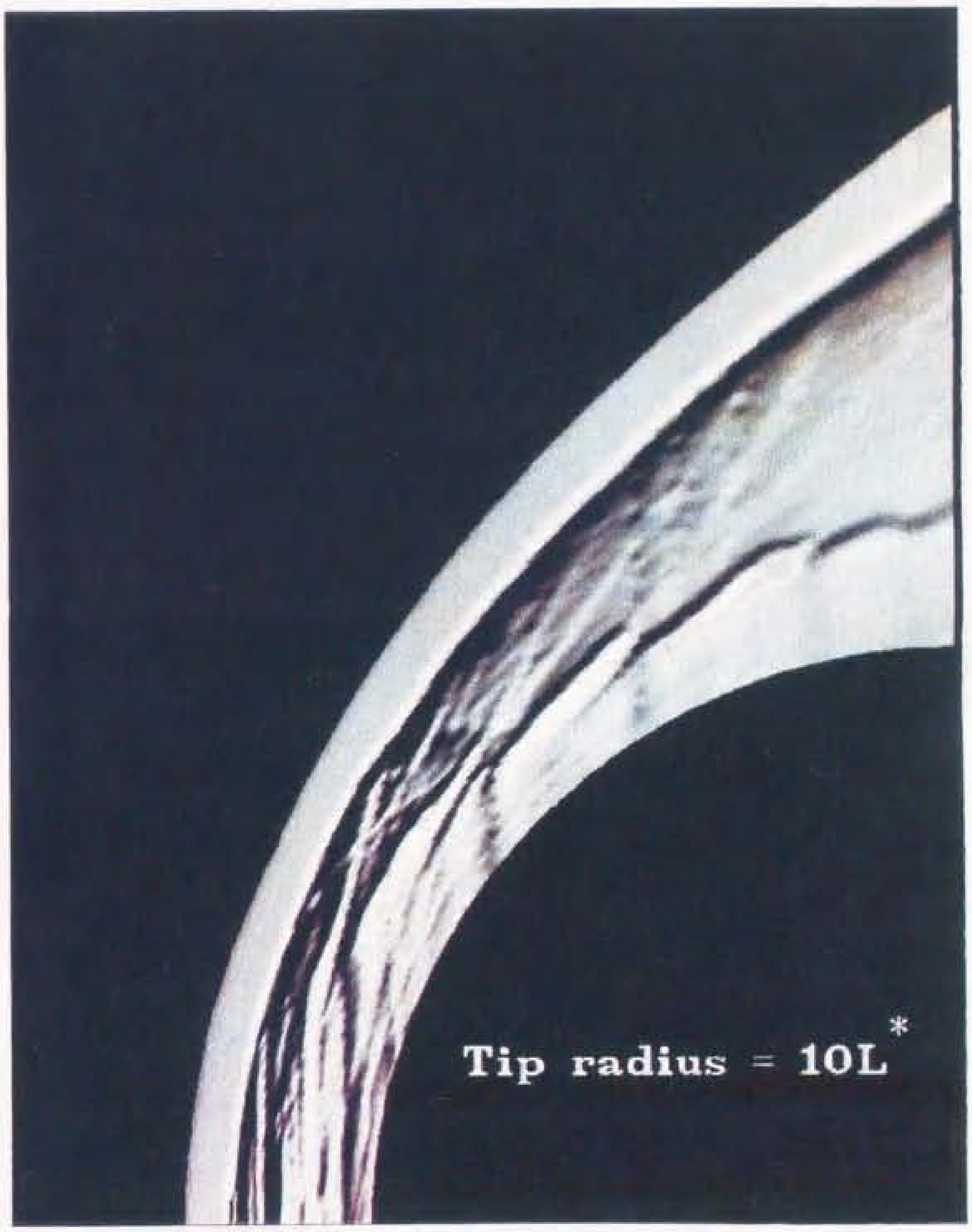

Figure 5.6 Computed shadowgraph image for the projectile radius 10L*

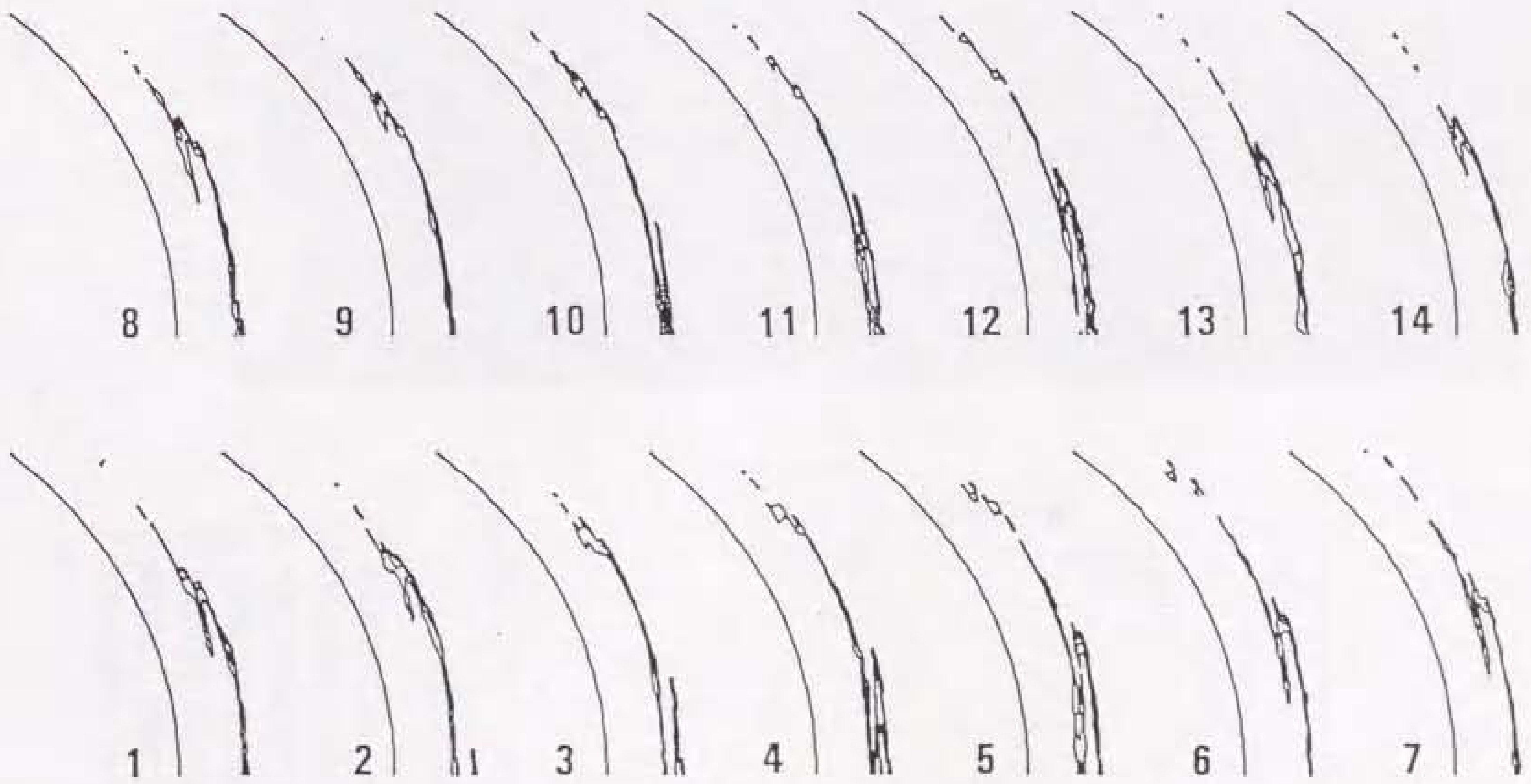

Figure 5.7 Close-up view of the time evolving contour plots of rwb in the nose region of the spherical projectile showing one cycle in the case of projectile radius 10L*

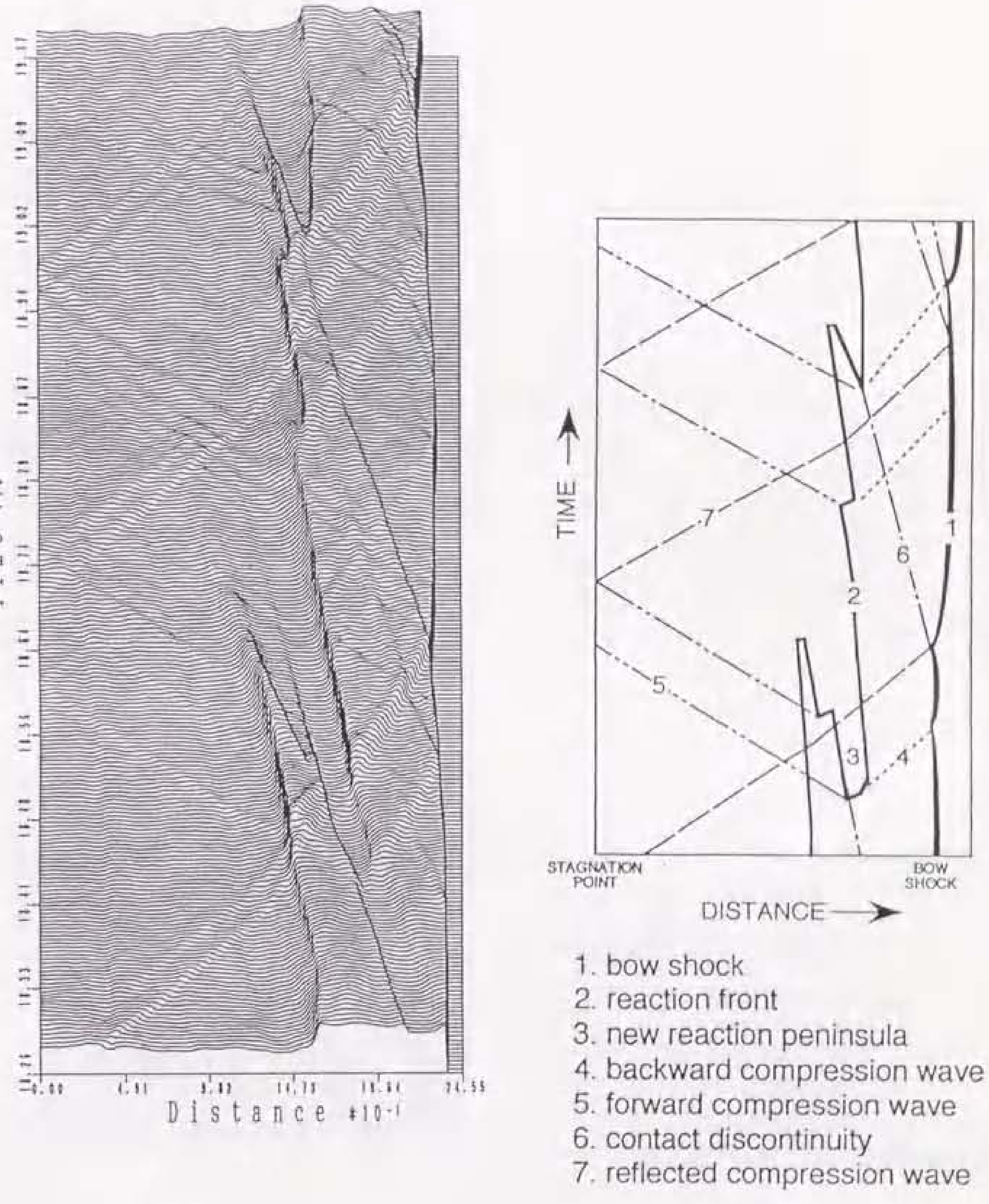

(a) (b)

Figure 5.8 History (x-t diagram) of density between the stagnation point and the bow shock wave on the stagnation streamline for the projectile radius 10L* : (a) level plots, (b) schematic picture

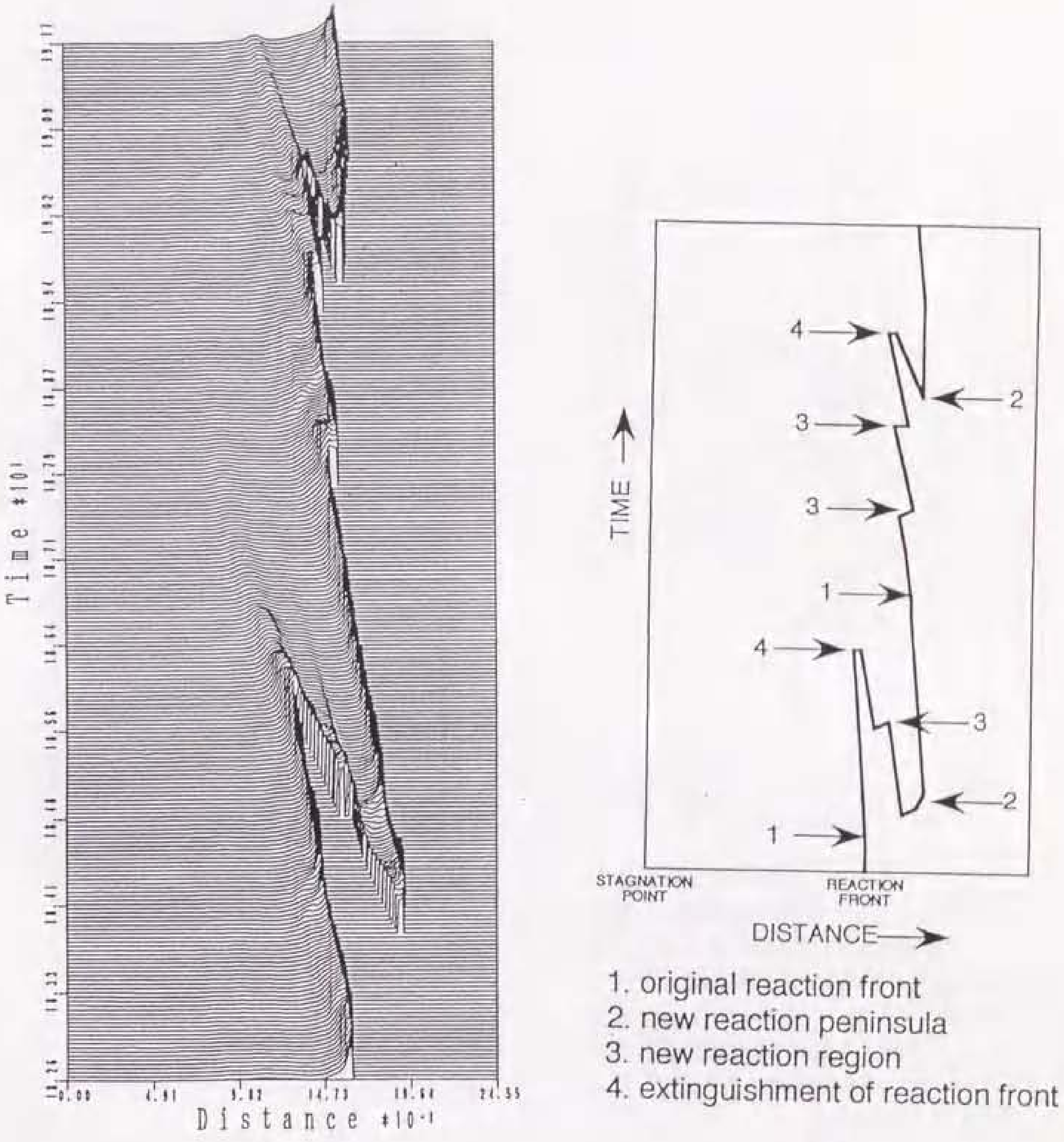

(a)

(b)

Figure 5.9 History (x-t diagram) of $\rho\omega_B$ between the stagnation point and the bow shock wave on the stagnation streamline for the projectile radius 10L* : (a) level plots, (b) schematic picture

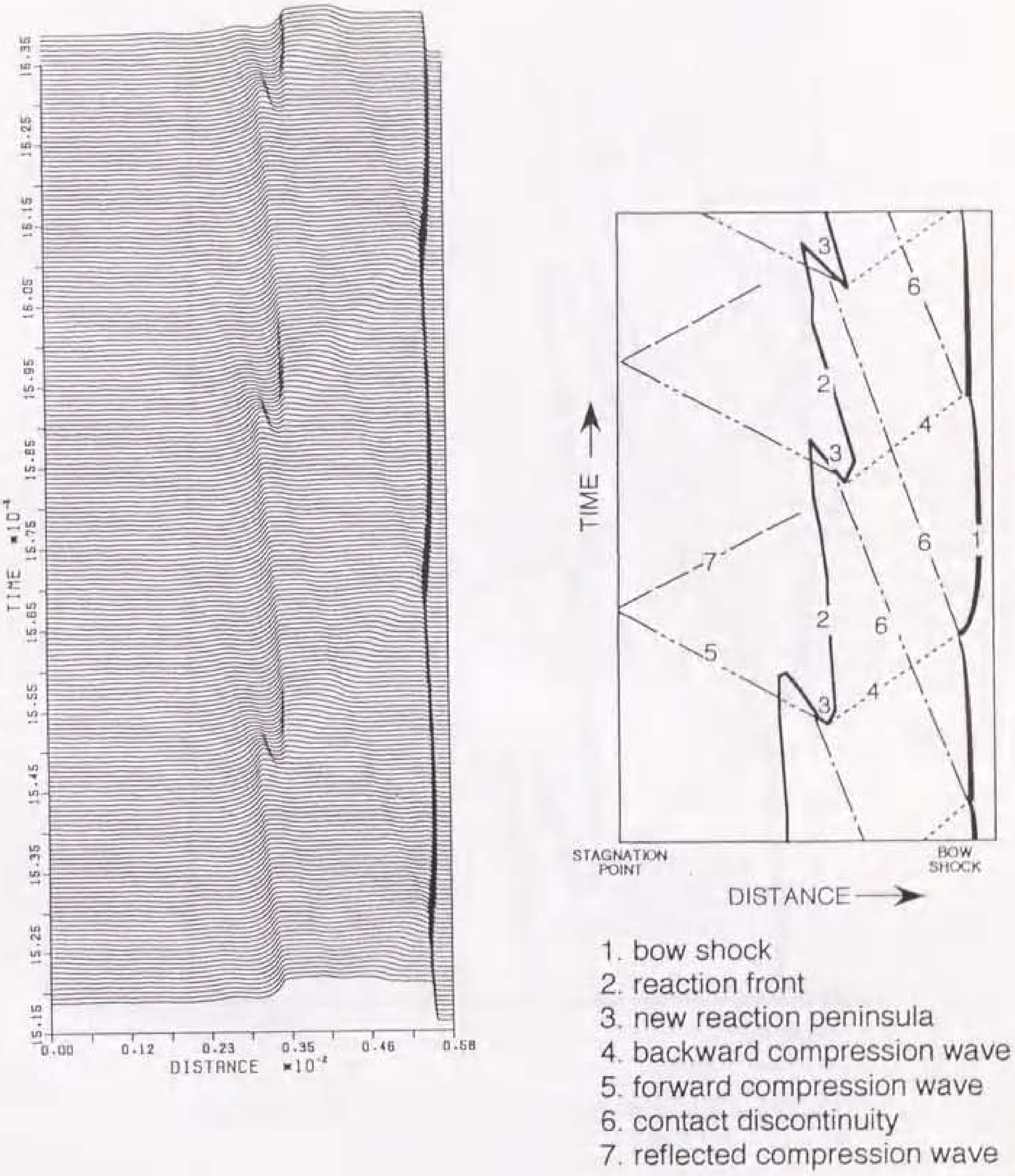

(a) (b)

Figure 5.10 History (x-t diagram) of density between the stagnation point and the bow shock wave on the stagnation streamline for the projectile radius 7.5L* : (a) level plots, (b) schematic picture

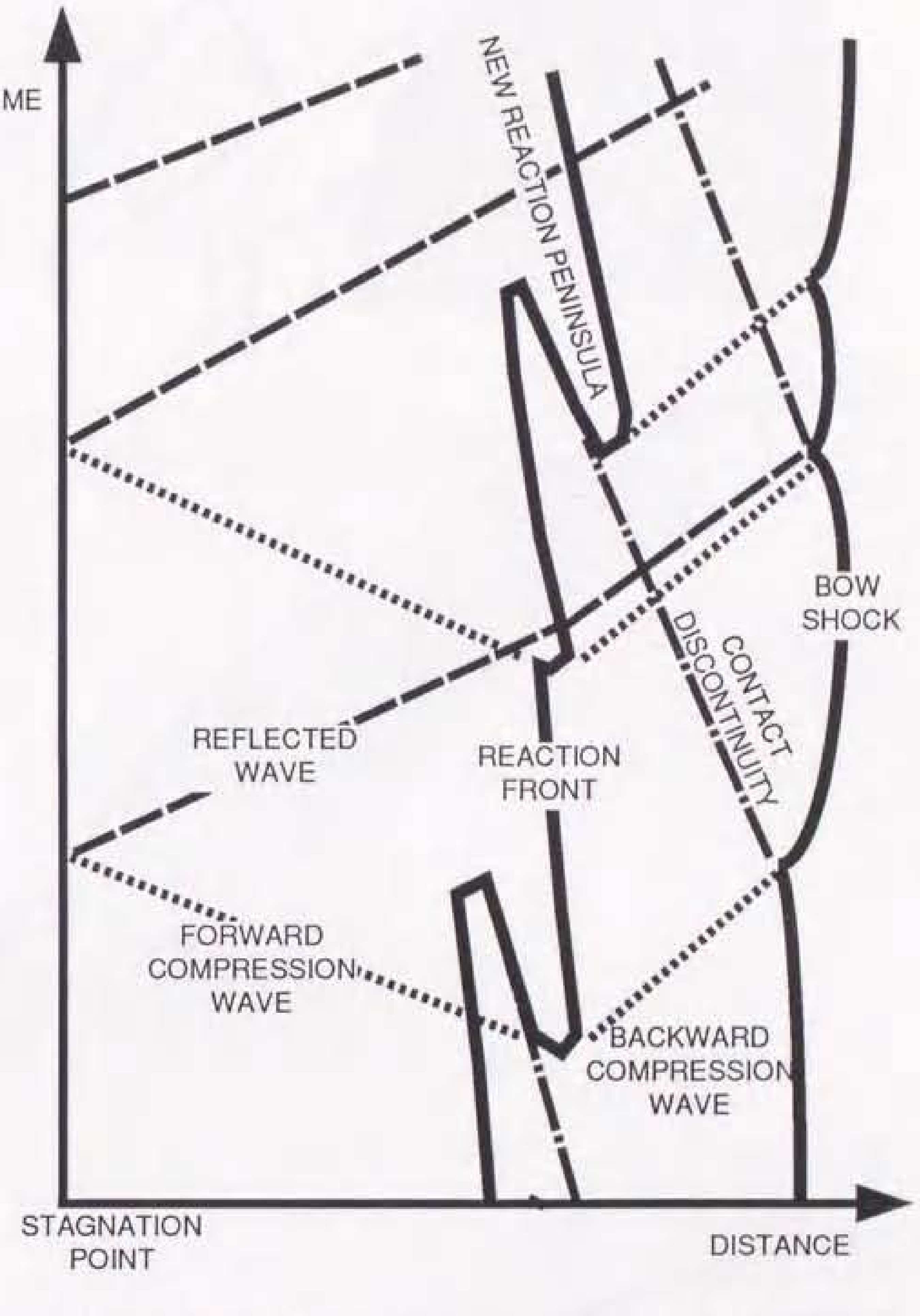

Figure 5.11 X-t diagram of proposed mechanism

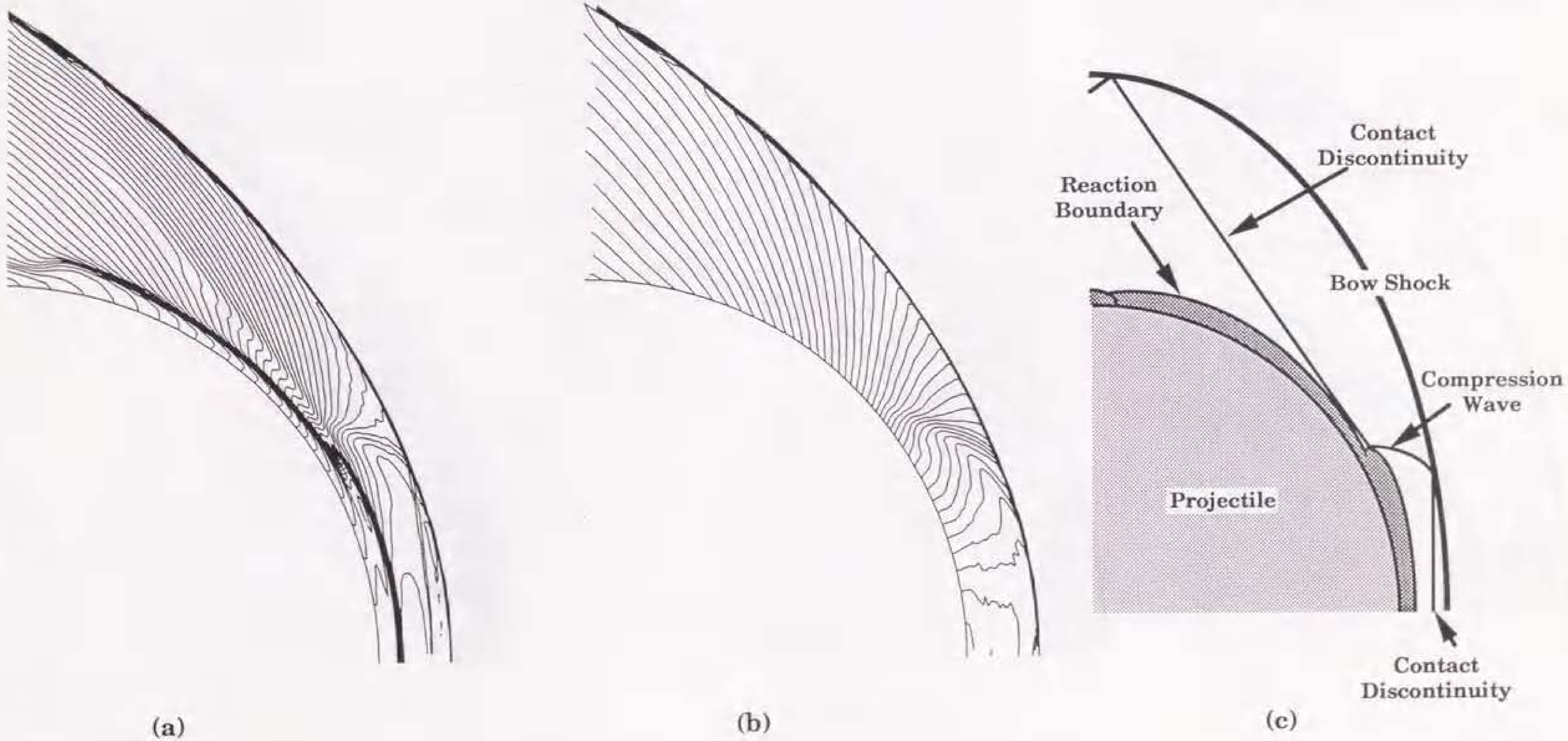

Figure 6.1 Flow fields for the projectile velocity 90% of D:
(a) Density contour plots, (b) Pressure contour plots, (c) Schematic picture of the flow field behind the bow shock

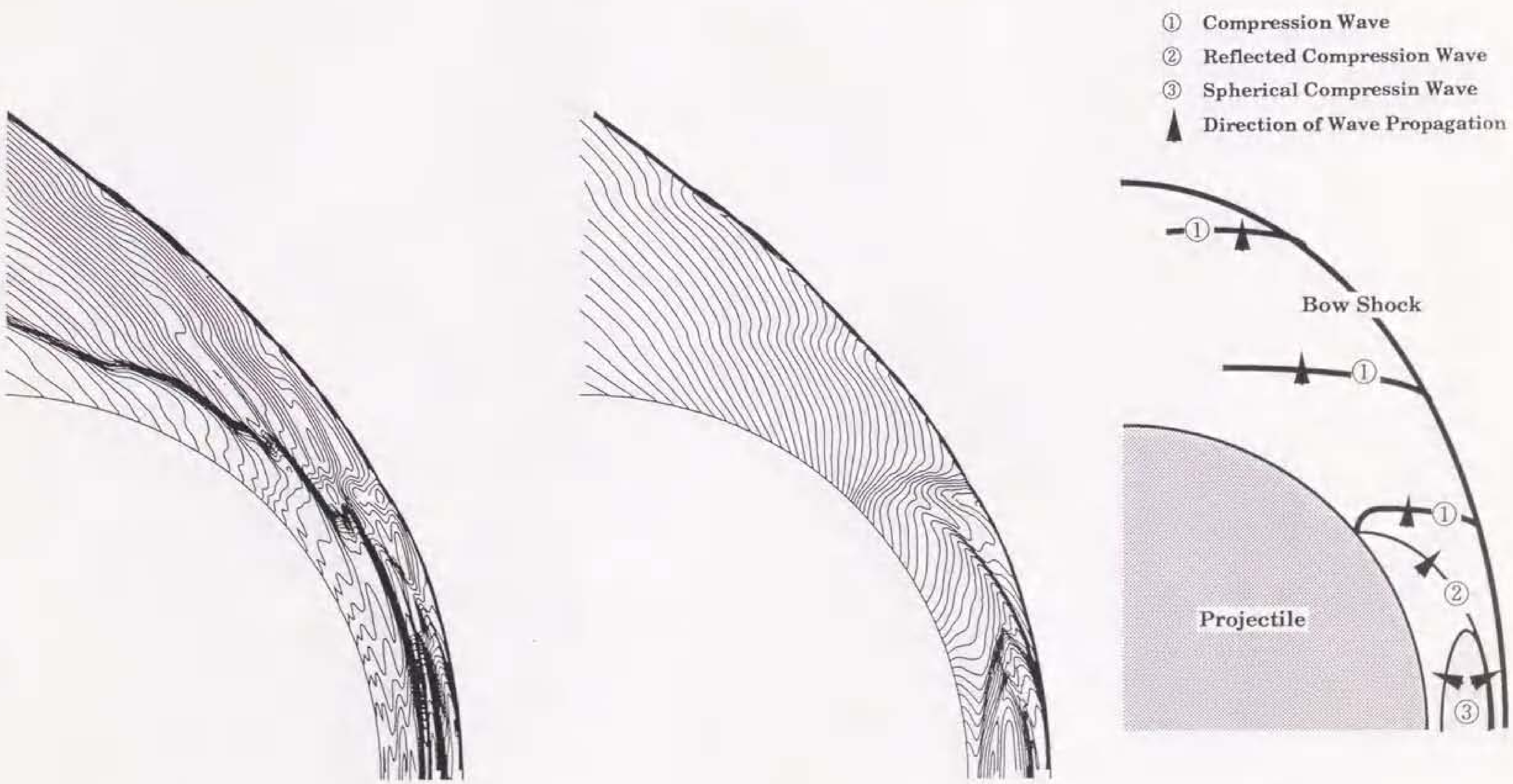

(a) (b) (c)

Figure 6.2 Flow fields for the projectile velocity 100% of D:
(a) Density contour plots, (b) Pressure contour plots, (c) Schematic picture of the pressure flow field behind the bow shock

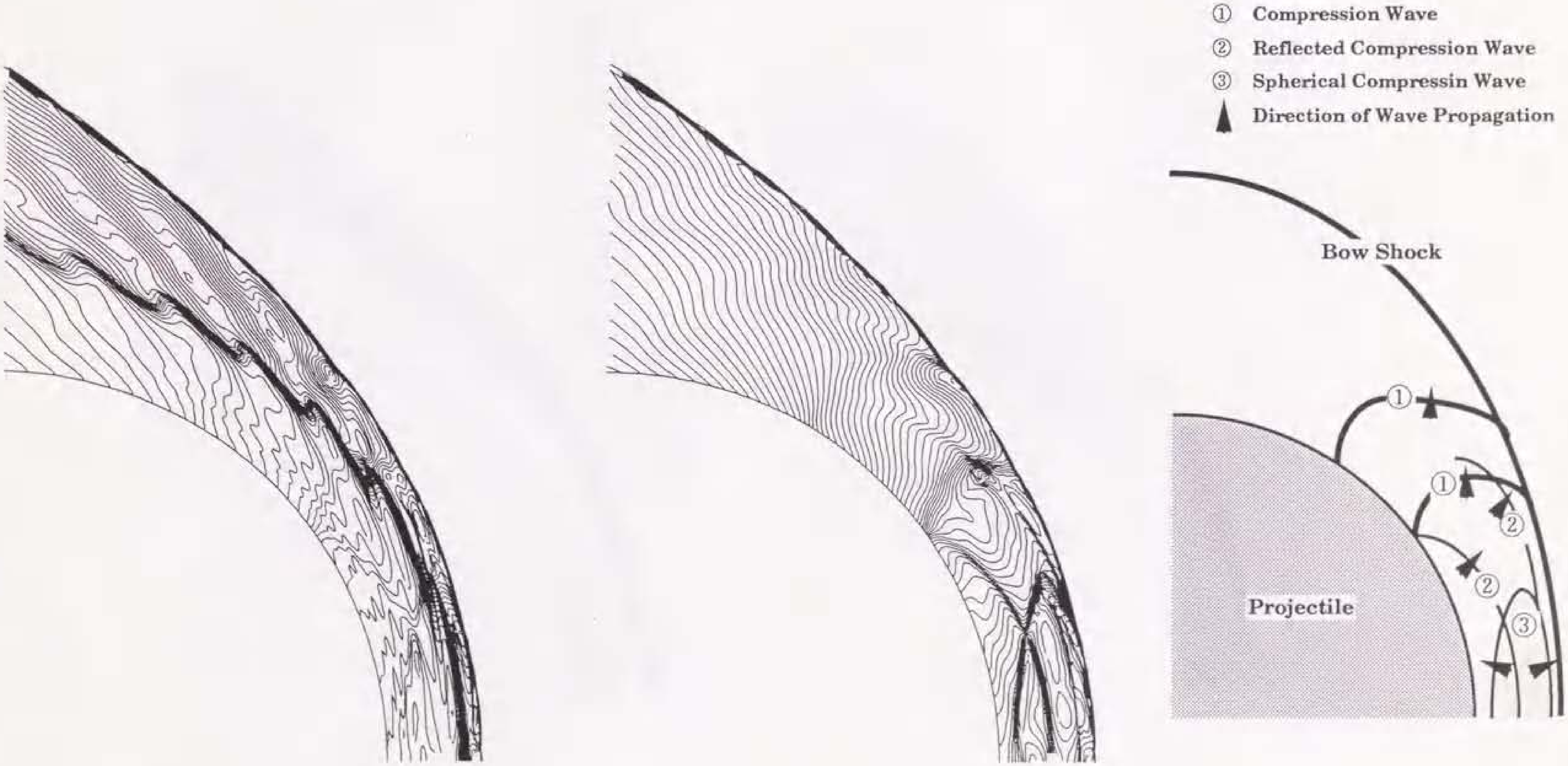

(a) (b) (c)

Figure 6.3 Flow fields for the projectile velocity 110% of D:
(a) Density contour plots, (b) Pressure contour plots, (c) Schematic picture of the pressure flow field behind the bow shock

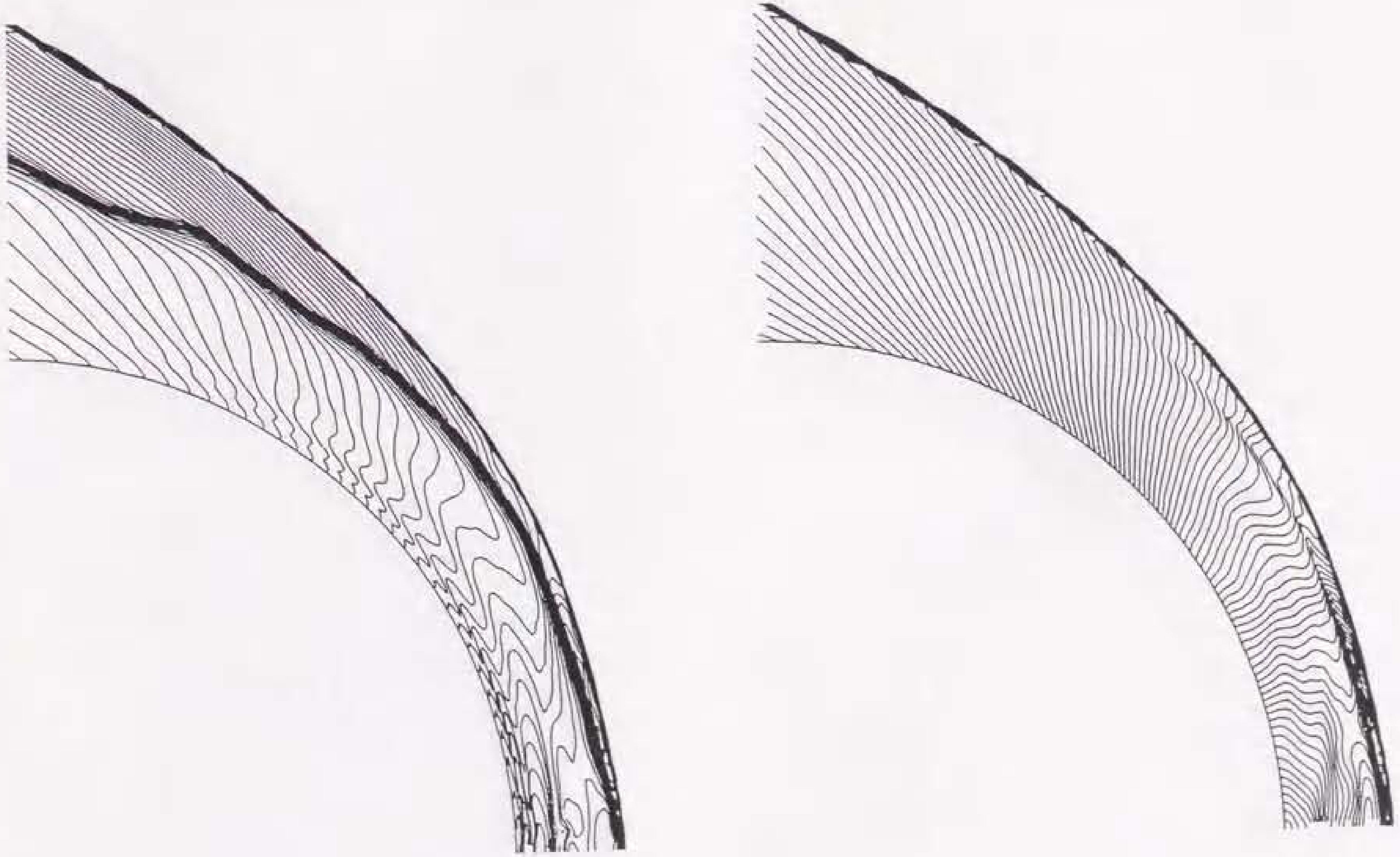

(a) (b)

Figure 6.4 Flow fields for the projectile velocity 120% of D: (a) Density contour plots, (b) Pressure contour plots

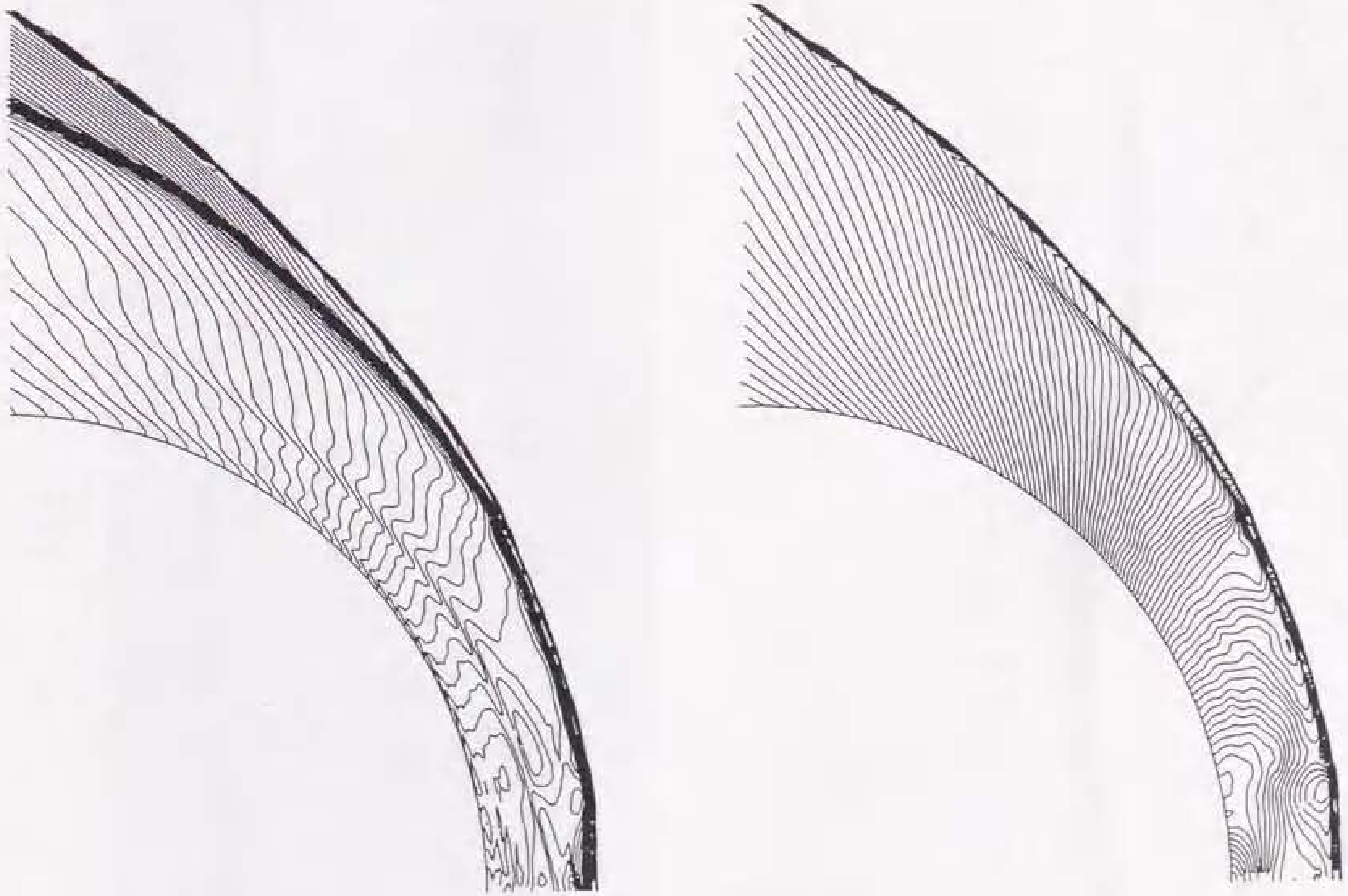

(a)

(b)

Figure 6.5 Flow fields for the projectile velocity 140% of D: (a) Density contour plots, (b) Pressure contour plots

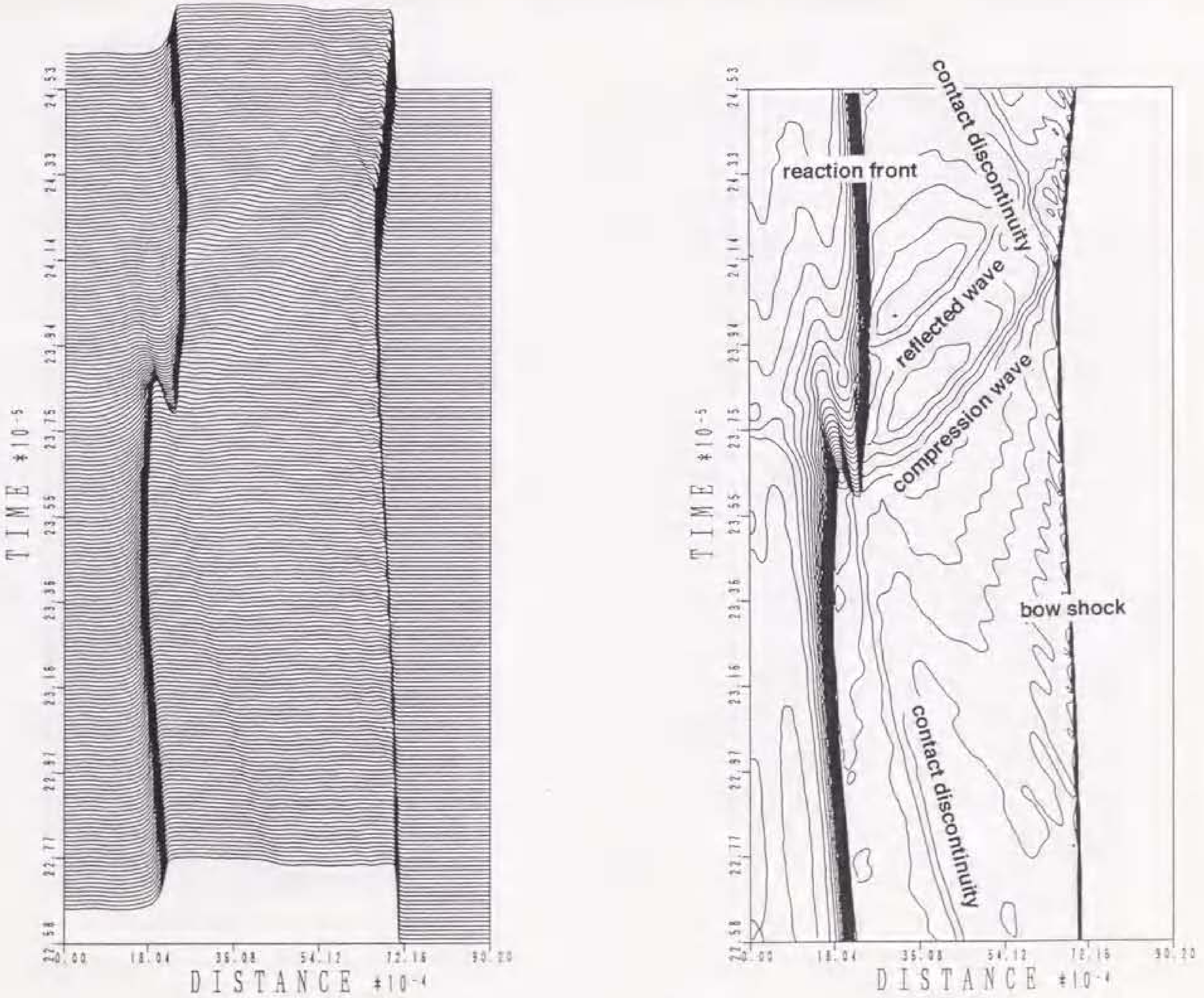

(a) (b)

Figure 6. 6 History (x-t diagram) of density between the stagnation point and the bow shock wave on the stagnation streamline for the projectile velocity 90% of D: (a) level plots, (b) contour plots

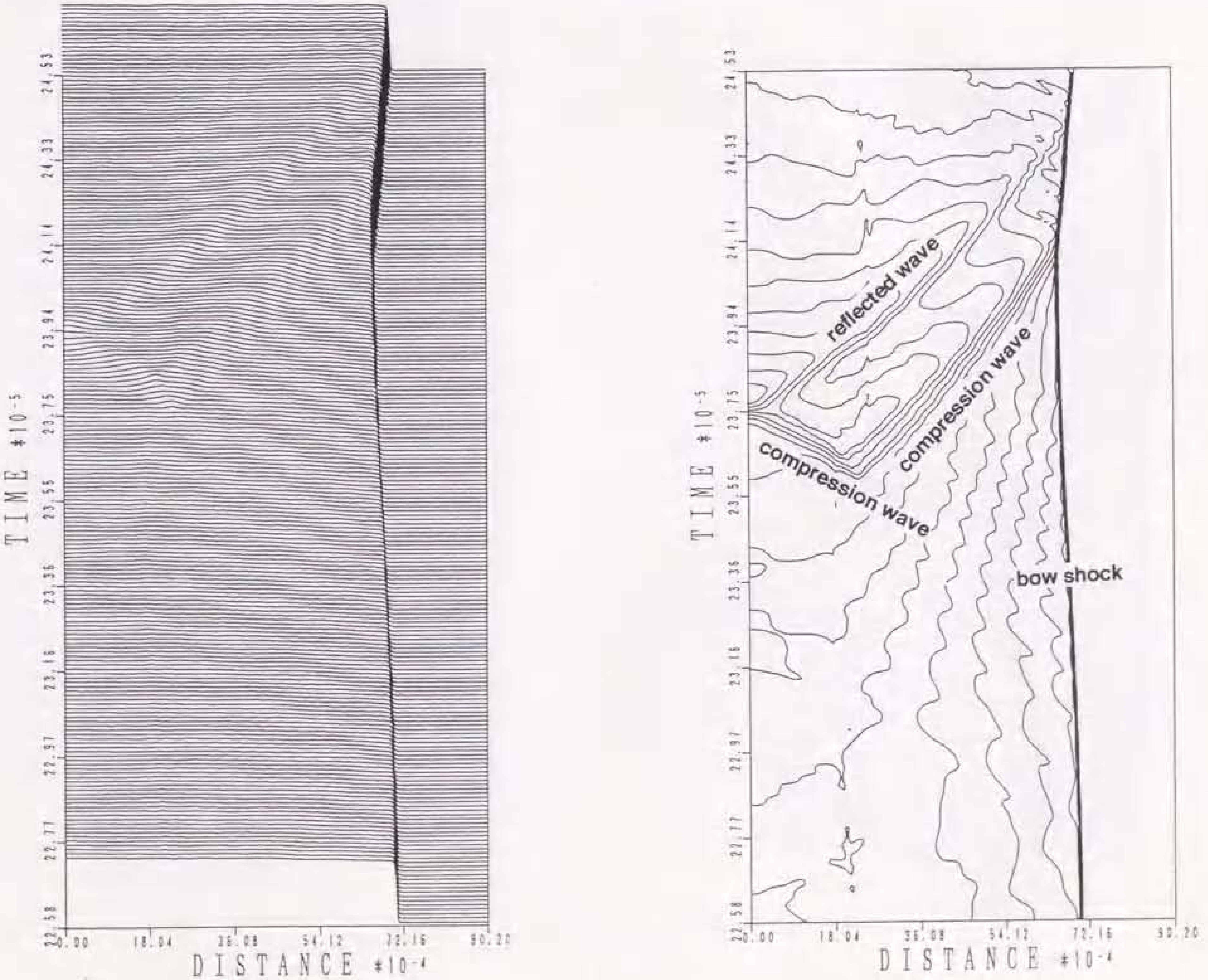

(a) (b)

Figure 6. 7 History (x-t diagram) of pressure between the stagnation point and the bow shock wave on the stagnation streamline for the projectile velocity 90% of D: (a) level plots, (b) contour plots

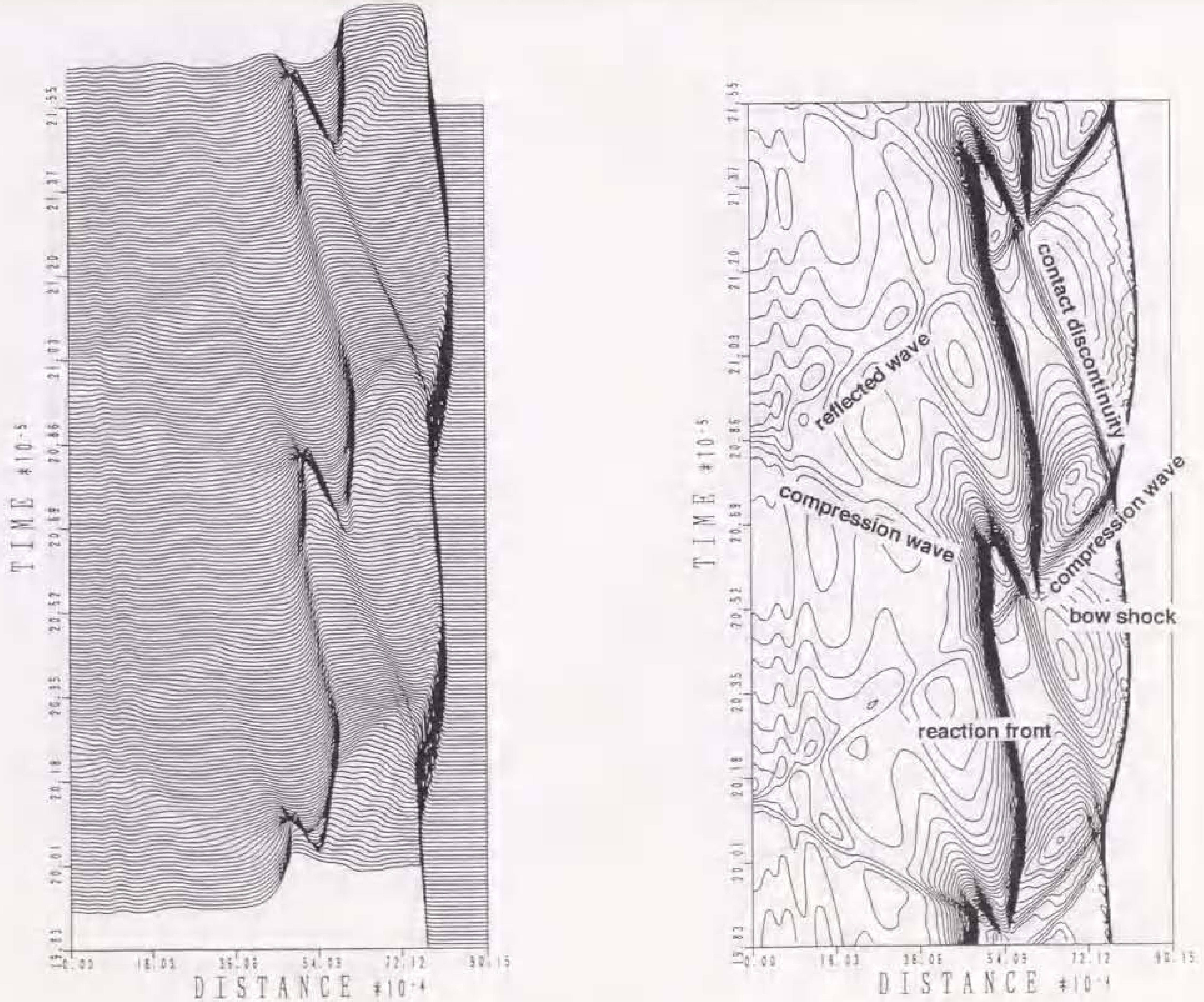

(a)

(b)

Figure 6. 8 History (x-t diagram) of density between the stagnation point and the bow shock wave on the stagnation streamline for the projectile velocity 100 of D: (a) level plots, (b) contour plots

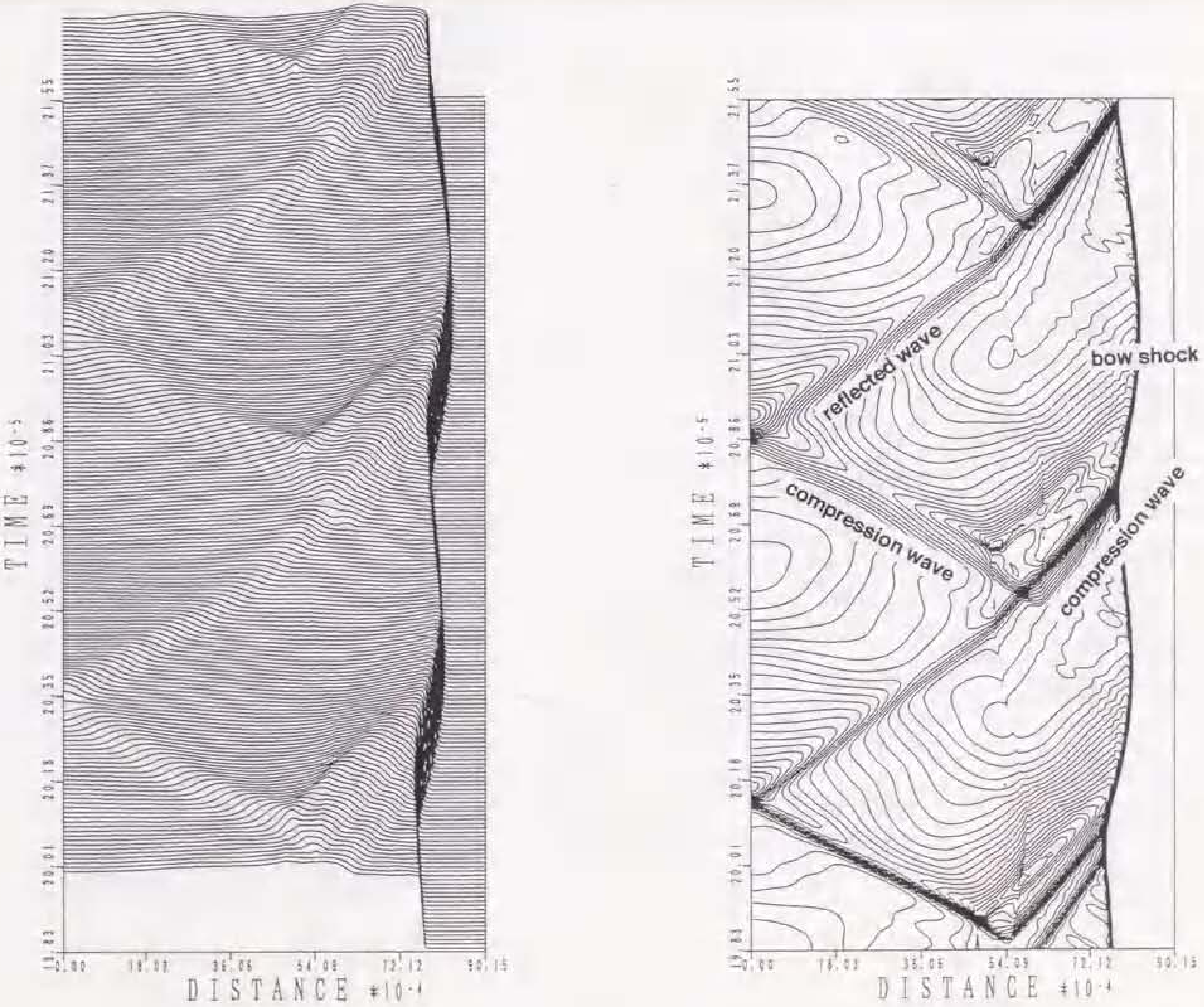

(a)

(b)

Figure 6. 9 History (x-t diagram) of pressure between the stagnation point and the bow shock wave on the stagnation streamline for the projectile velocity 100 of D: (a) level plots, (b) contour plots

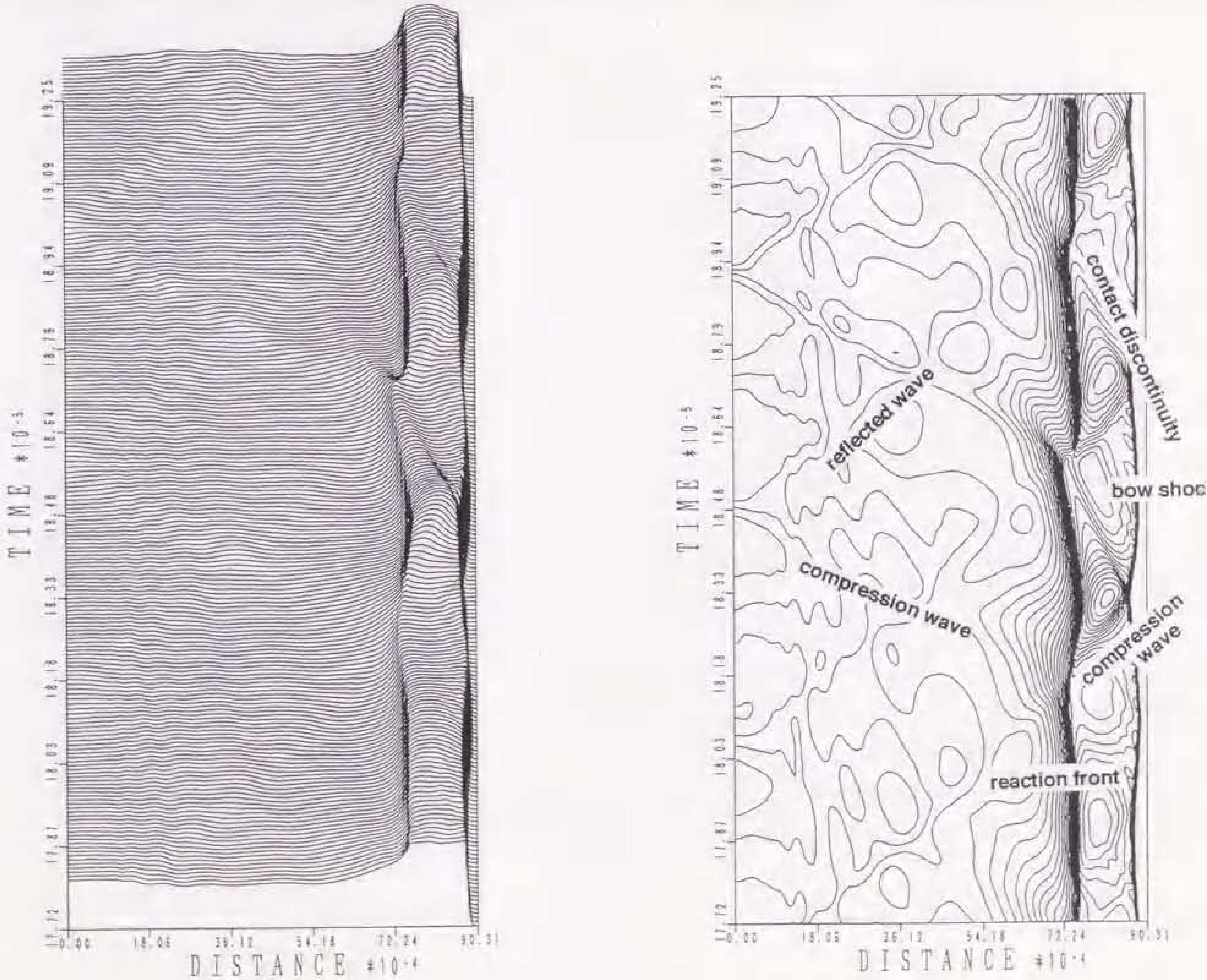

(a)

(b)

Figure 6. 10 History (x-t diagram) of density between the stagnation point and the bow shock wave on the stagnation streamline for the projectile velocity 110 of D: (a) level plots, (b) contour plots

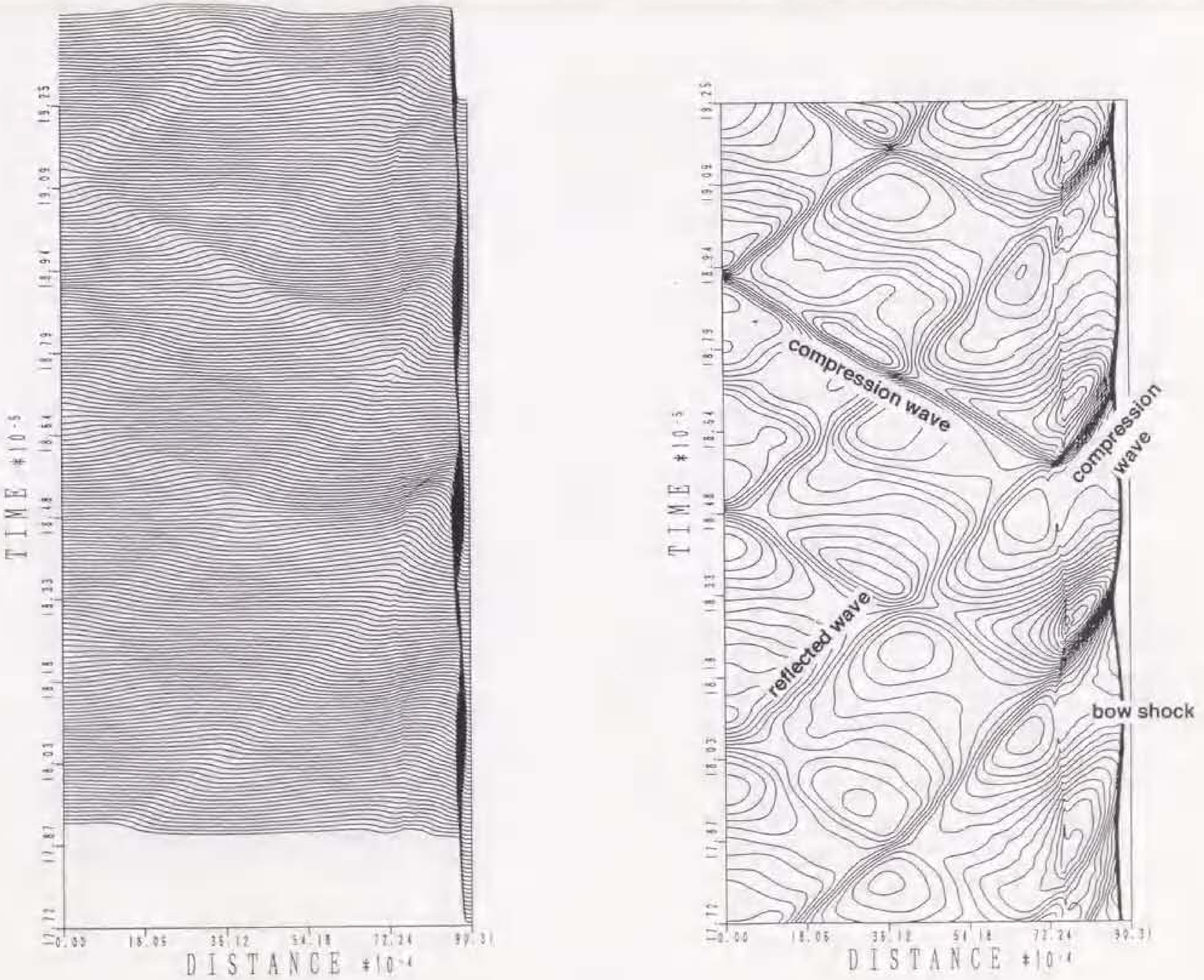

(a)

(b)

Figure 6. 11 History (x-t diagram) of pressure between the stagnation point and the bow shock wave on the stagnation streamline for the projectile velocity 110 of D: (a) level plots, (b) contour plots

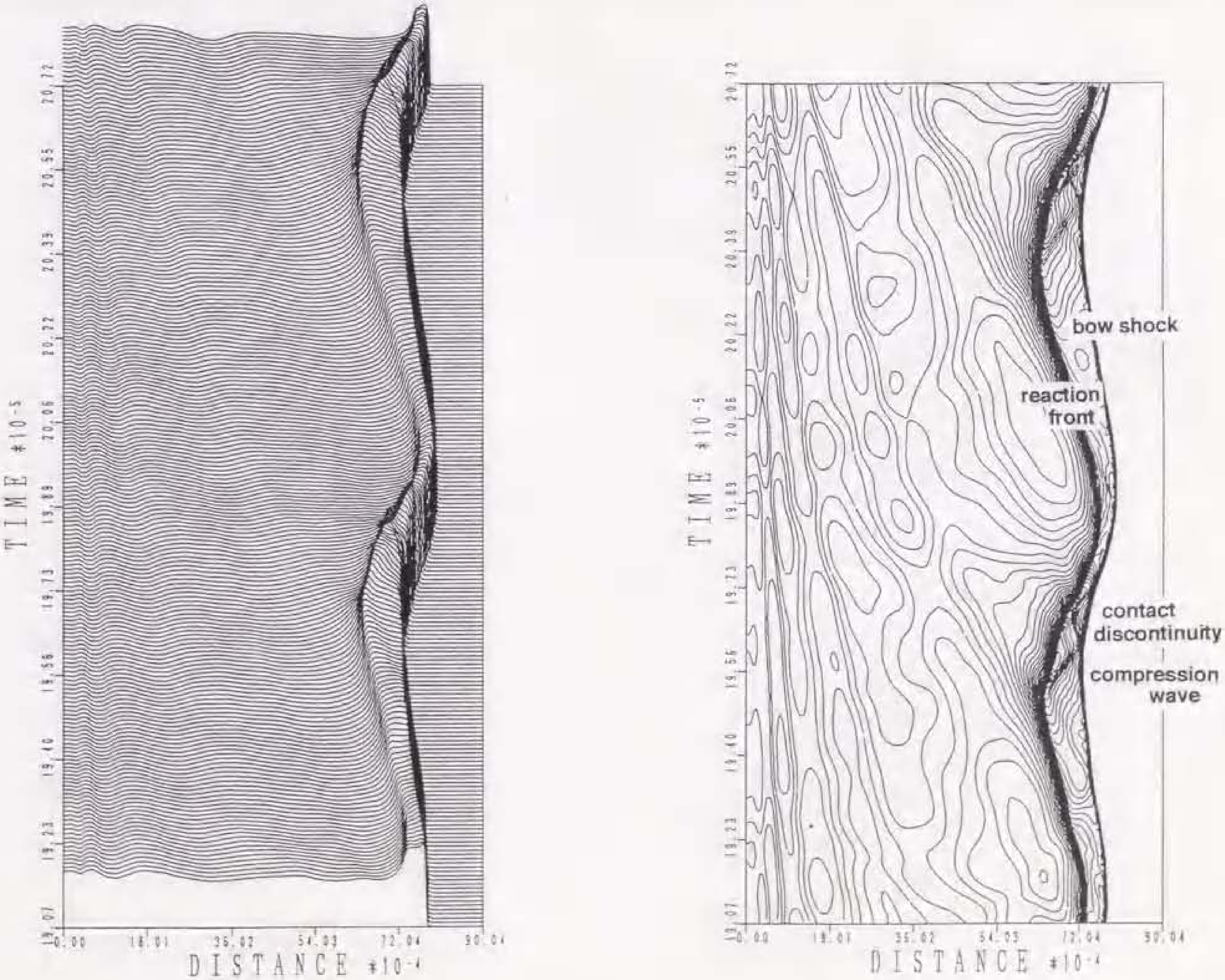

(a)

(b)

Figure 6. 12 History (x-t diagram) of density between the stagnation point and the bow shock wave on the stagnation streamline for the projectile velocity 120 of D: (a) level plots, (b) contour plots

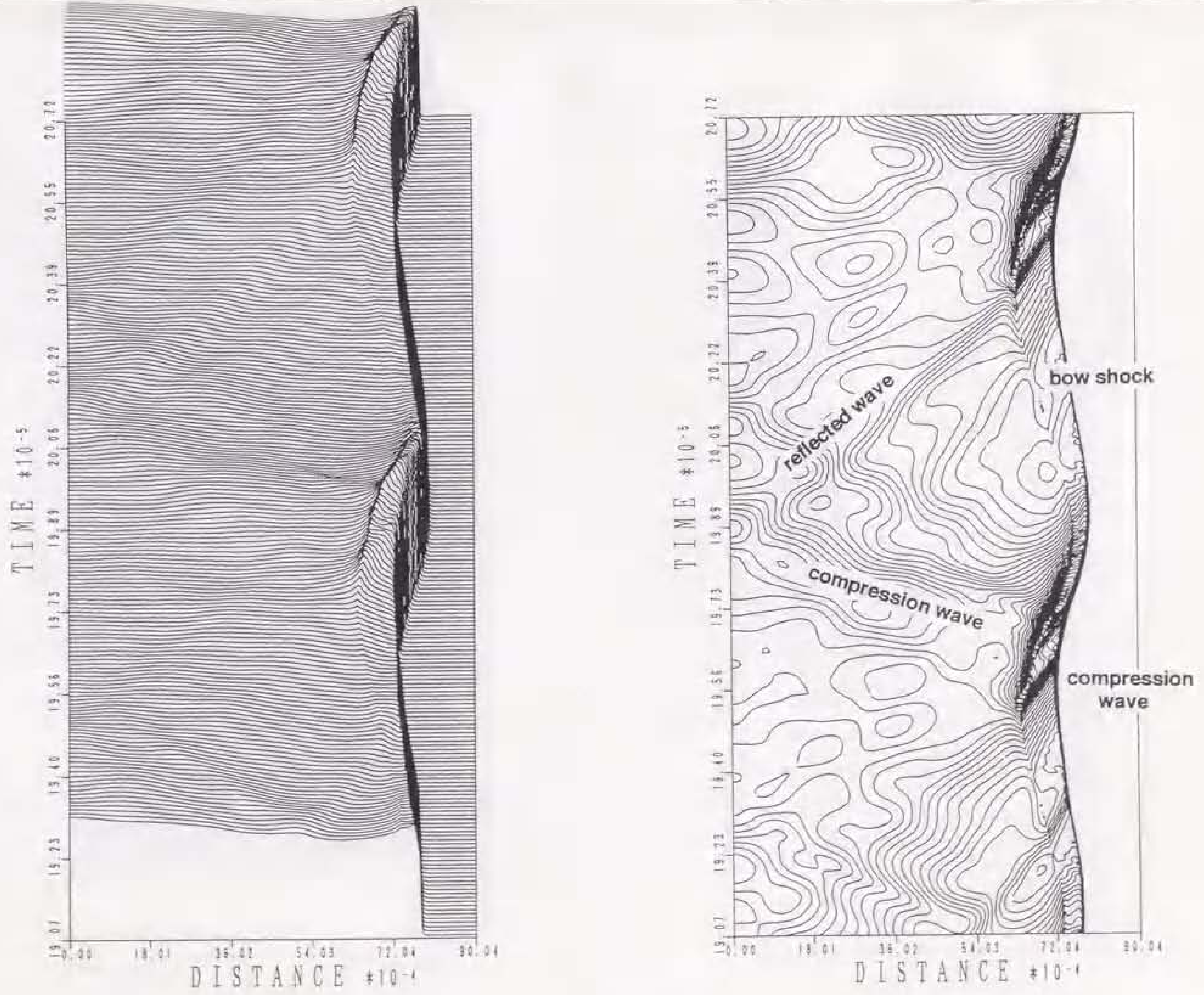

(a)

(b)

Figure 6. 13 History (x-t diagram) of pressure between the stagnation point and the bow shock wave on the stagnation streamline for the projectile velocity 120 of D: (a) level plots, (b) contour plots

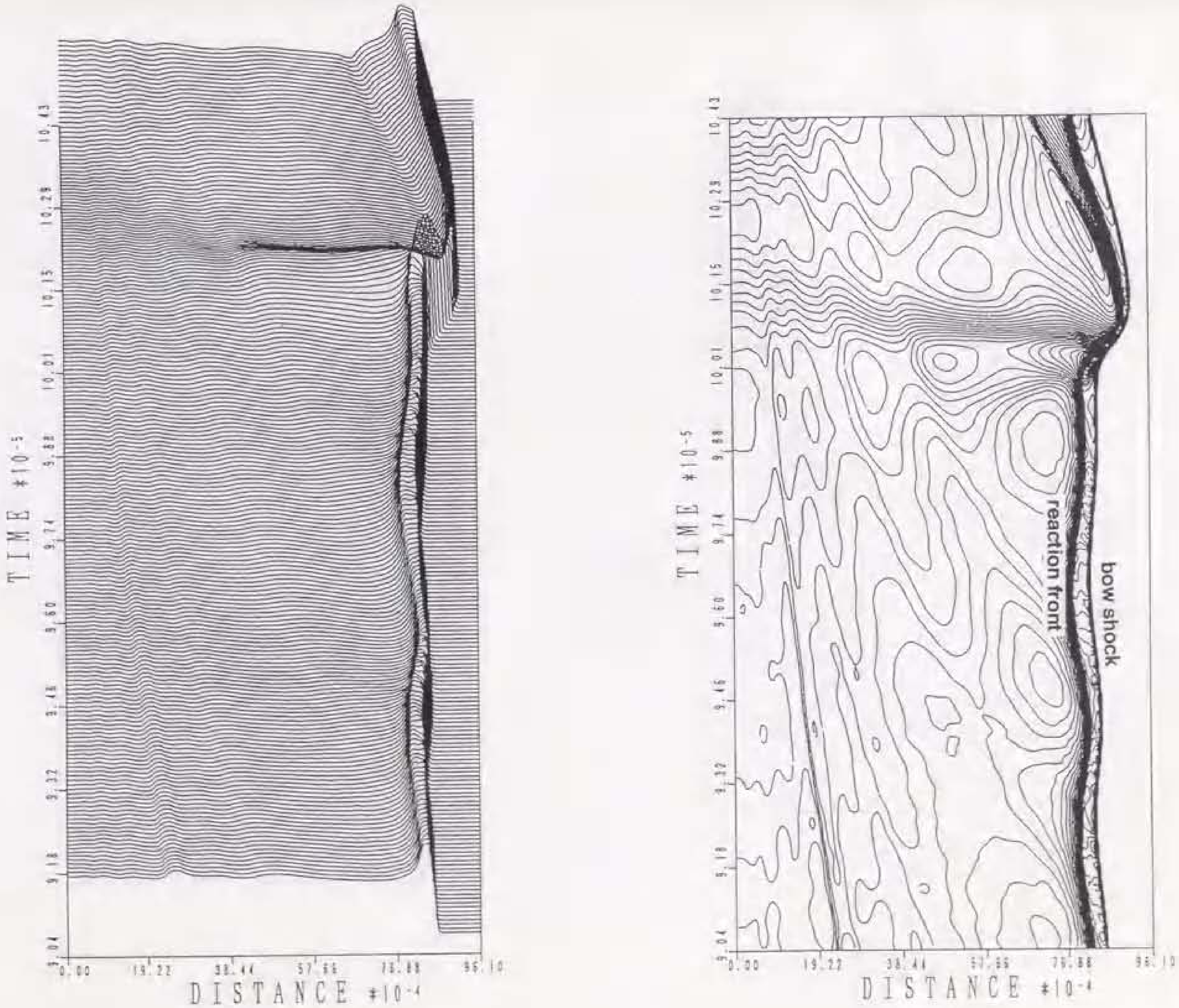

(a)

(b)

Figure 6. 14 History (x-t diagram) of density between the stagnation point and the bow shock wave on the stagnation streamline for the projectile velocity 140 of D: (a) level plots, (b) contour plots

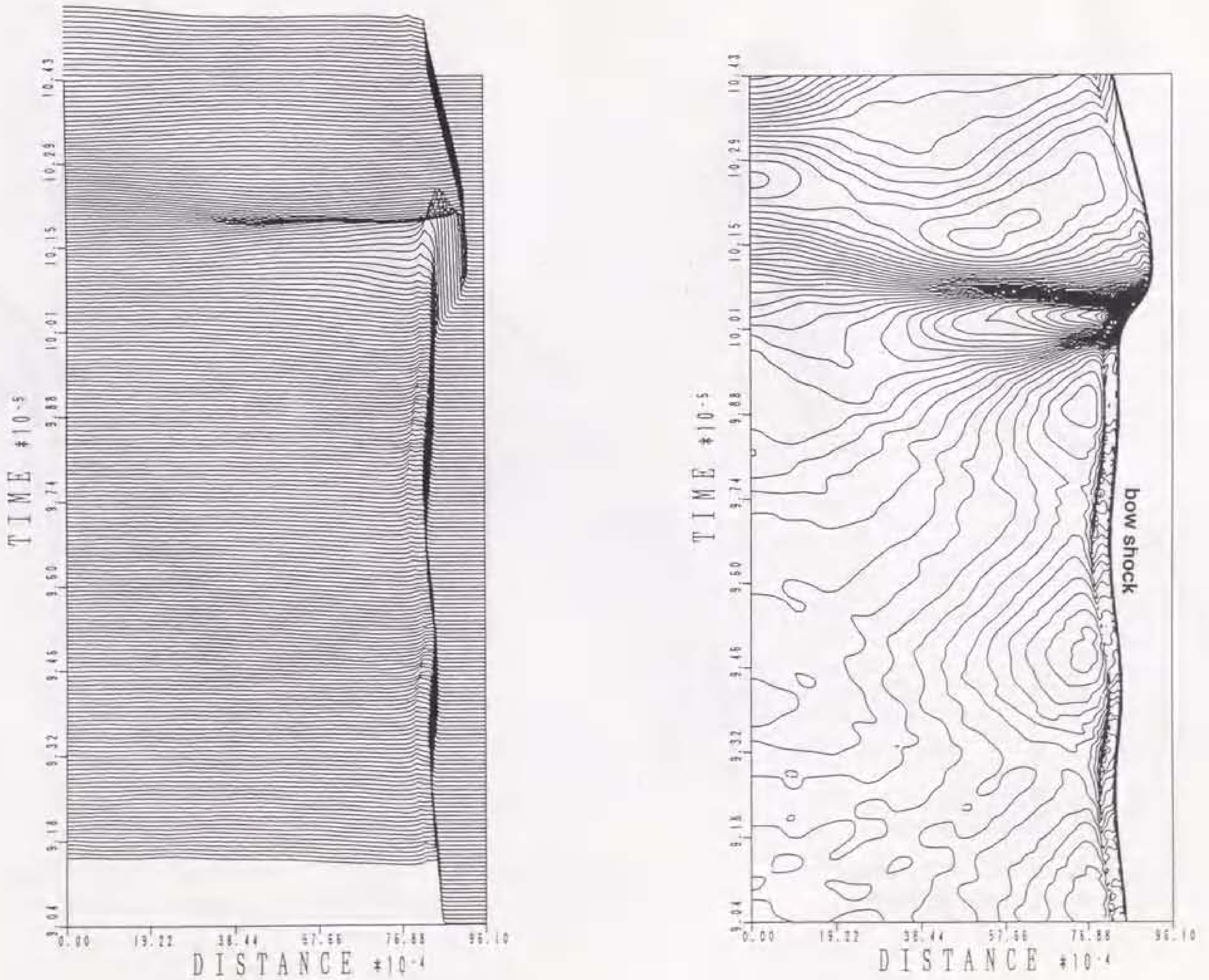

(a)

(b)

Figure 6. 15 History (x-t diagram) of pressure between the stagnation point and the bow shock wave on the stagnation streamline for the projectile velocity 140 of D: (a) level plots, (b) contour plots

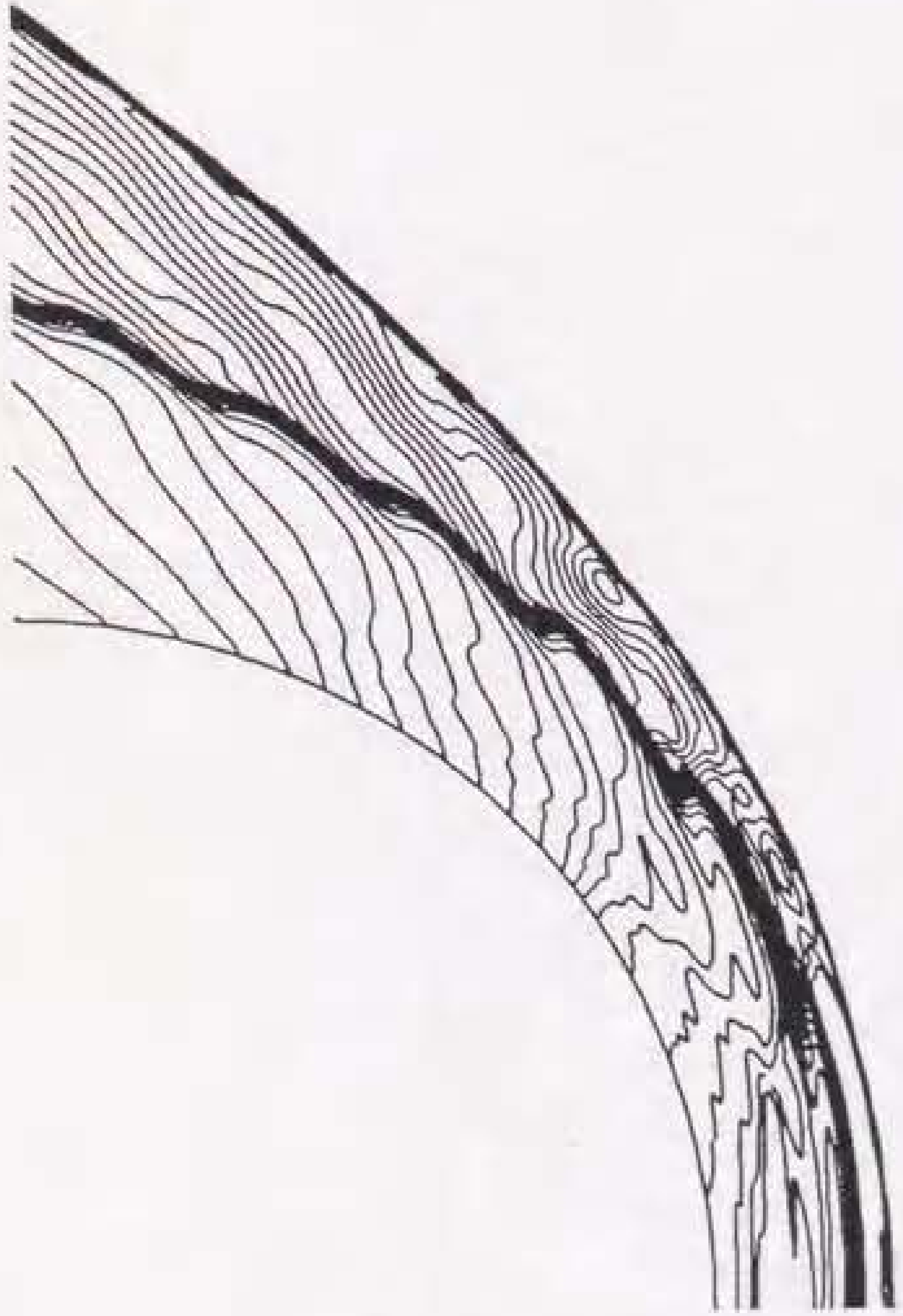

Figure 7. 1 Density contour plots for the projectile velocity 1,931 m/sec

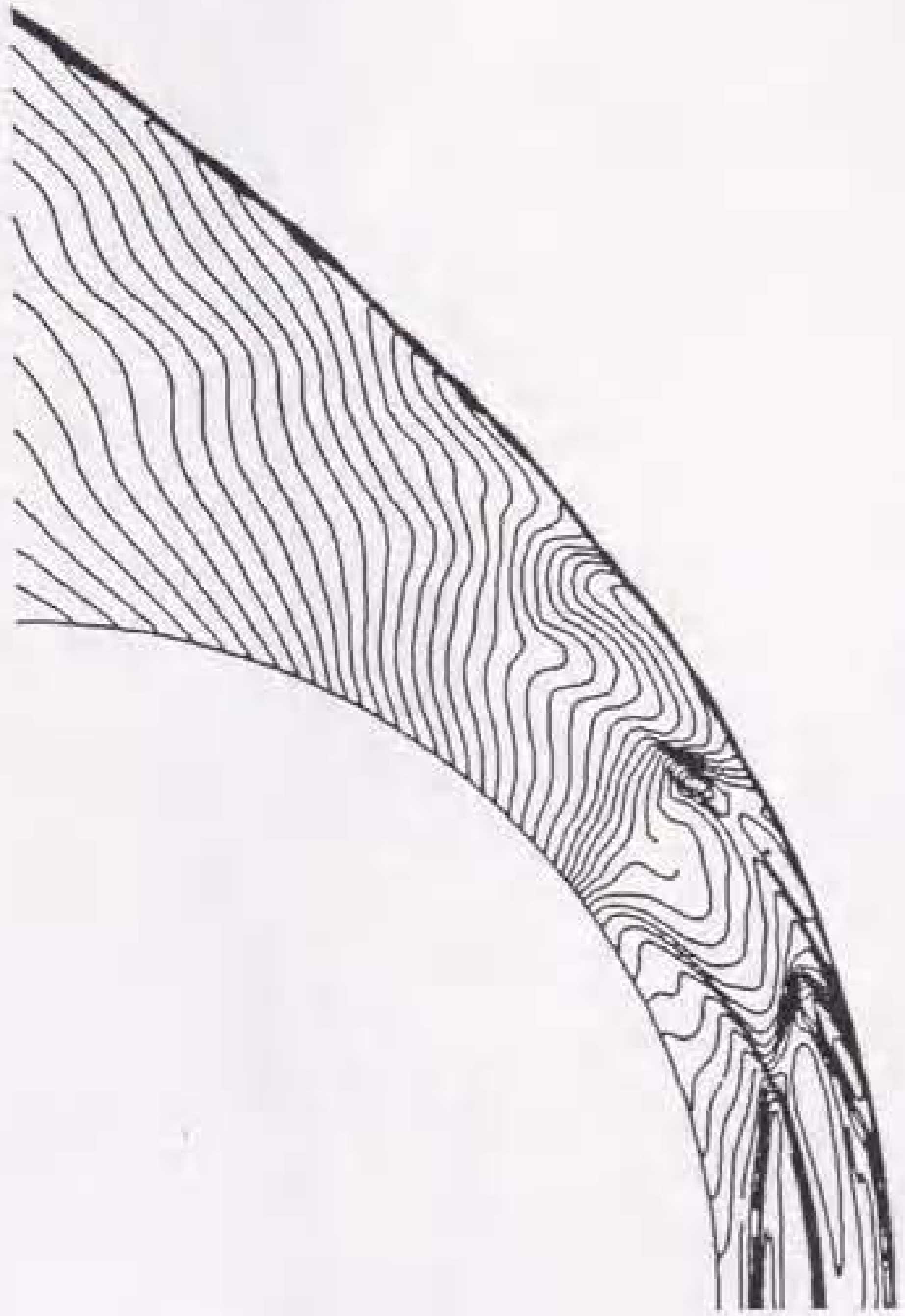

Figure 7. 2 Pressure contour plots for the projectile velocity 1,931 m/sec

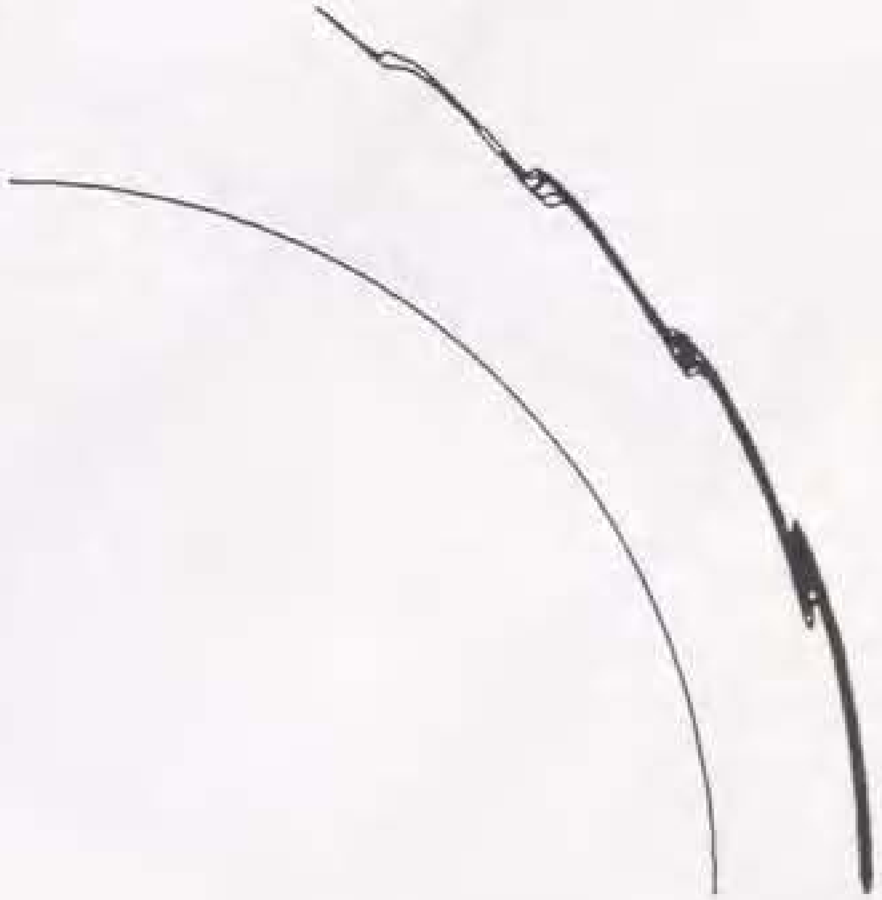

Figure 7. 3 Contour plots of source term of the water for the projectile velocity 1,931 m/sec

(a) (b)

Figure 7. 4 History (x-t diagram) of flow fields between the stagnation point and the bow shock wave on the stagnation streamline for the projectile velocity 1,931 m/sec: (a) density, (b) pressure

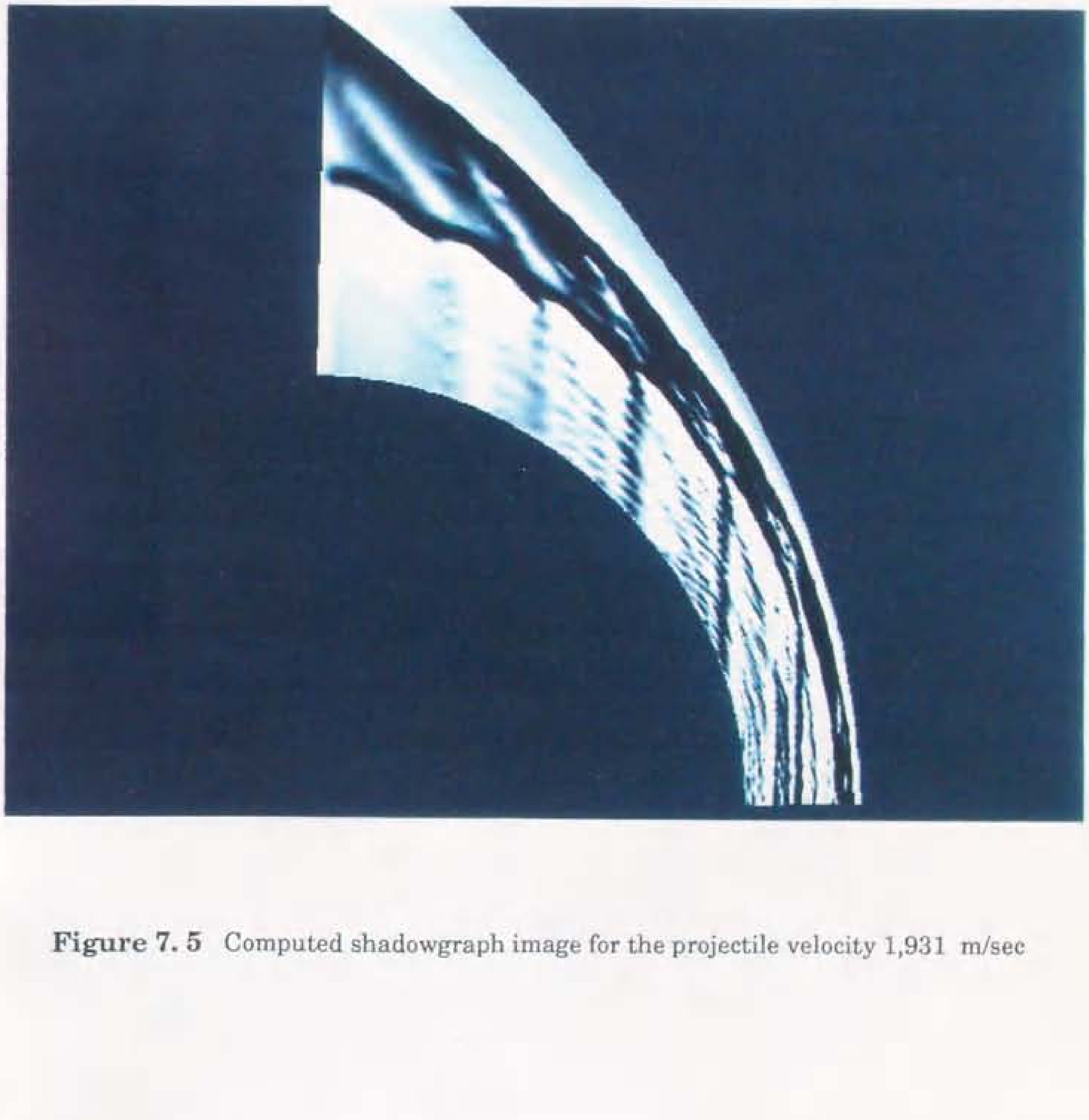

Figure 7. 5 Computed shadowgraph image for the projectile velocity 1,931 m/sec

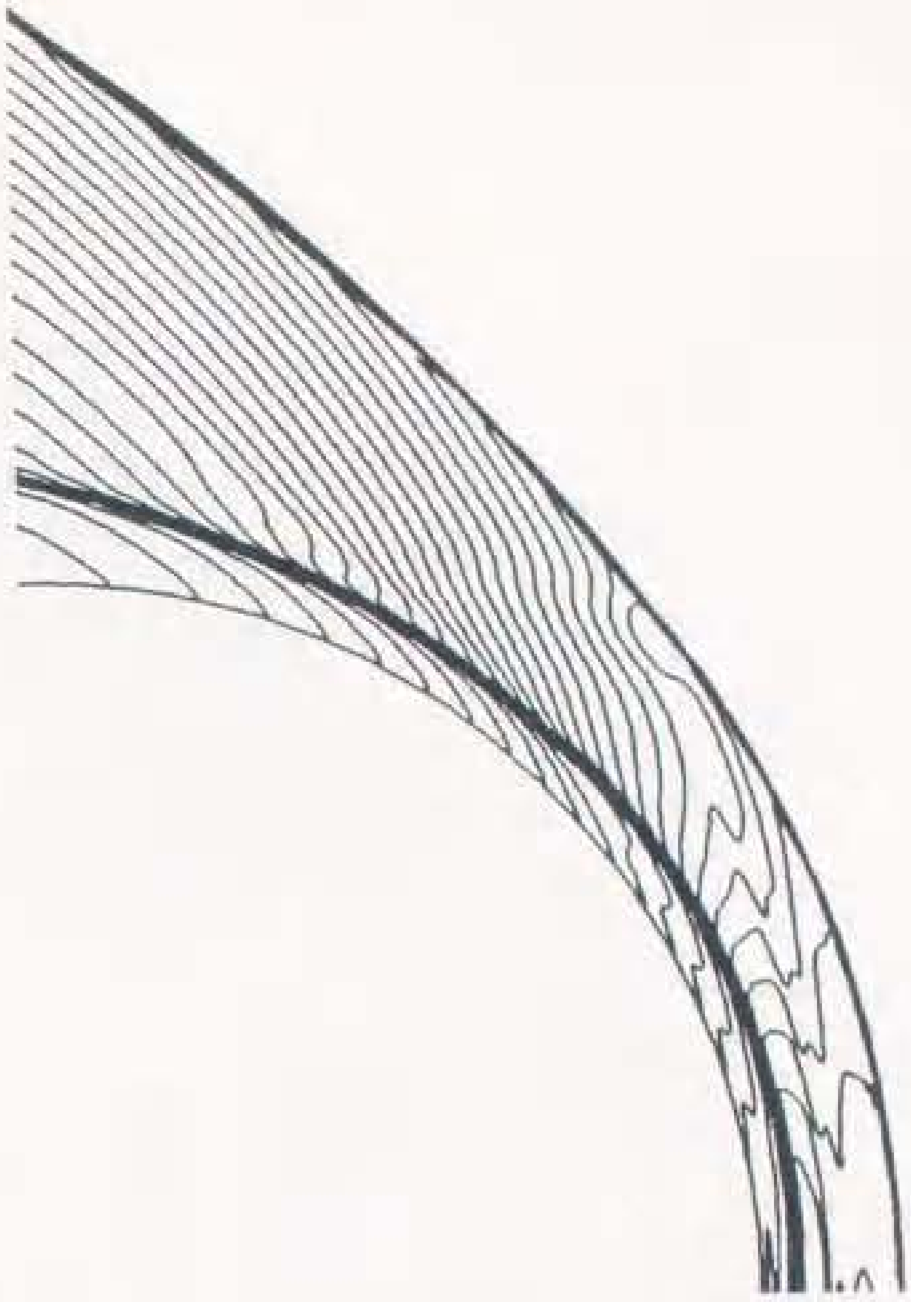

Figure 7. 6 Density contour plots for the projectile velocity 1,685 m/sec

Figure 7. 7 Density gradient for the projectile velocity 1,685 m/sec

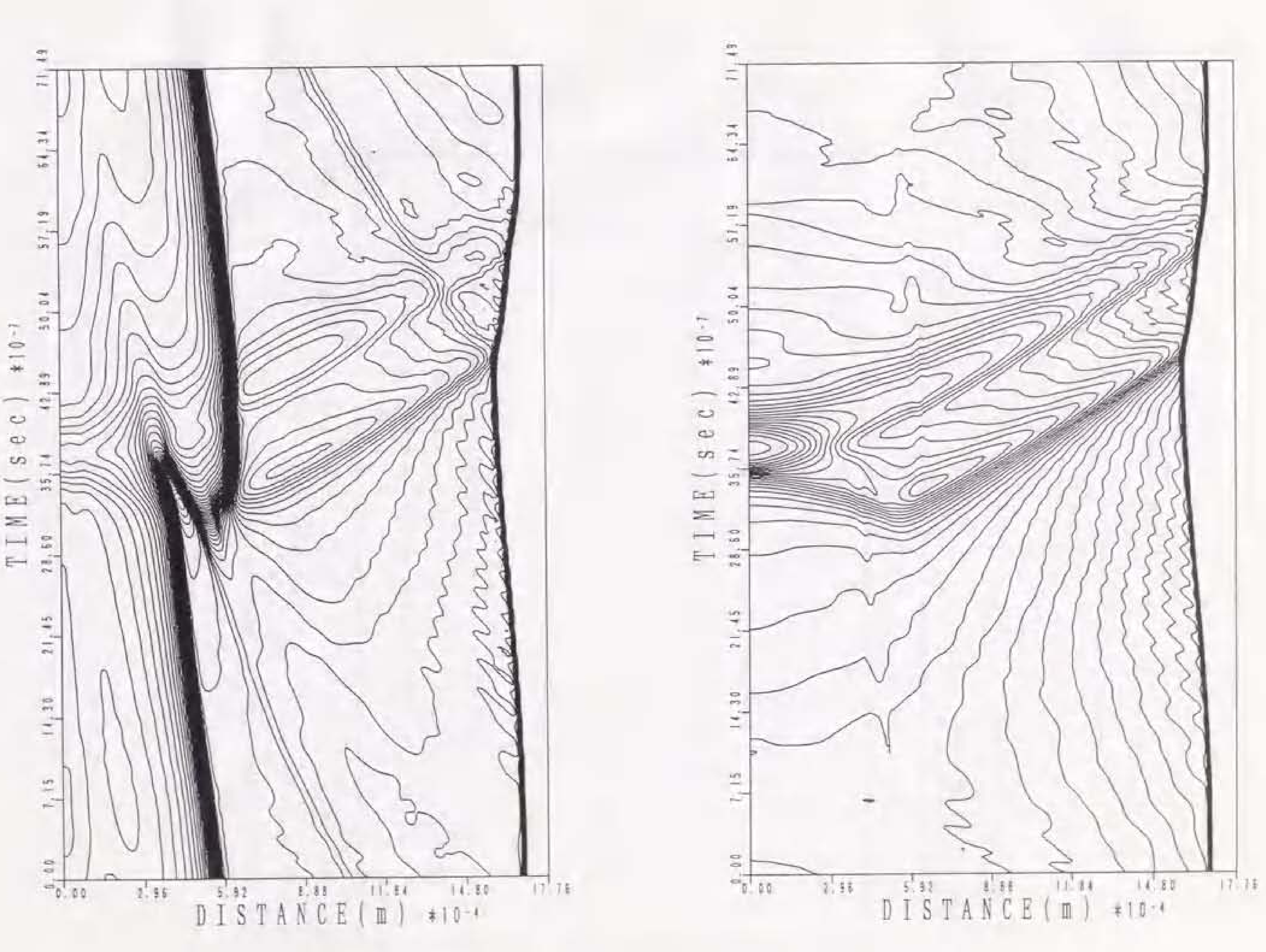

(a)

(b)

Figure 7.8 History (x-t diagram) of flow fields between the stagnation point and the bow shock wave on the stagnation streamline for the projectile velocity 1,685 m/sec: (a) density, (b) pressure

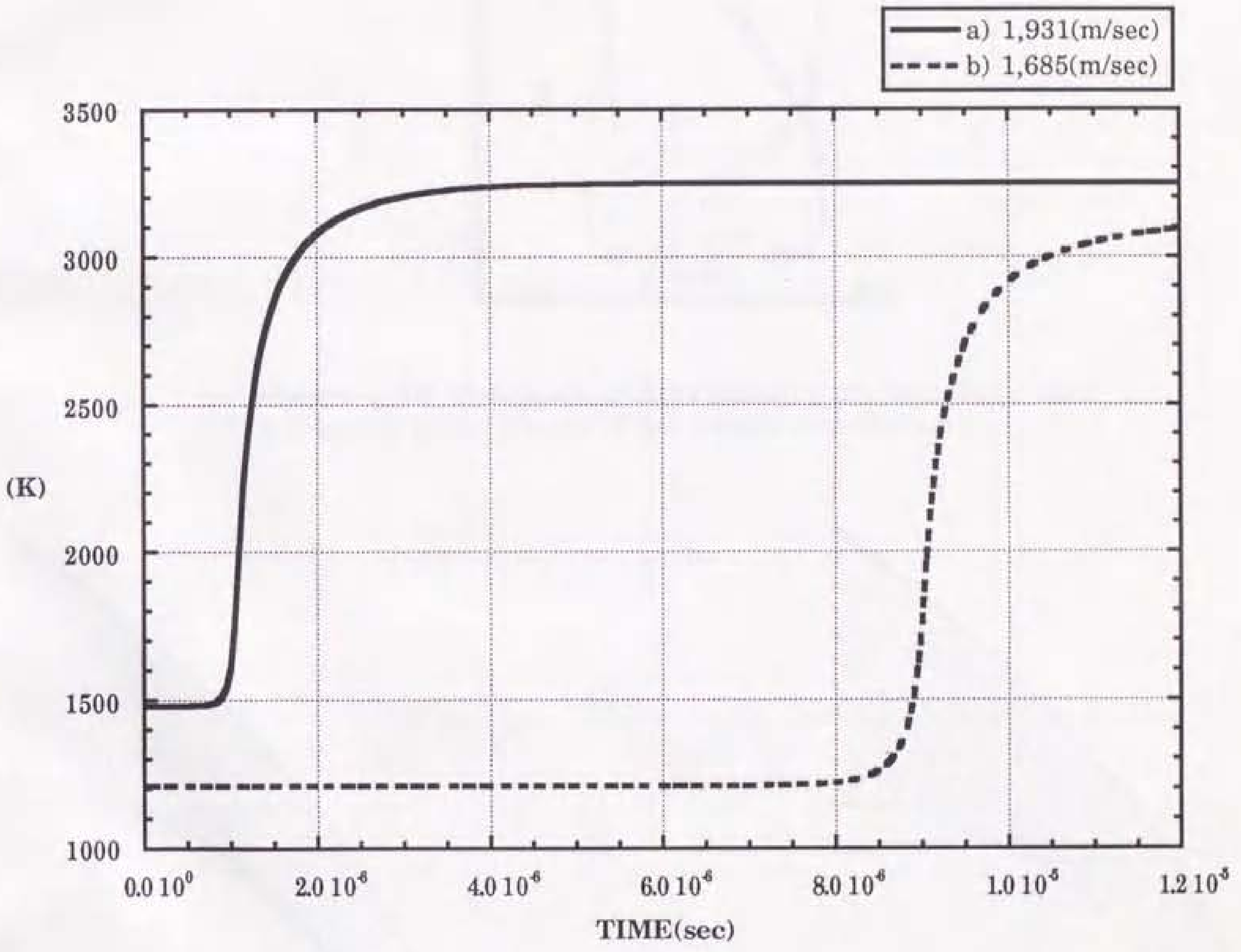

Figure 7. 9 Time-evolving temperature profiles: a) 1,931 m/sec; b) 1,685 m/sec

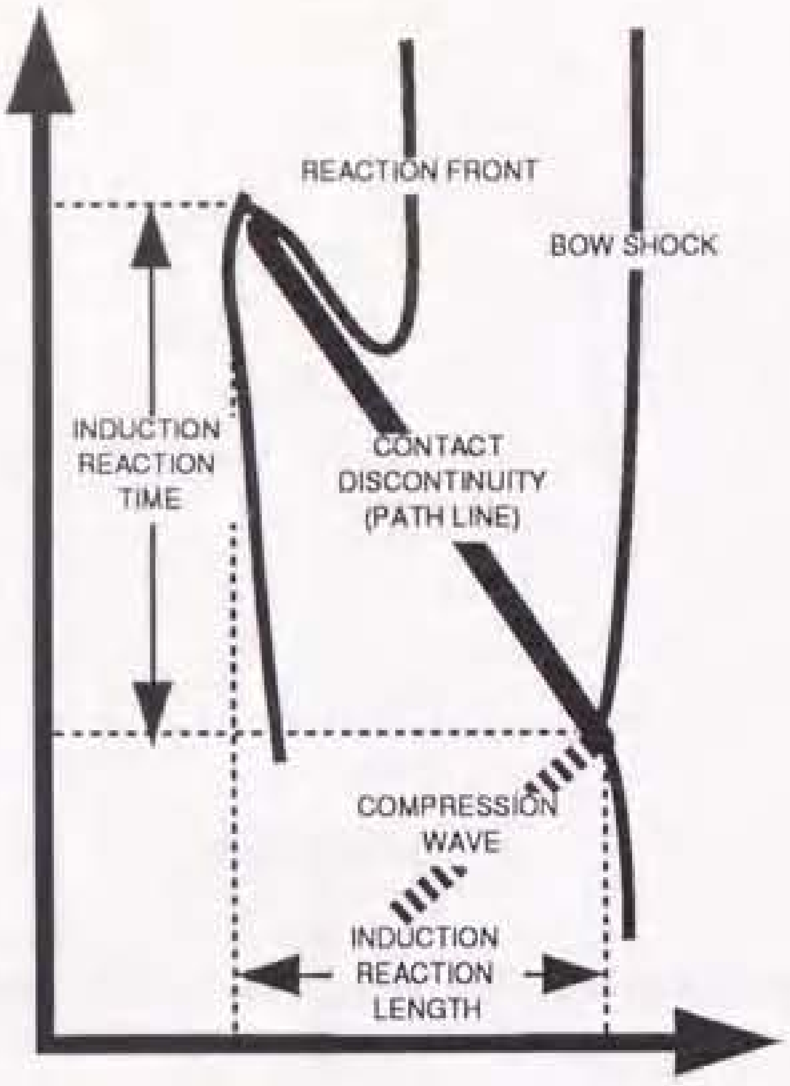

Figure 7. 10 Schematic picture showing the inductione time and length in the history of the density distribution

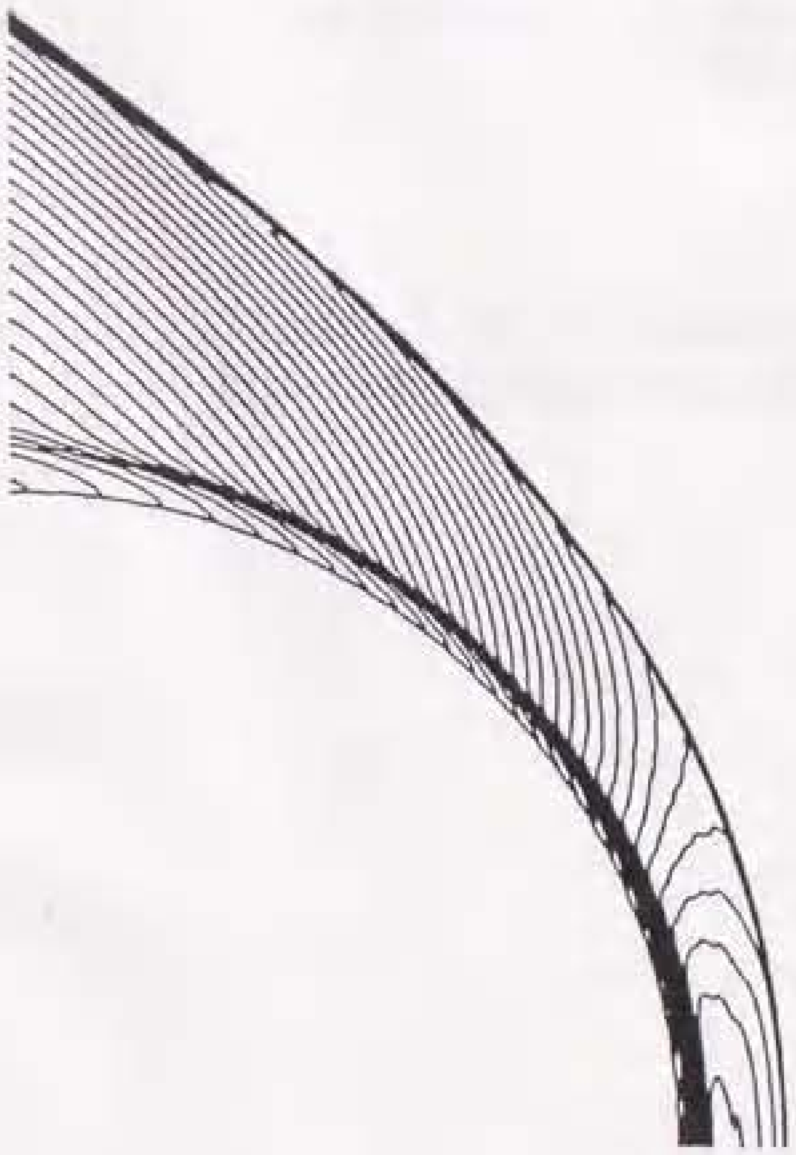

Figure 7. 11 Density contour plots for the projectile diameter 2.5 mm and the velocity 1,931 m/sec.

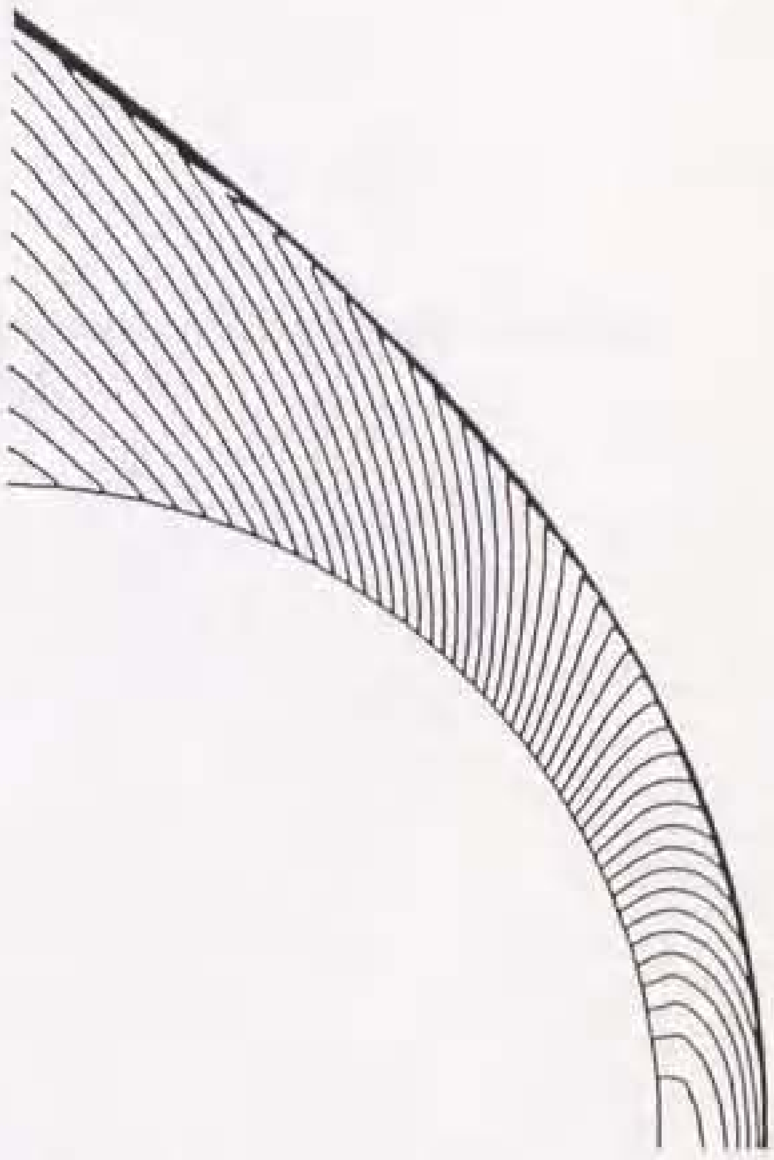

Figure 7. 12 Pressure contour plots for the projectile diameter 2.5 mm and the velocity 1,931 m/sec.

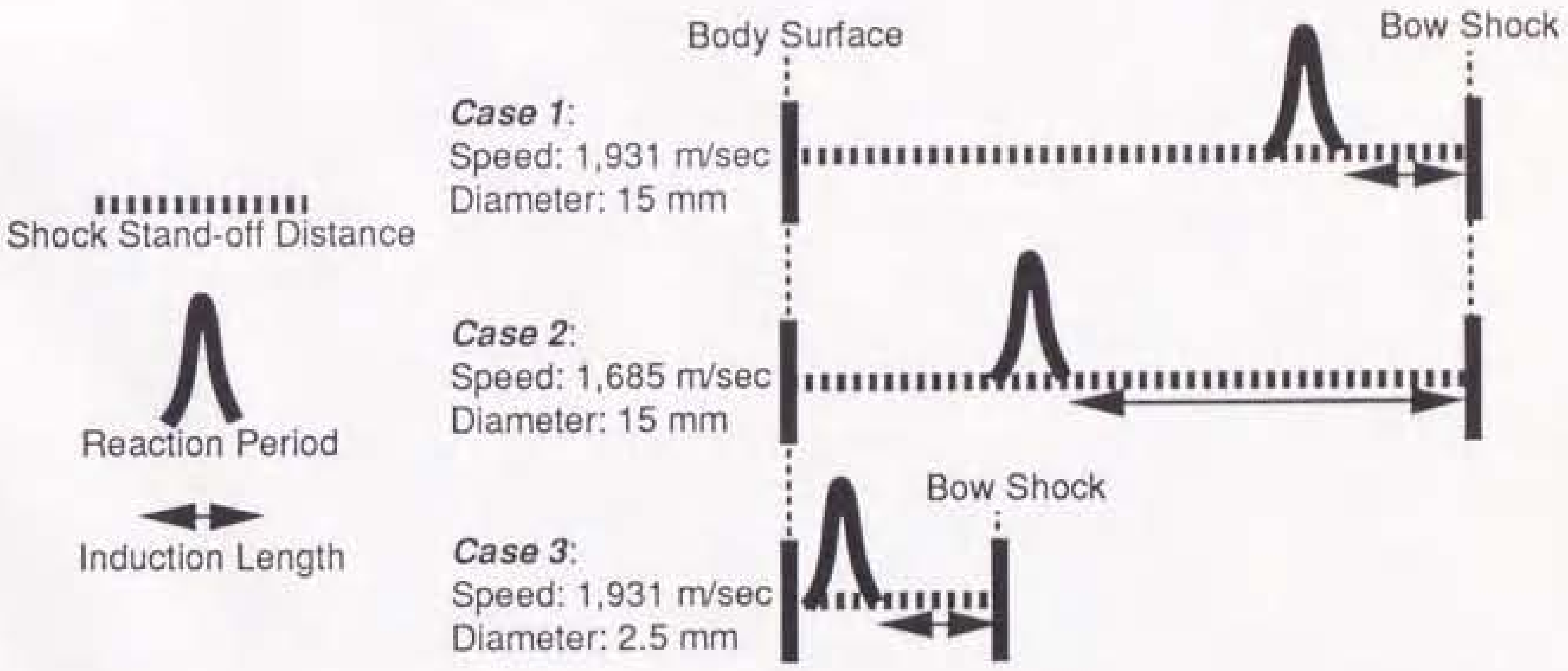

Figure 7. 13 Schematic picture showing the relative scale of the shock stand-off distance, the induction length and the reaction period


inches
cm
Kodak Color Control Patches
© Kodak, 2007 TM: Kodak
Blue
Cyan
Green
Yellow
Red
Magenta
White
3/Color
Black
Kodak Gray Scale
C
Y
M
© Kodak, 2007 TM: Kodak
A 1 2 3 4 5 6 M 8 9 10 11 12 13 14 15 B 17 18 19